UNIVERSITÀ DEGLI STUDI DI TRENTO

Doctoral School in Civil, Environmental and Mechanical Engineering

Topic 3. Modelling and Simulation

Marica Broseghini

Modelling of high-energy grinding processes

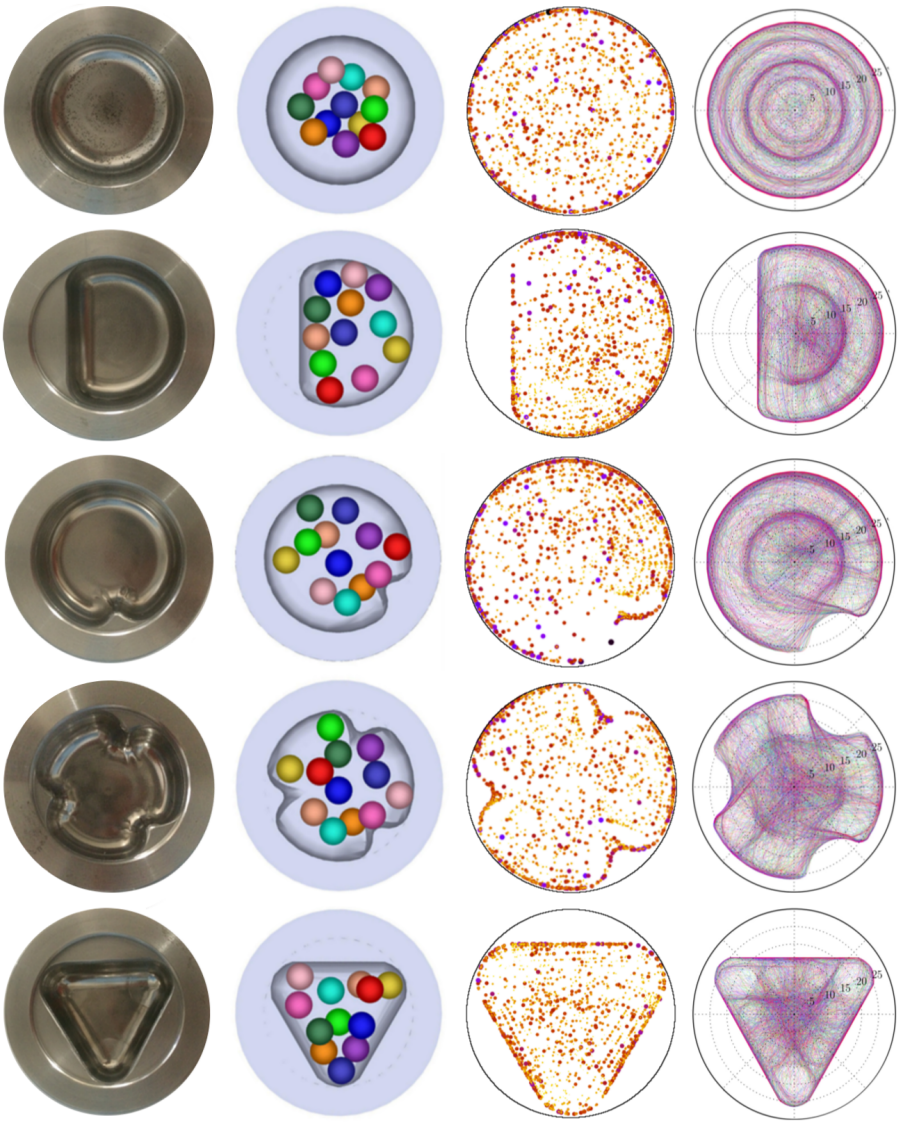

2017 - Doctoral thesis

UNIVERSITY OF TRENTO - Italy
Department of Civil, Environmental
and Mechanical Engineering

Doctoral School in Civil, Environmental and Mechanical Engineering
Topic 3. Modelling and Simulation - XXIX cycle 2014/2017

Doctoral Thesis - December 2017

Marica Broseghini

Modelling of high-energy grinding processes

Supervisors

Prof. P. Scardi - University of Trento
Prof. N.M. Pugno - University of Trento, Queen Mary University of London, Italian Space Agency

Credits of the cover image
M. Broseghini
Grinding Jars

ISBN (paper): ..... ; ISBN (online): .....

University of Trento
Doctoral School in Civil, Environmental and Mechanical Engineering
http://web.unitn.it/en/dricam
Via Mesiano 77, I-38123 Trento
Tel. +39 0461 282670 / 2611 - *dicamphd@unitn.it*

to my family

Contents

List of Equations

List of Tables

List of Figures

Chapter 1

Introduction

Grinding is a top-down process which exploits mechanical energy to diminish the size of solid materials and, in general, to introduce various defects modifying properties and internal energy of the product [1–3]. Early applications of this technique date back to the beginning of civilisation [2], growing in time to date, with a large variety of uses ranging from the production of boulders and pebbles from rock masses, limestone and clinker to make cement to the *top-down* preparation of nanostructured materials [2–5].

Among the multitude of grinding devices, this Thesis focuses on the *planetary ball mill*, an apparatus featuring high efficiency and versatility, being suitable for processing almost any kind of material [6, 7]. Examples of application chiefly include the mechanical alloying of metals as well as the synthesis of ceramics [8–10]. This technology proved also to be effective in processing organic and *exotic* materials, like, respectively, in the comminution of drugs, often required by pharmaceutical industry to enhance dissolution of poorly soluble compounds [11–14], and in the mechanical exfoliation of bulk systems, leading to large-scale production of two-dimensional nanostructured materials, such as graphene and boron nitride nanosheets [15, 16]. Moreover, besides reducing the size of the mill charge, this device is widely adopted to augment the internal energy of the ground solid materials, so to induce chemical reactions, an approach known as mechanochemistry [1, 17].

Although the design and the working principles of this device are rather simple and well known, being based on impacts between milling media (balls and jar) and mill charge, the characteristics of the end product strongly depend on a multitude of milling variables determining balls trajectories and velocities; these, in turn, depend on the nature and magnitude of the much less known impulsive forces acting during collisions [12].
Insights into the effect of some variables are provided by the wide literature available on this subject, but in general each application requires specific attention and calibration [12, 18]. A *brute-force* empirical testing, based on extended trial-and-error experimental campaigns, is the most frequently adopted approach to process parameters optimisation *i.e.* to select the best milling conditions for a given choice of mill and materials [12, 19–21].

As a valuable alternative, numerical simulations can be employed to investigate and comprehend mechanical processes. Indeed, the time evolution of kinematic and dynamic properties of milling media – as well as quantities involved in contact events – computed by these methods can shed light on the role of each milling variable and thus address the design of the characteristics of the end product [12, 18, 22]. The continuous development of methods and softwares combined with the constantly increasing power of computers contributed to augment popularity of this approach. In particular, multibody simulation is a powerful tool for the investigation and design of systems consisting of several bodies (multibody systems) and it is nowadays employed in several applications dealing with moving components, including

e.g. automotive industry, aerospace, robotics, machinery and biomechanics [23]. As a major advantage over other modelling approaches, multibody dynamics simulations produce a clear picture of the dynamic response of a system under different conditions, therefore allowing a quick and reliable optimisation of its performance [23, 24].

This Thesis chiefly deals with the development of a multibody dynamics model of the planetary ball milling process, including its validation and evaluation of the effect of the main milling variables; results also supported an investigation on innovative solutions to fine-tuning specific collisions features, involving the design of new jars with innovative internal shape.

Being the *collision* the crucial phenomenon underlying the milling process, in Chapter 2 selected contact models are discussed and the multibody dynamics framework employed to implement the model of the planetary ball mill is introduced.
The model is presented in Chapter 3, including a review of available analytical and numerical modelling methods, and it is exploited to analyse the effect of selected variables – *e.g.* the jar-to-plate velocity ratio. Special emphasis is given to the validation of the modelling outcomes against experimental data, indirectly accomplished by characterising the microstructure of a test material, calcium fluoride, by X-ray powder diffraction.
Chapter 4 focuses on the re-design of the internal shape of the jar that. This specific aspect of grinding technology, although barely investigated in literature, is revealed as an alternative and advantageous approach to improve the process efficiency. Particularly, new profiles modifying the ratio of normal-to-tangential transferred mechanical action are proposed with the main goal of enhancing the comminution efficiency of the mill charge and reducing process time. Modification of balls motion regimes increasing the number of high-energy impacts is analysed in simulations and validated by *in-operando* video recordings of the process. Experimental grinding of calcium fluoride powder is performed to assess the effect of milling time, through the evaluation of the size and strain of the end product.
To conclude, two rather extreme and opposite case studies are considered in Chapter 5, proposing the investigation of the milling process of two materials requiring energy to be exchanged mostly along either the tangential or the normal direction to be successfully accomplished, corresponding respectively to the exfoliation of graphite and the comminution of the anti-HIV drug Efavirenz.

1.1 Problem statement and goals

The fundamental purpose of this Thesis is to investigate the ball milling technique, whose success strictly relates to the careful milling parameters assessment, governing the effectiveness of the large amount of involved impacts. For process optimisation, namely for the set up of the milling variables leading to the best grinding results, the use of the multibody dynamics simulation technique is proposed as an alternative to experimental testing. This enables understanding of the role of each grinding variable – *e.g.* physical properties of colliding bodies and kinematic parameters – on the characteristics of the end product, both in terms of comminution efficiency and defects content. In contrast to experimental testing, computer simulations allow for a quicker, cheaper and more insightful comprehension of the effect of different parameters, as well as the implementation of innovative grinding solutions. Moreover, selected case studies are corroborated by an experimental X-ray powder diffraction structural and microstructural characterisation of the end product, to deeply correlate modelling outcomes and ground material characteristics.

Concisely, the basic objectives of the Thesis follow:

1. to understand the fundamental laws of impact dynamics and their implementation into a multibody dynamics simulations framework (Chapter 2)
2. to develop a procedure to estimate contact parameters needed by contact laws (Chapter 2)
3. to develop a numerical multibody dynamics model of the planetary ball mill and to validate it either directly, against camera recordings, and indirectly, against X-ray powder diffraction characterisation of the end product (Chapter 3, Chapter 4)
4. to propose and test innovative solutions, *e.g.* the modification of the internal shape of the jar to increase grinding efficiency (Chapter 4)
5. to employ the model to design solutions enhancing the force exchange along a specific contact axis as required for processing peculiar materials *e.g.* graphene and the anti-HIV drug Efavirenz, assumed as relevant case studies (Chapter 5)

Chapter 2

Some remarks on contact dynamics modelling

Impact is defined as the process occurring every time two or more bodies collide [25–27]. The scientific and technological disciplines in which this notion can be found range from astrophysics and space exploration – *e.g.* the Moon Impact Probe, used to discover the presence of water on the Moon [28] – to microscopic particle technology, from particle physics to the investigation of matter – *e.g.* by means of X-ray, neutron or electron scattering – from ballistics to mechanical engineering and robotics [26, 27, 29–34]. An impact event is mainly characterised by very short duration, sudden change in colliding bodies velocities, very large stresses, deformation localised in the contact area and, usually, consequent dissipation of energy in various forms including *e.g.* permanent deformation, friction and heat [25, 35]. The phenomenon is therefore complex, depending on several properties of impinging bodies *e.g.* material characteristics, bodies geometry and relative velocity: theoretical models providing with a simplified description of the physical process are thus necessary to investigate the behaviour of colliding bodies [25, 26].
Research on impact dynamics modelling started with Newton's work [36], who analysed collisions among rigid bodies and formulated motion laws and correction factors accounting for energy loss [26, 36]. Further important advances were later granted by the advent of the theory of elasticity and, within this field, the Hertz's formulation describing the deformation and stress distribution near the contact point must especially be cited [37]. Successive extensions of these methods as well as new approaches to the problem – *e.g.* including vibrational aspects – have been proposed (see *e.g.* [38–41]), leading to the modern formulations capable of investigating complex contact scenarios [34]. As a further step forward, in more recent years research focused on the development of algorithms implementing contact models into computer codes, allowing to simulate the dynamics of complicated systems involving a large amount of objects (multibody systems) and impact events [34].
The fundamental goal of this Thesis is the development of a multibody dynamics computer model for the investigation of the behaviour of the planetary ball mill, a mechanical grinding apparatus exploiting impacts to accomplish its task. Crucial point in achieving reliable simulation results is the comprehension of the fundamentals of impacts modelling [34] and, therefore, the most widespread theories are briefly reviewed in the next section. An insight on the main concepts of multibody dynamics simulation technique is then also provided, focusing especially on the solutions adopted to deal with impacts.

2.1 Contact dynamics modelling

Among the several theories proposed in literature to describe the behaviour of colliding bodies, two main approaches can be distinguished, namely the discrete and continuous methods[‡]. Particularly, while the former assumes that the impact event is instantaneous and does not significantly alter the configuration of colliding bodies, the latter presupposes a finite duration of the event and a contact force acting

[‡]While other schemes and/or methodologies can be found in literature, this Thesis chiefly follows the approach proposed in [25]

continuously, in turn resulting in deformation and stresses at the contact area [25]. Below, peculiarities of the most widespread contact models belonging to both categories are briefly reviewed.

2.1.1 Discrete contact models

The discrete approach (or impulse-momentum method or nonsmooth dynamics formulation [42]) refers to the oldest and classical theory of impact, called steromechanics, mostly based on the impulse-momentum law. It was introduced by Isaac Newton [36], analysing the impact among rigid bodies, and later expanded mainly by Whittaker [43] to include also the effect of friction. This approach is based on the fundamental assumptions that (i) colliding bodies are rigid, (ii) the interaction among them is instantaneous, (iii) the arising impact force has impulsive nature, (iv) the velocities undergo a sudden an discontinuous change whereas (v) the configuration of the bodies does not change significantly at contact location [25, 26]. The impact dynamics is modelled through the linear impulse-momentum and the angular impulse-momentum principles, introducing relations among the problem variables relative to the beginning and to the end of the event [25, 26, 31]. Particularly, for the most straightforward case of the non-frictional central [†] impact of 2 non-rotating bodies (examples treating more complex conditions *e.g.* presence of friction can be found in [26]) these laws lead the event to be described as[26],

$$\begin{cases} m_1\, v_{1,\,i_n} + m_2\, v_{2,\,i_n} = m_1\, v_{1,\,f_n} + m_2\, v_{2,\,f_n} \\ v_{1,\,i_t} = v_{1,\,f_t} \\ v_{2,\,i_t} = v_{2,\,f_t} \end{cases} \tag{2.1}$$

where v are the velocities and m the masses of the approaching bodies, whereas n, t denote the normal and the tangential directions of a coordinate system with origin at the contact point, 1, 2 the bodies and i, f the beginning and the end of the impact respectively. While for this simple configuration the tangential component of the velocity remains unchanged, to predict the velocities of objects after the event in normal direction, v_{1,f_n} and v_{2,f_n}, an additional relation is required and it can be provided by the so-called coefficient of restitution, e [26, 31]. This parameter represents the energy loss during the impact and ranges from 0 and 1 idealising the concepts of plastic and perfectly elastic collision, respectively. Several formulations have been proposed for e and, according to the most common, it can be expressed as the ratio of final-to-initial relative normal velocity components ($\dot{u_f}/\dot{u_i}$) [26]

$$e = \frac{v_{2,\,f_n} - v_{1,\,f_n}}{v_{2,\,i_n} - v_{1,\,i_n}} = \frac{\dot{u_f}}{\dot{u_i}} \tag{2.2}$$

Therefore, from equations 2.1 and 2.2, v_{1,f_n} and v_{2,f_n} can be computed as a function of e,

$$v_{1,\,f_n} = v_{1,\,i_n} - (1+e)\,\frac{m_2\, v_{1,\,i_n} - m_2\, v_{2,\,i_n}}{m_1 + m_2} \tag{2.3}$$

$$v_{2,\,f_n} = v_{2,\,i_n} + (1+e)\,\frac{m_1\, v_{1,\,i_n} - m_1\, v_{2,\,i_n}}{m_1 + m_2} \tag{2.4}$$

being e estimable from *e.g.* experiments [26, 44].
For more complex cases, where frictional properties of contact surface are taken into account, other equations must be introduced for completely describe the impact process. In particular, friction affects the tangential component of the velocity of colliding bodies that, remains constant in an impact among

[†]Central impact occurs when the contact point of impinging bodies is located on line connecting their centres of mass [26]

two perfectly smooth surfaces (no friction) whereas vanishes if impinging objects are completely rough (infinite friction) [26]. The most exploited law to account for this phenomenon is the so-called Coulomb's model (see figure 2.2), depending on the friction coefficient μ, which is also the only one that can be adopted within the discrete approach for contact modelling.
The main advantages of this approach are the straightforward mathematical description and the availability of closed-form analytical solutions for simple impact geometries. However, this model can give predictions only on the velocities after the impact and the consequent energy loss, which also strongly relates to the coefficients of restitution and friction that should therefore be carefully determined. Moreover, this model is incapable of describing contact force, stress and deformation at contact location and, as an another drawback, it is not easily extendible to more complex impact scenarios, where impacts occur at the same time in many points of the system [25, 45].

Coefficient of restitution: theory and experimental assessment

The coefficient of restitution e purports to globally describe the energy dissipated in an impact, incorporating many dissipative phenomena *e.g.* viscoelasticity of materials and plastic deformation at contact surfaces as well as vibrations in the bodies [26]. It is a dimensionless quantity, varying between 0 and 1, where these 2 limit cases represent respectively the perfectly inelastic and the perfectly elastic impact *i.e.* in the former case all the energy is dissipated and at the end of the event the 2 colliding bodies move as a single mass whereas in the latter, the kinetic energy of the system is completely conserved.
The first definition of e was derived by Newton [36] from the law of conservation of mechanical energy and expresses it as the ratio of final-to-initial relative velocity of impinging bodies (equation 2.2). Although more refined expressions have been proposed in literature [25, 27, 46], the Newton's one is still the most used owing to its mathematical simplicity.
Originally, the value of e was believed to be an intrinsic property of materials but experiments, mainly performed by Goldsmith, pointed out its dependence on mass, shape as well as relative velocity of colliding bodies [26].
Referring to Newton's definition, the most straightforward way to determine e from experiments is dropping a sphere on a flat plate from a height h_0 and measuring the first rebound height h^*. Indeed, being the relative velocity of the 2 bodies equal to the velocity of the sphere and exploiting the kinematical equation of free fall, $v = \sqrt{2gh}$ (where g is the gravitational acceleration), e can be computed as

$$e = \frac{\dot{u}_f}{\dot{u}_i} = \sqrt{\frac{2gh^*}{2gh_0}} = \sqrt{\frac{h^*}{h_0}}. \tag{2.5}$$

Being this parameter crucial for properly predicting the impact dynamics, some experimental tests were performed following this approach, so to determine the most appropriate e for materials and geometries that will be adopted later in this Thesis for the modelling of the collisions involved in the planetary ball milling process. Experimental procedure and results of the performed tests are reported hereafter.

Experimental tests Sphere-on-plate drop tests were performed for (i) a 12mm diameter steel sphere and a 10mm thick massive steel flat plate and for (ii) a 6mm diameter zirconium-oxide (yttria stabilised) sphere and 10mm thick zirconium-oxide (yttria stabilised) flat plate. The sphere was dropped from a height h_0 increased from 100 to 800mm by steps of 100mm so to investigate the effect of different initial relative velocities $\dot{u}_i$. For every height 10 tests were performed.
The employed testing apparatus is shown in figure 2.1 and comprises of a dropping column allowing to release the ball by switching off a magnetic field, a steel flat base holding the target and a high-speed camera (Sony Action Cam HDR-AS200V, 240 fps, 1280X720 pixel resolution) recording the tests.

Collected movies allowed to read the first rebound height, h^*, on a millimetric scale located behind the dropping column.

Figure 2.1: Drop test experimental setup

Error in measuring h^* mostly relates to the reading of the millimetric scale and to parallax and, since it can be considered the same for each test, it is not reported in the results. A rough estimate of its value could be ± 5mm. As an example, table 2.1 shows the results of the tests performed for the (ii) case of a zirconium oxide ball dropped on a zirconium oxide plate. For every h_0, the average h^* resulting from the 10 performed test is reported.

h_0	h^*	e
100	76	0.87
200	155	0.88
300	215	0.86
400	322	0.9
500	404	0.9
600	483	0.9
700	582	0.92
800	646	0.9
		$e_{average}$=0.9

Table 2.1: Results of drop tests performed for a zirconium oxide sphere dropped from different heights h_0 on a zirconium oxide plate providing with an average estimate of the coefficient of restitution, $e_{average}$

The same tests were repeated for the (i) steel on steel case and provided with $e_{average}$=0.516

Friction models

Friction at the contact location is another crucial aspect of the impact process, influencing the motion of the bodies as well as the energy dissipation [25, 47].
The first and most straightforward friction model refers to the Coulomb law, stating that (i) the direction of the frictional force, F_t, is always opposite to the relative tangential motion between colliding bodies and (ii) its magnitude can be related to the magnitude of the normal contact force, F, through the so-called friction coefficient, μ [25, 47, 48]. Particularly, friction at the contact point was shown to prevent colliding bodies from sliding (sticking condition, characterised by null relative tangential velocity of bodies $\dot{u}_t$) as long as [25, 47, 49]

$$F_t \leq \mu_s \, F, \tag{2.6}$$

where μ_s is the static friction coefficient. Once sliding occurs, F_t can be described instead by the equation

$$F_t = \mu_d \, F \, \frac{\dot{u}_t}{|\dot{u}_t|}, \tag{2.7}$$

being μ_d the dynamic friction coefficient and $\dot{u}_t$ the relative tangential velocity of the colliding bodies.
It is worth noting that two friction coefficients are used, μ_s and μ_d, since experiments demonstrated that an higher external tangential force is required to start the motion than to maintain a constant relative velocity. Coefficients μ_s and μ_d were shown to depend only on the characteristics of the surfaces in contact – mainly material and surface quality – and not on the relative velocity (see figure 2.2) [47, 48]. Although literature suggests straightforward tests to estimate these coefficients, for the sake of simplicity they are often assumed to be equal and only a single value, μ, is used [25, 47, 48].
The Coulomb friction model, whose most straightforward formulation is depicted in figure 2.2a, introduces a discrete transition from sticking to sliding and *viceversa* characterised by a discontinuity for $\dot{u}_t$ crossing zero, that can lead to numerical instability as pointed out by some authors [25, 47, 48]. Nevertheless, this is the only model compatible with the discrete description of the impact and, moreover, being easily implementable, it has often been exploited. Extensions of this formulation were also developed to capture more complex phenomena like viscous friction (see *e.g.* [48]).

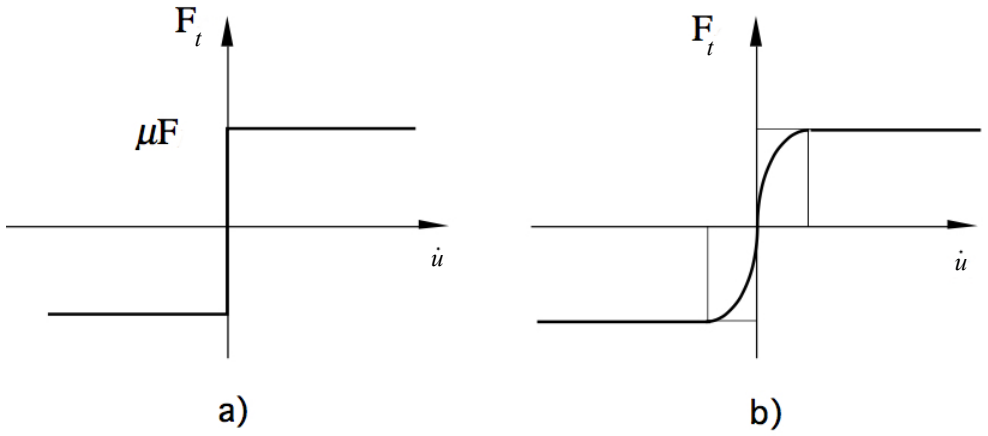

Figure 2.2: The Coulomb friction model in the (a) standard and (b) regularised formulations. The latter formulation smooths the intrinsic discontinuity of the former to avoid discontinuities in computation. More detail are reported in subsection 2.1.2. *Adapted from [23].*

Dynamic friction coefficient experimental assessment A widespread experimental method to evaluate the dynamic friction coefficient, μ_d, is the pin-on-disc tribological test [50] and it is exploited in this Thesis to characterise the frictional behaviour of the couples of materials involved in the modelling of the planetary ball mill, presented in the next chapter. It is worth noting that materials constituting the milling media as well as the mill charge have been tested since during the grinding process impacts among milling media either free or covered by a layer of ground material can occur.
Experiments were performed using a pin-on-disk tribometer (CSM tribometer [51], see figure 2.3) consisting of a fixed pin under an applied load in contact with a rotating stage holding the sample (generally a disk). Every shape can be adopted for the pin so to account for the effect of geometry at contact area [50] but the most exploited is the spherical one, which is also the most suitable to represent interactions among spheres and/or jar wall, typical of the ball mill. Therefore, for the experiments here proposed, a 6mm diameter pin was used together with a 50mm diameter and 5mm height disk.

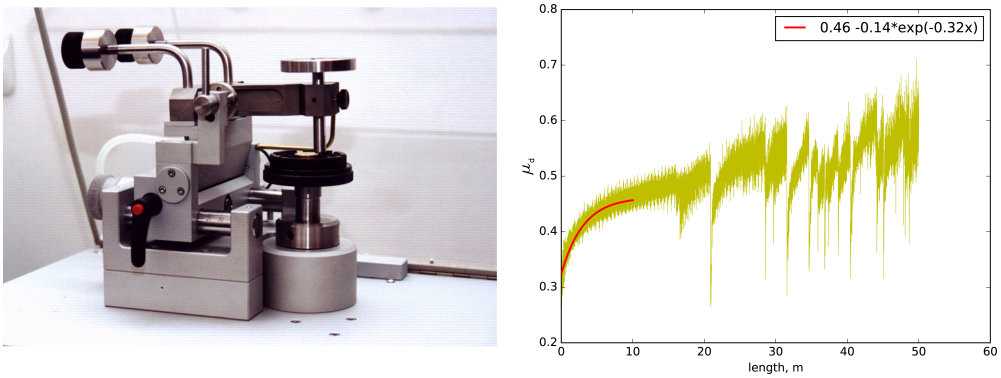

Figure 2.3: Left, pin-on-disc tribometer [51], right, an example of coefficient of dynamic friction measured during the tribological test and exponential fit of the data. The example is relative to one of the tests performed for a zirconium oxide pin and a Efavirenz disk (Efavirenz is a pharmaceutical, treated in detail in chapter 5)

During the experiment the friction force is measured continuously and, exploiting the Coulomb law, the coefficient of friction is computed as the ratio of this force to the loading force on the pin. At the end of the experiment the average coefficient of friction is provided. However, as shown in figure 2.3right, the obtained value was further validated by fitting an exponential curve to the data corresponding to the first part of the test, where the measure is presumably not affected by wear and other phenomena arising during the test, changing the geometry of the pin. Different couples of materials were tested adopting 2N load, 1.2 m/s rotation speed and 1200 sliding distance. 8 experiments were performed for each case and the mean value of the resulting μ_d is reported in table 2.2.

Material Pin	Material Disk	μ_d
Steel (AISI C1020)	Steel (AISI C1020)	0.8
Steel (AISI C1020)	Calcium Fluoride	0.2
Zirconium Oxide	Zirconium Oxide	0.67
Zirconium Oxide	Efavirenz	0.2

Table 2.2: Results of tribological tests providing with the dynamic friction coefficient for different couples of materials tested since they are going to be involved in the simulations of the ball milling process, as reported in the next chapters.

2.1.2 Continuous contact models

The previously-described discrete method refers to the hypothesis of rigid bodies. However, physical objects are compliant and therefore the impact duration – although extremely short – is greater than zero [45]. According to this more realistic view of the phenomenon, continuous (or force-based) models, describing the impact dynamics as a continuous-time event, have been developed. This formulation (i) assumes that colliding bodies deform and undergo local indentation and (ii) introduces a contact force, expressed as a function of indentation, acting in a continuous manner over the finite impact duration. This implies a simple addition of the contact forces to the equations of motion upon the occurrence of a collision, quite easily identifiable through *e.g.* a minimum distance criterion. A valuable advantage of the continuous over the discrete approach is that not only the relative velocities of bodies after the impact but also insights on the pressure at contact location can be assessed using this method [25, 45]. Furthermore, the method can be almost effortless extended to a multiple contacts scenario and it is well suited for the implementation into computer codes dealing with impact dynamics problems (*e.g.* multibody dynamics or the Discrete Element Method (DEM)) owing to its computational simplicity and efficiency [25, 34].
Also thanks to to the development of Computer Aided Engineering (CAE) analysis tools, over the last decades the continuous method gained increased importance and several expressions of the interaction force at the surface of two bodies in contact were postulated [29, 52].
Some of the proposed models are purely elastic while others include dissipative terms, generally expressed in the form of internal damping. Some widespread schemes are briefly reviewed below and some hints about parameters assessment are also given. A short description of friction models is also provided since, unlike the discrete approach, the continuous method permits to adopt several different formulations for taking into account the phenomenon.

Pure elastic contact force models

Linear Hooke contact model The simplest elastic contact force model, known as the Hooke's law, consists of a linear spring element embodying the elasticity of the contacting surfaces. The normal – *i.e.* along the impact axis – contact force, F, is expressed as

$$F = k_l\, u, \tag{2.8}$$

being k_l the spring stiffness and u the compenetration between the colliding bodies (namely, the relative displacement of two bodies from the beginning of the contact event, as illustrated in figure 2.4). The coefficient k_l depends on objects physical properties and geometry and can be analytically estimated for simple cases or through experiments [53, 54], whereas u is computed from the relative positions of the bodies during the collision.
Only a rough description of the contact force is provided by this model, unable to properly account for the complexity of shape, surface conditions and mechanical properties of colliding objects [34].

Non-linear Hertz contact model One of the most exploited representations of the impact force refers to the Hertz theory of contact [37]. This pioneering work, described in detail *e.g.* in [26], provides a geometrical relation among compenetration (assumed to be localised in a very small contact area) and the static compression of two isotropic elastic bodies with smooth surfaces that, within the contact area, can be approximated by two paraboloids [37].
The expression derived for the contact force is a non-linear power function of compenetration, that can

be idealised as a non-linear spring acting along the impact axis,

$$F = k\,u^n, \tag{2.9}$$

where k and n are, respectively, the generalised stiffness parameter and the non-linear power exponent, depending on material and geometric properties at the contact area and estimable through elastostatic theory [37].
The parameter n, in case of a parabolic distribution of stresses, equals 3/2 as in the original work by Hertz [34] but it can be varied if materials at the contact surface exhibit peculiar characteristics [55, 56].
The value of k for two colliding spheres i and j is expressed as

$$k_{sph-sph} = \frac{4}{3\pi}\left(\frac{1}{\eta_i + \eta_j}\right)\sqrt{\frac{R_i R_j}{R_i + R_j}}, \tag{2.10}$$

and for a collision between a sphere i and a plate j,

$$k_{sph-plate} = \frac{4}{3\pi}\left(\frac{1}{\eta_i + \eta_j}\right)\sqrt{R_i}, \tag{2.11}$$

where R is the sphere radius and η includes the elastic properties of the materials,

$$\eta_i = \frac{1-\nu_i^2}{\pi E_i}, \tag{2.12}$$

being ν the Poisson's ratio and E the Young's modulus.
The advantages of the Hertz law over the Hooke scheme rely on the improved physical meaning, represented both by the non-linearity and on the connection between model parameters and body properties. However, this formulation does not account for energy dissipation and therefore it is limited to low impact speeds, hard materials and frictionless surfaces [25].

Dissipative contact force models

Since the amount of energy dissipated in a contact event is generally not negligible, the previously introduced purely elastic schemes are not the most appropriate for the careful description of the impact phenomenon and, therefore, several models augmenting the Hookean or the Hertzian laws with dissipative terms have been proposed [25, 34, 45]. The dissipative contact force models are typically representable by a spring-dashpot scheme [26], tuned by a parameter expressing the internal damping of materials. Many linear and non-linear formulations of this term have been developed, generally in turn a function of the coefficient of restitution, e [25, 27, 57].

The linear Kelvin-Voigt contact model (linear spring and linear damper) The simplest dissipative contact force model is the one named after Kelvin and Voigt [26], schematising the impact through a linear spring in parallel with a linear damper (dashpot) representing, respectively, the elastic behaviour and the dissipation of energy. In this framework, the normal component of the contact force is expressed as [27, 34]

$$F = k_l\,u + c\,\dot{u}, \tag{2.13}$$

being k_l the spring stiffness (Hooke's-type behaviour), u the compenetration (see the linear Hooke contact model), c the linear damping coefficient and $\dot{u}$ the relative normal velocity of colliding bodies.
The c parameter can be estimated from the solution of the classic problem of damped vibration of a mass spring system, where it is expressed as the product of the damping ratio, ζ, and the critical damping, c_c, of the system [58, 59], *i.e.* for two colliding bodies i and j [27]

$$c = \zeta\, c_c = \zeta\, 2\, m_e\, \omega_n = \zeta\, 2\sqrt{m_e\, k_l}, \tag{2.14}$$

being $\omega_n = \sqrt{\frac{k_l}{m_e}}$ the natural frequency of the system and $m_e = \frac{m_i m_j}{m_i + m_j}$ its equivalent mass. For ζ and k_l different formulations have been proposed, and in particular an explicit relation between ζ and the coefficient of restitution, e, was derived by Zang *et al.* [57, 60],

$$\zeta = -\ln(e)\sqrt{\frac{1}{\ln^2(e) + \pi^2}}, \tag{2.15}$$

leading to

$$c = -2\ln(e)\sqrt{\frac{1}{\ln^2(e) + \pi^2}}\sqrt{m_e k^*}. \tag{2.16}$$

A possible equivalent formulation for the stiffness, k^*, was provided by Di Maio *el al.* [61] by imposing the equality between the maximum force-to-displacement ratio computed from Hertz theory and from the linear model, resulting in

$$k^* = \left(\frac{320}{81} m_e \dot{u}_{n0}^2 E_e^4 R_e^2\right)^{1/5}, \tag{2.17}$$

where $\dot{u}_{n0}$ is the relative normal impact velocity and $1/R_e = 1/R_i + 1/R_j$ and $1/E_e = 1/E_i + 1/E_j$ account for the geometrical and elastic properties of the colliding bodies respectively .
Some weakness of the Kelvin-Voigt model have been highlighted in literature. Particularly, the formulation of the dissipative term leads to a non-zero contact force at the beginning of the impact event and to a negative force – *i.e.* attractive – at the end (being in this condition the compenetration null and the relative velocity negative), obviously not correct from a physical point of view. Furthermore the energy dissipation rate is improperly assumed to be constant during the entire contact event due to the fixed value of the damping coefficient [25, 62–64]. Nevertheless, the model was demonstrated to provide a satisfactory approximation of the phenomenon in case of reasonably small material damping and moderate relative impact velocity and therefore it has been often exploited, especially owing to its simplicity [61, 65–69]. In particular, this model was the first to be introduced in numerical methods (*e.g.* within the DEM [70]) and computer codes developed to investigate the dynamics of systems with multiple interacting bodies, such as granular materials [71].

The non-linear spring and linear damper model To partially account for the non-linear nature of the impact, Dubrowsky *et al.* presented an extension of the linear Kelvin-Voigt scheme, modelling the behaviour of colliding bodies at the contact area through a Hertzian spring and a linear damper [72],

$$F = k\, u^n + c\, \dot{u}, \tag{2.18}$$

where n and k are given by the Hertz law (k computed according to equations 2.10 and 2.11 for *e.g.* a sphere-sphere and a sphere-plate contact respectively) and equations 2.16 and 2.17 can give an estimate of the damping parameter, c. However, as for the Kelvin-Voigt case, the physics of the energy loss is not accurately represented by this model since the damping parameter is constant [73].

The non-linear spring and non-linear damper model To overcome the limits of the previous models, Hunt and Crossley proposed the following representation of the contact force, adding a non-linear viscous damper to the Hertzian response [73]

$$F = k\,u^n + C(u)\,\dot{u}, \tag{2.19}$$

being $C(u)$ the damping coefficient that, to satisfy the boundary conditions of null contact force at the beginning and at the end of the impact event, is expressed as a function of the compenetration, u, between colliding bodies, modelling as well a non-constant energy loss during the impact, therefore leading to a more physically sound representation of the event [25, 34] at the cost of augmented computational complexity (for more details see *e.g.* [34]).

Other dissipative contact models Starting from the non-linear spring and damper model, other schemes have been developed especially to account for plastic or permanent deformation at the contact area [44, 74, 75]. More details can be found *e.g.* in [25, 34].

Friction models

As an advantage over the discrete method, several models for friction can be adopted within the continuous approach to impact modelling [25]. The simplest and most exploited ones consist of regularised expressions of the Coulomb friction model (see figure 2.2b), smoothing the intrinsic discontinuity of the standard formulation and thus allowing a continuous transition from sticking to sliding through a continuous friction force [48].
More complicate formulations have also been developed to properly include various friction phenomena – *e.g.* stick-slip, viscous friction or pre-sliding – that can influence the dynamic response of the system (an exhaustive list is reported *e.g.* in [48]). However, price to pay for a more accurate description of the phenomenon is the dependence of the model on a larger number of parameters that often can not be easily estimated [25, 48].

Parameters assessment

The main drawback of the continuous impact models with respect to the discrete ones is the greater effort required for parameters assessment, especially for the generalised stiffness and the damping coefficients [25, 48]. As shown, these parameters are expressed as mathematical functions of physical and geometrical properties of colliding bodies and they are not directly measurable from simple experiments, as a difference with the discrete approach where models mainly refer to the coefficient of restitution deducible from *e.g.* drop tests. Although accurate, analytical formulas provide an estimate of the coefficients that should be validated and, eventually, tuned *e.g.* by comparing the modelling outcomes and the results of experimental tests [25].

2.2 Impacts in multibody dynamics simulations

Since 1988, when it first appeared in a textbook [32], the kinematic and dynamic computer simulation has become a powerful tool for the investigation and the design of systems consisting of several bodies (multibody systems) and it is nowadays employed in almost any application dealing with moving components, including *e.g.* automotive industry, aerospace, robotics, machinery and biomechanics [23]. Multibody dynamics simulation provides with a clear picture of the dynamic response of a system under different conditions, therefore allowing to quickly and economically optimise the performance [23, 24].
The importance gained by this simulation technique is demonstrated by the number of available softwares and, above all, by the publication of a large amount of studies [24], investigating and addressing several issues including, but not limited to, methods for the formulation and the more efficient numerical solution of the equations of motion [76, 77] as well as analyses on the modelling of material properties and mechanical constraints [78].
This method usually incorporates a finite set of mathematically described elements including rigid or elastic bodies, kinematic constraints (joints), springs and dampers, bearings, gears as well as forces and torques for the definition of the characteristics and the dynamics of the system. The temporal evolution is obtained by numerically integrating the equations of motion, generally expressed according to the Newton-Euler or Lagrange formalism, together with additional constraints and contact conditions [23, 45].
Being moving bodies often subjected to impacts, the implementation of contact and friction models ever more sophisticated, has been fundamental for increasing the reliability of simulation results [23, 45].
Within this context, in this Thesis the framework of multibody dynamic simulation is exploited for the study of the planetary ball mill, a grinding device where impacts play the key role.
However, it should be mentioned that there is another popular method for simulating interactions among moving bodies, the DEM. This technique, developed for the analysis of discontinuous materials [70], mostly addresses problems in granular flow and powder or rock mechanics (see *e.g.* [33, 67, 79, 80]). DEM and mutlibody dynamics share the same working principles but, generally speaking, while the former deals with a very large amount of small particles driven by gravity or kinematically simple machinery, the latter can simulate systems more complex in terms of motion but including a smaller number of parts. In principle, both the DEM and the multibody dynamics methods are suitable for simulating the planetary ball mill since this system involves a number of bodies not too large for the multibody and a kinematic that can be efficiently handled also by DEM. The choice of the multibody approach within this Thesis is chiefly motivated by (i) the simple management/modification of the kinematics and dynamics of the system given by the built-in joints as well as (ii) the possibility of using both native solids and CAD imported models for defining the geometry of the bodies offered by the software used, *i.e.* MSC.Adams [81], and by (iii) the larger diffusion that this method, allowing to simulate almost any mechanical system or component, can obtain in industry and scientific research areas dealing with mechanics. Furthermore, the employed multibody dynamics software, MSC.Adams, implements a robust but at the same time more straightforward contact scheme (although any formulation can be added by the user) than several DEM softwares, thus reducing the effort and the uncertainties related to parameters fitting. Finally, it is worth noting that the DEM has already been widely exploited for the simulations of the planetary ball mill (see *e.g.* [12, 18, 22, 82–84]) whereas, to the best of my knowledge, no models of this system in the framework of multibody dynamics simulation are reported in literature.

2.2.1 MSC.Adams contact model and parameters assessment

For a reliable simulation of the planetary ball milling process, impacts modelling plays a crucial role.
Particularly, the software employed within this Thesis, MSC.Adams [81], adopts the continuous approach

(see subsection 2.1.2) and therefore, once the contact among two bodies is detected, an impact force is added to the equations of motion. This force is expressed through the hard-coded *impact function* (but every other scheme can be added by the user), implementing the non-linear spring and linear damper scheme [45] (equation 2.20)

$$F = k\,u^n + c\,\dot{u}$$

However, to prevent discontinuities and avoid the previously reported side effects of this model, in contrast with the classic formulation, the *impact* function introduces a damping coefficient, c, which is not constant but dependent on the compenetration of colliding bodies, u, computed as the difference of a reference distance u_1 and the istantaneously measured distance between the centre of mass and the external surface of the colliding bodies u_2 (see left part of figure 2.4) [45, 81],

$$c = -c_m\left(\frac{u}{d}\right)^2\left(3 - 2\frac{u}{d}\right). \tag{2.20}$$

According to this function, sketched in the right portion of figure 2.4, c varies from zero (no compenetration) to a maximum value, c_m, applied when the compenetration is greater than or equal to d.

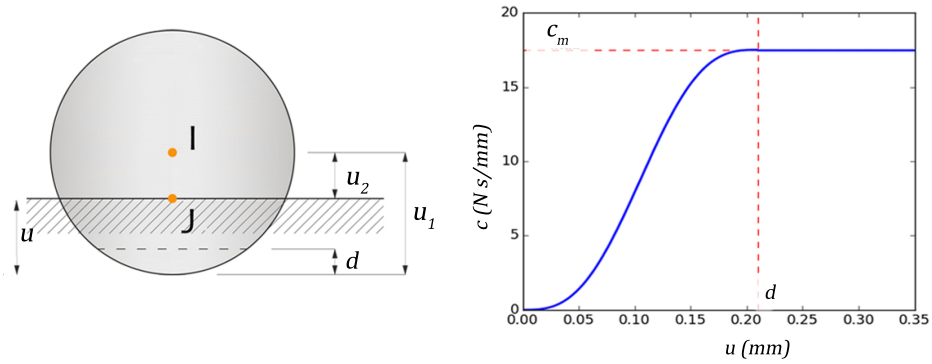

Figure 2.4: Left, definition of compenetration and right, trend of damping coefficient introduced in the MSC.Adams *impact* function as a function of compenetration. Differently from the standard formulation, defining a constant c, in the *impact* one this parameter varies as a function of compenetration among colliding bodies, u. *Adapted from [85].*

This contact scheme requires therefore the introduction of the parameters k, n for describing the elastic part of the contact force and c_m, d for the dissipative one.
A default procedure for parameters assessment is not defined and therefore the user can refer to every kind of method: from experiments to theory.
Hereafter the procedure developed in this Thesis is briefly explained.

Parameters assessment First of all it should be underlined that, although the planetary ball milling process is quite complex, involving a large number of collisions at different speed and angle, the contact model parameters were estimated for single impacts representative of the events occurring in the real scenario [84, 86], namely impacts among spheres and among spheres and the curved jar wall. The determined parameters were then extended to all the events involved in the process and, as will be shown in the next chapters, the overall contact dynamics was then validated through comparison against experiments.

For the contact model parameters assessment the impact between two spheres and between a sphere and a plate were considered, the latter assumed to approximate the collision of a ball with the jar wall, being the ball radius much smaller than the jar one.

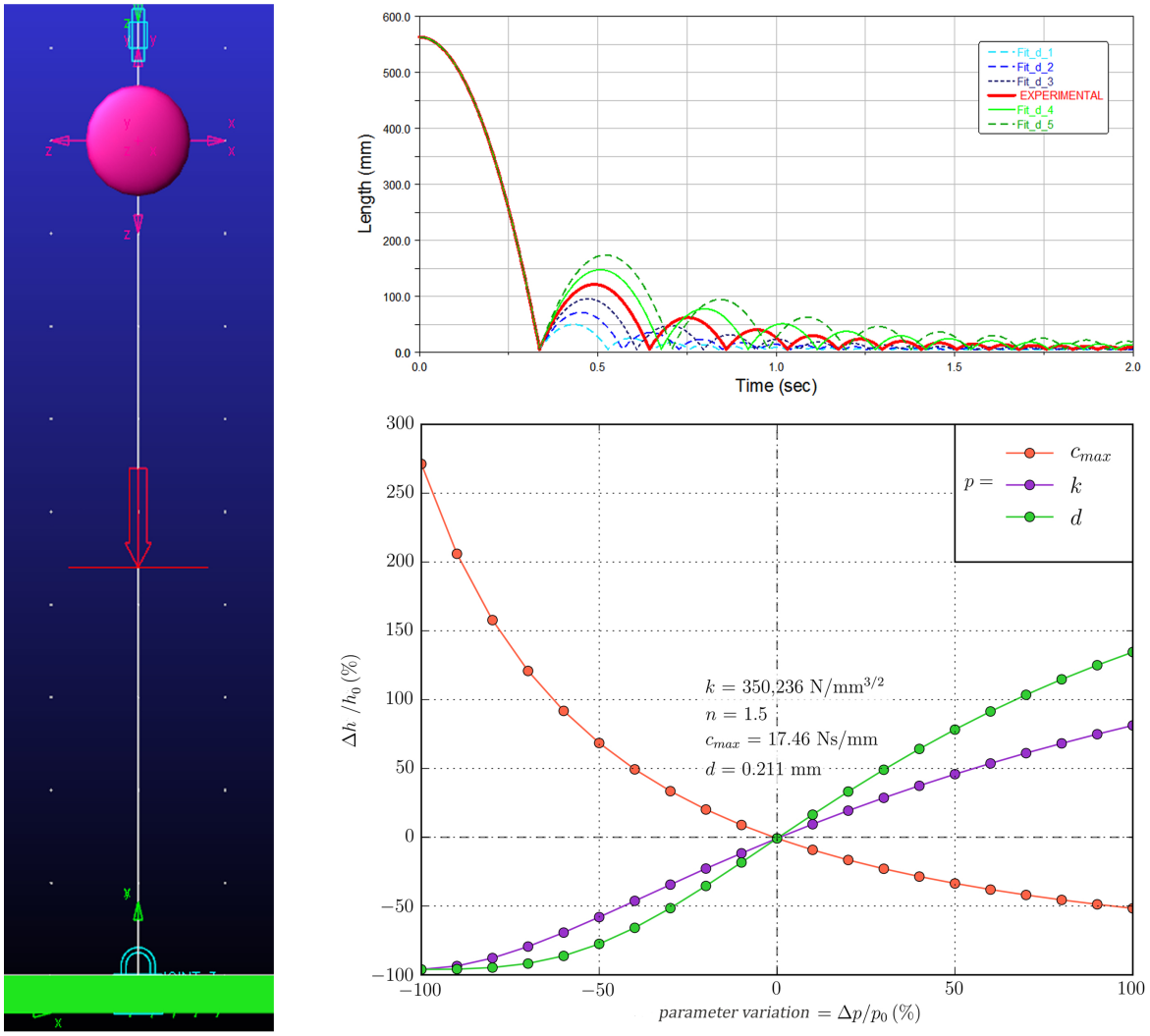

Figure 2.5: Left, simulated ball-on-plate drop test. Right-bottom analysis of the effect of each parameter introduced in the *impact function* on the first rebound height of the ball, h^*, provided by simulations. Starting from the first-estimate values, parameters were varied of $\pm$ 50 % and, for each simulation, h^* was measured (the figure reports the variation of this quantity expressed as $\Delta h = h^* - h_0/h_0$). It can be noticed that c and d have the larger influence on this variable. Right-top, d fitting of h^*. Results here reported refers to case study of a 12mm diameter steel ball dropping from $h_0 = 500$mm on a steel plate. *Adapted from [85].*

Being the MSC.Adams *impact function* formulation related to the non-linear spring and linear damper model, the theoretical expressions previously presented for this case were exploited to estimate k, n and c_m. Starting from the sphere-plate case, the generalised stiffness k and the n exponent were deduced from the Hertz theory (see non-linear Hertz contact model paragraph) and particularly n=3/2 was fixed whereas k was computed according to equation 2.11. For estimating c_m instead, the expression 2.16, proposed for the linear damper, was used introducing (i) the value of e provided by the drop test experiments reported

in subsection 2.1.1 (ii) k^* derived from the equation by Di Maio *el al.* (equation 2.17) and (iii) equivalent mass $1/m_e = 1/m_{sphere}$ since m_{plate} should be considered ∞ for this kind of collisions [26, 87].
Being d a feature of the MSC.Adams code, no suggestions for its estimate are provided in literature and therefore a first-tentative value was fixed according to considerations about the materials properties, the dimensions of the bodies and, in turn, the expected compenetration.
While calculations provided a reasonable first-order guess, experiments – more complicated but without simplifying assumptions in theories – were used to validate results. Particularly, as suggested by literature [84, 86], the ball-on-plate drop test was exploited, providing with the first rebound height of the dropping sphere, h^* (see subsection 2.1.1).
This experiment was simulated (see left portion of figure 2.5) – for a dropping height, h_0, chosen as representative of the impact velocities that can take place in the ball milling process – introducing in the *impact function* the first-tentative parameters determined from the above-described methods. h^* was extracted from simulation results and compared with the corresponding experimentally measured value. Since no match was found, further simulations were performed varying d until the correspondence among numerical and experimental h^* was reached (see top-right part of figure 2.5). It should be specified that d was adopted as fitting variable since (i) a parametric analysis on the effect of each contact model parameter on the variation of h^* was performed (bottom-right part of figure 2.5) and it pointed out that the dissipative terms mostly influence this quantity and (ii) it was chosen over c since no analytical first-guess expressions are available for its estimate.
For contact model parameters assessment for the impact among spheres, the same methods were adopted. However, being sphere-on-sphere experimental drop tests hardly performable with the apparatus showed in subsection 2.1.1, as a first-order approximation, the value of e derived from sphere-on-plate tests was introduced in equation 2.16 to compute c_m. Subsequent drop test simulations showed a rebound h^* approximately 20% higher than for the sphere-plate case, which is quite in agreement with the differences in terms of mass, geometry and stiffness among these 2 cases [26, 88–90]. Beside the contact force, MSC.Adams allows to account for friction at contact location through the following hard-coded regularised expression of the Coulomb model (see the paragraph on friction models),

$$\mu = \begin{cases} \mu_s \left(\dfrac{\dot{u}_t}{\dot{u}_{ts}}\right)^2 \left(3 - 2\dfrac{\dot{u}_t}{\dot{u}_{ts}}\right) & 0 \le \dot{u}_t < \dot{u}_{ts} \\ \mu_s - (\mu_s - \mu_d)\left(\dfrac{\dot{u}_t - \dot{u}_{ts}}{\dot{u}_{td} - \dot{u}_{ts}}\right)^2 \left(3 - 2\dfrac{\dot{u}_t - \dot{u}_{ts}}{\dot{u}_{td} - \dot{u}_{ts}}\right) & \dot{u}_{ts} \le \dot{u}_t < \dot{u}_{td}, \\ \mu_d & \dot{u}_t \ge \dot{u}_{td} \end{cases} \tag{2.21}$$

gradually varying from the static μ_s to the dynamic μ_d friction coefficient as a function of the tangential relative velocity of colliding bodies $\dot{u}_t$, as illustrated in figure 2.6 (but it should be noticed that any other friction model can be implemented by the user).
The required stiction ($\dot{u}_{ts}$) and friction ($\dot{u}_{td}$) velocities, representing the transition from sticking to sliding, were assumed low enough to allow a quick passage to sliding so to mimic the standard formulation of the Coulomb model (see figure 2.2) and ensure the application of a sliding friction force also at relatively low impact tangential velocities, as those typically developing during the planetary ball milling process.
For μ_d instead, the results of the pin-on-disc tribological tests (reported in subsection 2.1.1) were used whereas μ_s was deduced from literature.

Integrator settings Other aspects strongly influencing the results of the simulation are the settings of the integrator and the calculation step (time step). For the integrator several formulations are available in MSC.Adams and in this Thesis the Hilber-Hughes-Taylor (HHT) one was adopted being very well suited

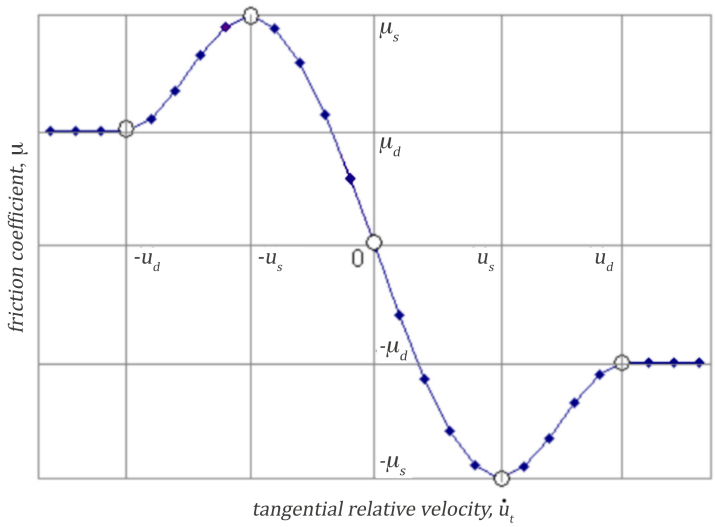

Figure 2.6: MSC.Adams formulation of the friction Coulomb model. Friction coefficient varies as a function of the tangential relative velocity, $\dot{u}_t$. *Adapted from* [81] – user manual.

for problems involving impacts (see [81] – user manual). Among the multitude of parameters that can be tuned by the user, the effects on the solution of (i) *error*, representing the allowed integration tolerance, (ii) h_{max}, indicating the maximum integration time step permitted and (iii) *step*, governing the output frequency (number of calculation points dumped to a file per second of simulation), were investigated. Simulations of the ball-on-plate drop test, systematically varying the above mentioned parameters, were performed until reproducibility of the solution in terms of trajectory of the bouncing sphere was achieved: maximum *error* and h_{max} ensuring this result were adopted. The *step* value instead, was chosen so that both a good description of the events was given and the size of the output files was not tremendously huge. It should be noticed that, this variable is also closely related to the time step, the latter being equal to 1/ *step* if h_{max} is not defined. On the other hand, even if h_{max} is set, to provide a more accurate solution in case of especially complex events (*e.g.* impacts), MSC.Adams reduces automatically the time step below h_{max} (adaptive time step) and, proportionally, increases the number of output points describing the event [81]. The number of calculation and output points per second of simulation therefore strictly depends on these variables as well as on the complexity of the modelled process and consequently it is not completely controllable by the user.

2.3 Impact of two spheres: comparison of analytically and numerically computed velocities

To validate the previously proposed procedure for parameters assessment and, in turn, the modelling outcomes, for the simple case of the impact among 2 perfectly smooth spheres (*i.e.* the effect of friction is neglected) a comparison among the simulated and analytically computed final relative velocities (*i.e.* at the end of the impact event) of the two bodies (sf_1 and sf_2) is proposed in figure 2.8.
In the reported scenario the relative initial velocity of the two bodies along the x-direction, v, (see top-left portion of figure 2.8) was set to 3300mm/s whereas their relative initial position, Δ, was varied, so to simulate different impact conditions. Particularly, as depicted in the right part of figure 2.8, distances between the centres of mass of the two spheres along the y-direction (Δ) equal to 0, 3, 6, 9 and 12 mm were investigated. Adopted geometrical and material properties of the spheres are reported in table 2.3.

Spheres: geometrical and physical properties	
material	steel
radius	6mm
density	7.85g/cm^3
Young modulus	200GPa
Poisson ratio	0.29
mass	7.1g

Table 2.3: Geometrical and physical properties of spheres used to compute both analytically and numerically the velocity at the end of an impact event (final velocity) for the case of study here reported.

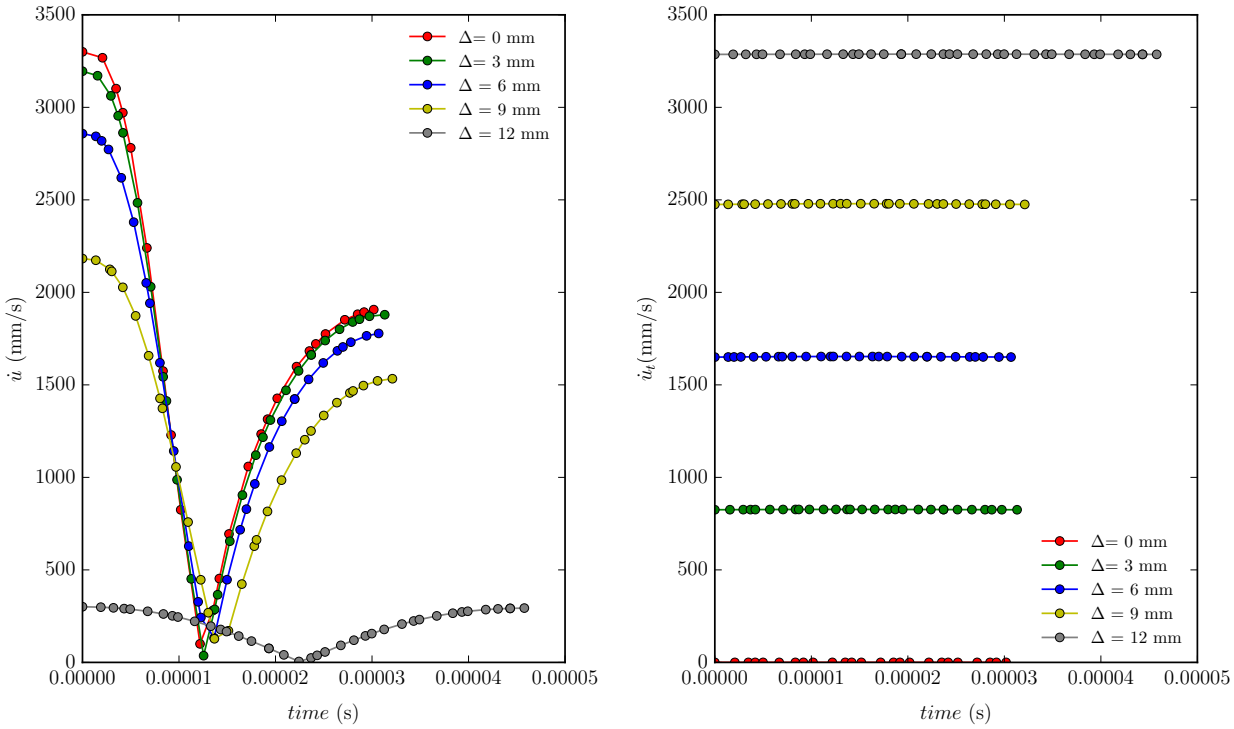

Figure 2.7: Profiles of normal and tangential components of relative velocity of two colliding spheres derived from multibody dynamics simulations for different relative initial positions Δ of the two bodies. Output points dumped by the simulator (which number is not fixed but depends both on integrator and output settings as well as on the complexity of the impact event) are reported on each velocity profile, with the latter corresponding to the relative velocity at the end of the interaction $\dot{u}_f$.

The effect of friction was not taken into account and therefore for the analytical calculations equations 2.3 and 2.4 were exploited to compute the final velocities of the bodies $v_{j,f}$, both in normal and in tangential direction with respect to the impact reference frame, and the relative final velocity $\dot{u}_f = v_{2,f} - v_{1,f}$. The same quantity was extracted from the outcomes of Msc.Adams multibody dynamics simulations, performed adopting the contact model and integrator parameters reported in table 2.4 and determined through the procedure described in the previous subsection.

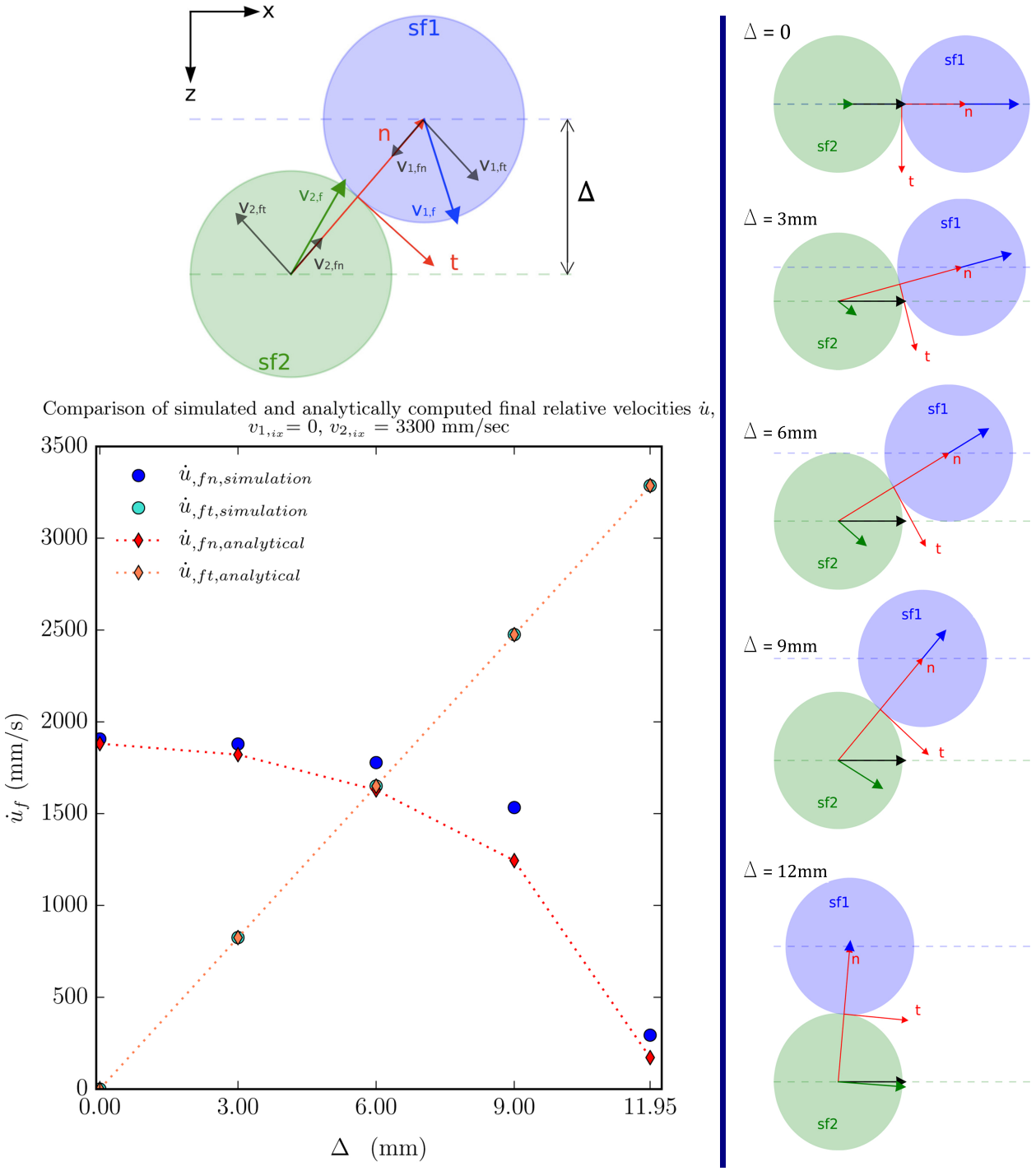

Figure 2.8: Bottom-left, comparison of relative velocities at the end of the impact ($\dot{u}_f$) analytically computed and retrieved from multibody dynamics simulations for the case study of two colliding spheres. Initial relative velocity was fixed while relative position Δ was varied. The five tested Δ values are depicted in the right part of the present figure. The top-left part shows instead the reference frame and the components of velocity of bodies along the impact axis, being n the normal and t the tangential component (for the complete definition of the velocity components see subsection 2.1.1).

Contact model and integrator parameters	
k	252,146N/mm$^{3/2}$
n	1.5
c	10.1kg/s
d	0.211mm
e	0.516
h_{max}	1E-6
error	1E-6
step (per second)	100

Table 2.4: Contact model and integrator parameters for 2 steel colliding spheres employed in the presented analyses

As illustrated in figure 2.7, simulations provided with the full description of the profiles of the normal and the tangential components of the relative velocity during the contact event, for every tested value of Δ. In agreement with predictions of equation 2.1, the tangential component of the relative velocity remains constant during the whole duration of the impact and its magnitude grows with Δ while the initial and, in turn, the final normal component reduces with the increase of Δ.
The comparison of analytically and numerically computed values of final relative velocities of colliding bodies, $\dot{u}_f$, is reported in the bottom-left portion of figure 2.8, highlighting a good agreement between the two approaches and therefore validating the effectiveness of the simulations and, at the same time, of the method for contact model and integrator parameters assessment. It is finally worth noting that variables reported in table 2.4 are going to be adopted for the simulations of the ball milling process in chapters 3 and 4 for modelling the impacts among spheres since objects with the same geometrical and physical properties will be used. For ball-plate impacts as well as for other investigated materials, the methods here presented have been followed for determining and validating the contact force parameters.

Chapter 3

Planetary ball milling modelling

• ○ • ○ • *Part of this section has been adapted from [91, 92].*
As briefly introduced in the previous chapters, the planetary ball mill (see figure 3.1) is one of the most exploited apparatuses for grinding materials down to the nanoscale, providing both for comminution and incorporation of defects.
It features straightforward handling, cleanability and moderate costs but, above all, high efficiency and versatility, therefore being well suited for processing almost any kind of material, from metals and ceramics to organic compounds and pharmaceuticals [9, 12, 13, 93, 94].

Figure 3.1: The Fritsch P4 planetary ball mill. In the middle, two jars installed on the plate; on the right, (top) detail of the jars, (bottom) an open vial with milling media and mill charge.*Adapted from [85].*

Selected typical applications

In the field of metals, the planetary ball mill is mainly exploited for the mechanical alloying. This method was initially applied to the production of oxide dispersion strengthened Ni-base superalloys (*e.g.* yttrium oxide and the superalloy) and later it was extended to other materials [8, 95, 96]. During the process, due to material transfer, the mixtures of powders milled together turn into an homogeneous alloy and, with respect to other techniques, finer and more homogeneous nanocrystalline structure can be obtained [95, 97].

On the other hand, ceramic materials can be synthesized either (i) indirectly or (ii) directly [9] in this apparatus. While the former route promotes enhanced reactivity of starting materials (owing to morphological, structural and/or chemical modifications) [98] and/or their deagglomeration [99], therefore improving the consecutive thermal treatment, the latter results in the direct manufacture of the desired end-product [100–103]. This is usually nanostructured, characterized by a selected polymorph [104–106], and affected by defects which are exploited to tune selected properties [10, 107]. Furthermore, ceramics can be incorporated into different matrices by ball milling, so to enhance mechanical properties [108].
Planetary ball mill is then largely applied also in the pharmaceutical industry, currently facing the challenge of enhancing the dissolution and bioavailability of poorly soluble drugs. The most common approach to assess this problem is increasing the surface free energy of drug particles by reducing their size and/or altering the morphological characteristics (*e.g.* shape, surface roughness, defects content ...) [11–13]. Planetary ball mill is very proficient in these tasks but it has also been successfully adopted for the development of more innovative technologies, *e.g.* for dry coating starches core particles with microparticulated drugs so to enhance the wettability and the dissolution rate [14].
To conclude this brief overview of planetary ball milling applications, it is worth highlighting that it has also proved to be effective in the mechanical exfoliation of bulk systems for the large-scale production of two-dimensional nanostructured materials - such as graphene and boron nitride nanosheets [15, 16], nowadays of utmost scientific and technological interest.

The planetary ball mill

Owing the name to the resemblance to the solar system motion, the planetary ball mill consists of two or more jars, rotating at angular velocity ω around their axis (rotation, see figure 4.11), installed on a disk simultaneously rotating at angular velocity Ω (revolution). ω and Ω can generally be independently controlled –with jars spinning faster– and they are limited by the design of the mill (*e.g.* for the Fritsch P4 planetary mill [109] in figure 3.1 maximum $\omega = 1200$rpm and $\Omega = 400$rpm). Jars and plate can be either co- or counter rotating but the counter direction is preferred in most cases, as it was demonstrated to be more effective in comminution [82].
Jars are filled with a customisable number of grinding balls and the mill charge. Different materials can be used for both the milling media (jars and balls), the more common being tungsten carbide, steel, zirconia, corundum or agate [12], carefully chosen so to avoid side reactions or high abrasion leading to contamination of the mill charge [8, 110]. Different sizes are also available, ranging from 0.1 to 40 mm for the balls and up to 500 ml volume for the jars [109], since up to now, planetary mills are built only on laboratory scale.
Inside each jar, grinding occurs by impacts among the milling media, driven by the field of centrifugal and Coriolis forces produced by the planetary-like kinematics, with mill feed particles typically covering balls and/or jar surfaces. Collisions intensity, direction, frequency and, consequently, the amount of energy transferred to the mill charge, are determined by balls movements that, in turn, strictly depend on the setup of the several operating parameters. These are related both to device geometry and to the physical properties of the jar and milling media and include *e.g.* size and shape of balls and jar, elasto-plastic and friction properties but also angular velocities, grinding time and charge fraction. A careful parameters assessment is of utmost importance, as it governs the nature and magnitude of the impulsive forces transferred by collisions and, therefore, the characteristics of the end product, both in terms of homogeneity and defects content as well as contamination, the latter being often the main issue of the process. With this in mind, the optimisation of the milling process has been investigated for a long time.
The most straightforward approach to correlate the milling parameters to the end product is running the mill under different conditions. Literature provides remarkable examples highlighting the effect of one or

more variables on *e.g.* resulting size [19], defectivity, homogeneity or phase structure [20, 21] of given materials. Among the others, the wide and highly systematic work of Gaffet for mechanical alloying should especially be mentioned [21], as it results in the construction of a so-called *parameter phase diagram*, presenting the phases forming for a specific materials system as a function of many milling parameters (milling time, temperature, rotation speeds).
The alternative to the brute-force empirical approach, deemed as expensive and time-consuming, is modelling the process, either (i) analytically (see *e.g.* [96, 111–115]) or (ii) numerically (see *e.g.* [18, 22, 83, 84, 116, 117]). The main advantage of modelling over experimental testing is the better understanding and control over kinematic and dynamic quantities (*e.g.* ball trajectories, kinetic energy etc...) under almost any possible operating condition, yielding predictions of the process results.
In the next section, a brief review on the development of the two categories of models is presented. Particular emphasis is given to the numerical ones, as this Thesis mainly deals with the development of a numerical model for the planetary ball mill implemented within the framework of the multibody dynamics.

3.1 Modelling approaches: a brief literature review

Analytical Models

A branch of the analytical models proposed in literature for the planetary ball mill focus on the estimate of the energy released during collisions and the work of Burgio *et al.* [111], published in 1991, is one of the most representative. In this work a single ball is assumed to move as an integral whole with a point on the jar circumference (without rolling or sliding) until, owing to a given composition of inertial forces, it is launched against the opposite point, perpendicularly to the jar surface. This results in a high velocity impact, after which the ball is again fixed to the jar wall. Kinematic equations describing the absolute velocity of the ball were developed so to compute the kinetic energy transferred to the mill system (*i.e.* mill feed and involved milling media) in a single collision event. Through the addition of correction factors, accounting for the presence of a finite number of balls and of the collision frequency, the expressions of the total energy and power were derived as a function of number, diameters and mass of balls, jar and disk diameter and angular velocities, filling ratio, weight of mill feed and milling time. Correlations among these quantities and results of mechanical alloying experiments were reported in a map, allowing to predict milling conditions giving an end-product with specific characteristics.
In the subsequent years, Burgio's model experimental validation was strengthened by their coworkers [112, 118, 119] comparing the computed total power with the electrical power that the mill needs to absorb exclusively for the grinding operation. This quantity, demonstrated to be dependent on milling conditions, was estimated by taking the difference between the power consumption measured running the mill equipped with an empty and a charged (with balls and powder) jar. A good agreement with computed values was found, under the assumption of power being almost completely transferred to the powder due to the inelasticity of collisions [120].
On the other hand, refinements of Burgio's equations were provided by Abdellaoui and Gaffet [96], proposing a new formulation of the criterion for the detachment of the ball from the jar wall, allowing a more rigorous calculation of the impact frequency. Furthermore, almost 10 years later, Chattopadhyay *et al.* [113] computed the normal and tangential components of the impact force at the collision point using the Hertz theory [30] and showed that the direction of the tangential one has an influence on impact effectiveness. Indeed, when it causes bodies in contact to spin in the same direction, the powder particles trapped between colliding bodies are forced to retain within the impact area, enhancing the grinding action of the impact. Authors also investigated the energy transfer and, unlike in the earlier works, the power spent in each collision for the elastic deformation of the ball was estimated.

While the cited studies mainly focus on the calculation of forces and transferred energy, in literature there are many other works aiming at mathematically describe the full trajectory of a single ball inside the jar as a function of the milling conditions.
In 1956, a first attempt was given by Joisel [121], who considered the development of an analytical solution too difficult and depicted the movement of a ball in graphical way. Analytical simplified calculations of ball trajectories were instead already available for the horizontal (tumbling) ball mill (see *e.g.* [7]) and, in 1963, Rumpf pointed out an analogy between balls motion inside this device and in the planetary one [122]. Starting from this consideration and assuming, as well as Burgio, a 2-phases ball trajectory (stationary and throwing phases [111]), in 1992 Raasch [114] derived 2 linear differential equations allowing the point-by-point calculation of ball movements depending on the angular velocities, radii of plate and jar as well as on the distance from the ball to jar centre. Boundary conditions, ensuring continuity at the detachment point, were determined exploiting the theory developed for the horizontal mills by Fischer [123] and Davis [124], assuming the detachment points to be located on a semicircle (the so-called Davis circle).
Also the work of Brun *et al.* [115] proposed an expression for the trajectory of a single ball and, according to the impact angle and the direction of the resultant force acting on the ball, identified 3 possible motion modes to appear at different jar-to-plate velocity ratios. The first one is characterised by the ball impacting and immediately leaving the jar surface while, on the contrary, the third does not foresee detachments. In the second regime instead, the ball follows the previously described 2-phases trajectory. The existence of these different motion patterns was confirmed by camera recordings of milling experiments but, according to the initial assumptions, the presented analytical model was capable of describing quite accurately only the second one.
However, simplifying hypothesis are almost inevitable for analytically handling the complex dynamics of the planetary ball milling process. In the aforementioned studies, the most restrictive one is that just one ball is considered and, in turn, the omission of the interactions among balls oversimplifies the kinematical and dynamical description of the real process. Also the kinetic energy transferred results underestimated since only ball-jar collisions are taken into account. Moreover, slip between jar wall and balls, inelasticity of collisions, deformation and friction at the contact point are neglected. It can therefore be concluded that analytical models are elegant and informative but, at the same time, limited by the necessary simplifications, often overlooking important phenomena.

Numerical Models

With respect to the analytical models, the numerical ones, although more computationally demanding, better preserve the complexity of the milling process, possibly giving more accurate predictions. They are also more flexible, allowing to quickly test and evaluate all the possible configurations of the system [70].
For the planetary ball mill modelling, the Discrete Element Method (DEM) is one of the most exploited technique. Just like multibody dynamics (see section 2.2), this method allows the analysis of discrete interacting bodies systems, providing the complete description of their dynamics (*e.g.* trajectories, velocities, accelerations) as well as all the quantities associated to each contact event (*e.g.* forces, contact points, relative velocities).
As already introduced in chapter 2, in both techniques, the integration of Newton's second law gives the motion of each element, resulting from the forces acting on it, and a force-displacement law, represented by a spring-damper scheme, is used to compute contact forces from displacement. Friction at contact location is also taken into account through suitable models (*e.g.* the Coulomb model).
The DEM method was developed in 1971 by Cundall [125] (and it was called the *Distinct Element Method*) and implemented into the *BALL* computer program [71]. It was first applied to the analysis of

the behaviour of granular assemblies (*e.g.* soil) [70] modelled as 2D disc, and validated comparing the computed forces with the results of photoelastic tests (presented in 1969 by Jong and Verruijt [126]).
Subsequently, with the dramatic increase of computer resources and numerical modelling popularity, DEM has been used for a large variety of applications, from rock mechanics to granular flow (see *e.g.* [33, 79, 80, 127–129]) and, since the 90's, it has also been applied to the investigation of the ball mills.[†]
Mishra and Rajamani first coded the scheme in the *2DMILL* computer program [84], later upgraded for dealing with 3D objects [130, 131]. In these works, authors particularly underlined the dependence of reliable computational results on the accurate choice of the contact force models and the associated parameters. Therefore, beside developing a new contact relation (the *elastic perfectly plastic contact model* [130, 132]), experimental procedures and formulas for determining stiffness, damping, and friction were suggested [84, 86, 130, 132].
Another main challenge in dealing with ball mill modelling is the simulation of the mill charge and 3 possible solutions have been proposed in literature [83]. The first one is explicitly modelling the powder particles as small spherical elements. However, this strategy requires enormous computational resources and simulation time (a huge amount of small elements would require a very small integration timestep to ensure the stability of the algorithm) and it is adopted in a few studies (*e.g.* [133]). The opposite approach is to totally ignore the mill charge and only model the grinding media [84, 116, 130]. However, this approach could result in a too rough estimation of the system dynamics since ball movements strongly relates to mill charge [18, 115]. The last and most exploited option lies in-between the previous ones and, in place of explicitly modelling the powder, assumes to include its influence by properly modifying the contact model friction and/or damping parameters [18]. According to Feng *et al.* [83], these variables may exhibit some randomness since they depend on the amount and the aggregation of the powder trapped between colliding bodies. Therefore, the authors proposed to adopt average values, estimated from the simulation of different impact configurations in a small scale local model, including two colliding elements and some powder particles (different configurations were modelled *e.g.* by changing the number and the arrangement of powder particles).
On the other hand, through a wide experimental campaign, Rosenkranz *et al.* demonstrated the possibility to account for the mill charge by only altering the friction coefficients [18], a method already introduced by Kano *et al.* [134]. High-speed videos of the planetary ball milling process were recorded for different kinds of mill feed and a significant change in balls movements was revealed owing to the formation of a powder coating layer on balls and/or jar, strongly affecting the friction conditions. Movies were qualitatively compared to the results, in terms of balls motions, of DEM simulations performed systematically varying the model friction coefficients and correlations among these parameters and the effect of the mill feed were found [18].
In addition to milling media motion analysis, simulation results can be exploited to compute several quantities allowing to quantitatively compare the effect of the operating parameters on the milling process and, in turn, predict the mill configuration providing with higher comminution of the mill charge.
Impact (or stress) energy is one of the most used quantities and, although many different formulations can be found in literature, it broadly estimates the maximum kinetic energy involved in collision events (see *e.g.* [12, 18, 82, 116, 117, 135, 136]), starting from the relative velocities of impinging bodies.
However, only a fraction of the so-computed energy is effectively involved into the grinding process, whereas the other is converted into heat, sound or particles motion. Due to the complexity of phenomena taking place during the ball milling process, the amount of energy transferred to the mill charge and actually used for comminute particles is therefore hardly estimable. Consequently, as a first order ap-

[†]It should be specified that the DEM is used for investigating all the class of ball mill apparatuses and not only the planetary one. However, within the scope of the Thesis, this short review mainly reports examples relating to the planetary ball mill.

proximation it is generally assumed that the rate of energy conversion to grinding is constant, meaning that a finer end product is expected to correspond to mill configurations giving higher energy [116].
Among the multitude of studies investigating the effect of milling variables by means of DEM and energy criteria, it is worth citing the studies of Mio, Kano and their coworkers, proposing some correlations among this quantity and experimental data. In particular, in [82, 117] jar and main disk rotating in counter-direction rather than in co-direction were shown to increase impact energy. The higher efficiency in comminution of this configuration was confirmed by X-Ray diffraction analysis of the end product. Indeed, patterns collected on talc ground under both the conditions revealed broader peaks (indicating smaller dimensions of the end-product crystallites) to correspond to counter-rotating jar and plate [82]. Further analyses pointed out that the energy also increases with the jar-to-plate velocity ratio till a critical value, when balls begin to roll along jar wall. However, this value can not be known in advance but it is influenced by the setup milling parameters *e.g.* the radius of the plate, that tends to shift it to higher velocity ratios.
Another work that it is worth citing is the one of Kano and Saito [22] focusing on the effect of ball diameter that, by means of a linear function, introduces a correlation between energy computed from simulations performed adopting different balls sizes and the rate of powder size reduction deduced from experiments.
Several other variables attracted the interest of researchers but, despite the amount of valuable contributions, no general rule can be established for the setup of optimal milling conditions for the planetary ball mill. Useful suggestions can be deduced from literature but every single case deserves specific attention. Optimisation of the process requires therefore the development of reliable tools and methods for a quick but, at the same time, careful case-by-case parameters assessment and numerical models are very well suited to this purpose, allowing to test every possible configuration in a reasonable time.

3.2 A multibody dynamics model of the planetary ball milling process

Hereafter a new numerical model for the planetary ball milling process is presented. Unlike the previous DEM-based works, it exploits the power of the multibody dynamics simulations that, as reported in section 2.2, are perfectly suited to motion analysis of mechanical systems. The discussed model is developed by using the software MSC.Adams [81], as it provides a feasible management of the kinematics and dynamics (*e.g.* every kind of mechanical joint and/or constraint and forces are predefined) as well as of the geometry (both native primitive solids and external CAD models can be used) of any modelled component, allowing to easily deal with complex mechanical systems. Furthermore, with respect to several DEM softwares (*e.g.* LIGGGHTS [137]), a robust but more straightforward contact scheme is implemented in MSC.Adams (but it should be mentioned that any other formulation can be added by the user), requiring less parameters, generally estimable through simple experiments, thus reducing the uncertainties of variables fitting.
The mill charge is not explicitly modelled since the presence of a large amount of very small particles can not be easily handled by this simulation technique and, besides, goes outside its scope. However, following the approach proposed by Rosenkranz [18], the effect of the mill feed is taken into account through suitable friction coefficients.
Contact model and friction coefficients as well as integration error, maximum timestep and output parameters are estimated through the procedure presented in subsection 2.2.1.
The model is here mainly exploited for investigating the effect of jar (ω) to plate (Ω) velocity ratio, defined as $\omega/\Omega + 1$. Counter rotating jar and plate are adopted and, therefore, jar velocity is taken with negative sign. The case of jar and plate rotating in the same direction was not considered in this study since it has been demonstrated to be less effective in terms of energy transfer and comminution [82].
Modelling predictions are validated around the case study of a brittle ceramic material, Calcium Fluoride

(or fluorite, CaF_2, commercial Carlo Erba c.d. 433587 powder). As will be better explained, fluorite was ground in a Fritsch P4 [109] planetary ball mill and X-Ray Powder Diffraction Line Profile Analysis (XRPD-LPA) was performed on milled samples so to investigate the microstructural evolution under mechanical grinding.
CaF_2 powder is particularly suitable for this kind of experiments as it presents a simple and stable crystalline structure that, during the milling process, does not undergo any phase transformation and/or reaction with contaminants [138].
While detailed information about this material can be found in [138], it is worth noting that the starting CaF_2 powder is mainly made of cubic particles with edge dimension between 2 and 10 μm as shown in figure 3.2a. A small fraction of pseudo-spherical particles with characteristic size of 10 μm, can be also observed (figure 3.2b). The composition declared by the producer, reveals the presence of a small contamination from MgO (approximately, 1.5wt% of MgO [138]), due to the process of calcination.

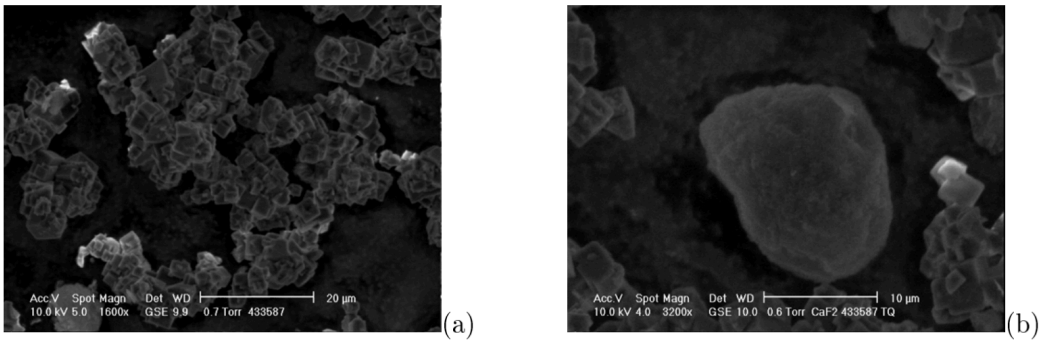

(a) (b)

Figure 3.2: Micrographs of CaF_2 pristine powder showing (a) the cubic and (b) the pseudo-spherical particles that composes it. *from [138]*

Typical quantities extracted from a X-Ray powder diffraction pattern are information on crystallite size and microstructure, *e.g.* in terms of dislocation content or stacking faults. It should be noted that the term crystallite refers to a coherent scattering domain, *i.e.* an ensemble of atoms approximately on the same crystal lattice, which often differs from particles observed by microscopy. Indeed, the latter are typically aggregates of crystallites, *e.g.* separated by grain boundaries, as sketched in figure 3.3.

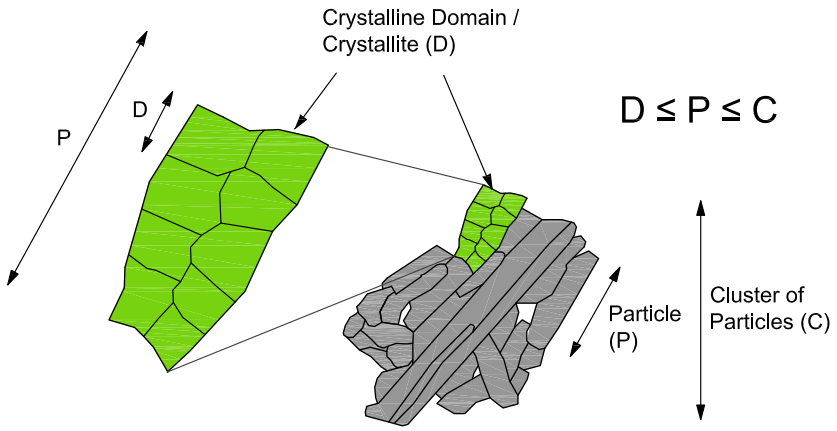

Figure 3.3: Sketch of particles and crystallites sizes. *Adapted from [139]., courtesy of P. Scardi*

In this Thesis, the Whole Powder Pattern Modelling (WPPM) [140–142] is adopted to extract information from powder diffraction patterns. This advanced analysis method is a perturbation approach which is applied to an initially perfect crystal model in reciprocal-space. A convolution of effects originating from the microstructure (*i.e.* any deviation from the ideal crystal) represents each peak composing the powder pattern. In particular, each effect is accounted for by an analytical expression, function of physical parameters. Among the available models, the crystallite size and shape, lattice distortions, dislocations and stacking faults should be mentioned.

Following, the paper [91], *Modeling of the planetary ball-milling process: The case study of ceramic powders* published in the *Journal of the European Ceramic Society* (Vol. 9, 2016) is reported, which summarizes the most important steps in the development and validation of the model together with the achieved results.

3.2.1 Modeling of the Planetary Ball-Milling process: the case study of Ceramic Powders

Authors: M. Broseghini, L. Gelisio, M. D'Incau, C. L. Azanza Ricardo, N. M. Pugno and P. Scardi.[†] *Adapted from [91].*

Abstract

A numerical dynamic-mechanical model of a planetary ball-mill was developed to study the dependence of process efficiency on milling parameters like ball size and number, jar geometry and velocity of the revolving parts. Simulations provide evidence of the correlation between milling parameters and the resulting microstructure of the ground material. In particular, maximum efficiency of the grinding process is observed with the most disordered ball motion, which is obtained within a well-defined range of jar to plate velocity ratios. As a significant case study in ceramic powder technology, the model is presented and discussed for calcium fluoride (CaF_2), ground under different conditions in a planetary mill, and then characterized by X-ray powder diffraction and scanning electron microscopy.

Introduction

High-energy ball milling is commonly used for particle size reduction (comminution) down to the nanometer scale [6, 8, 12]. Increased surface energy and defectivity lead to modified physical/chemical properties and can promote structural transformations and/or chemical reactions (see e.g. [7]). Nearly all materials can be processed, including metals [93, 99, 143], organics [94, 144, 145] and pharmaceuticals [146–148], as well as composites [149, 150] or low-dimensional structures [15, 151–154].
Ceramic materials can be produced either (i) indirectly or (ii) directly [9] *via* ball milling. While the former route promotes enhanced reactivity of starting materials (due to morphological, structural and/or chemical modifications) [98] and/or their deagglomeration [99], therefore improving the consecutive thermal treatment, the latter results in the direct manufacture of the desired end-product [100–103]. This is usually nanostructured, characterized by a selected polymorph [104–106], and affected by defects which are exploited to tune selected properties [10, 107]. Furthermore, ceramics can be incorporated into different matrices by ball milling, so to enhance mechanical properties [108]. Among high-energy ball mills, the planetary is a mechanically simple and versatile device for efficient grinding.

[†]In this work MB developed the model, performed the simulations, analysed the results and wrote the major part of the manuscript, LG and CLAR helped in data analysis and in drafting the manuscript, MDI conceived the idea, performed experimental tests and analysed part of the experimental data, NMP conceived the idea and revised the manuscript, PS conceived the idea, analysed experimental data and revised the manuscript.

It is usually made of two or more jars, rotating at an angular velocity ω around their axis (see figure 4.11), installed on a disk rotating at angular velocity Ω.
Grinding occurs by impact among the milling media (balls and jars), driven by centrifugal and Coriolis forces, with material particles typically covering balls and/or jar surfaces. The energy available for comminution and, in turn, the size of the ground particles and their defectivity, are determined by several parameters, related both to geometry and to physical properties of jar and milling media. These include size and shape of balls and jar, elasto-plastic properties and friction coefficients, but also angular velocities, grinding time and charge fraction. Products homogeneity and contamination from the vials are also related to the above-defined parameters and must be properly accounted for.
The (i) straightforward approach to correlate milling parameters to end products is running the mill under different conditions. The alternative to this brute-force, time consuming empirical approach is modelling the process, either (ii) analytically [96, 111, 114] or (iii) numerically [18, 22, 83, 84, 116, 117]. The main advantage of modelling over experimental testing is a better control over kinematic and dynamic quantities, *e.g.* ball trajectories and kinetic energies, under all possible operating conditions. Analytical models are elegant and informative, but most often limited by simplifying assumptions, like inelasticity of collisions or approximate friction models. Numerical multibody models, although more computationally demanding, can preserve the full complexity of the milling process and possibly provide more accurate predictions. This work introduces a model belonging to the latter category, implemented within the framework of a multibody dynamics software. The validity of the model has been verified considering the case study of a typical ceramic material, calcium fluoride.

The model

Following, the model of a planetary ball mill Fritsch Pulverisette 4 (P4, [109]) ball mill is presented. The solution of the equation of motion of the milling media is obtained, implementing a suitable model for contacts and Lagrangian description, by the software MSC.Adams [81]. One of the most appealing features of this multibody dynamics software is the aptitude for handling complicated mechanical systems, therefore allowing a detailed description of different processing apparatuses. Due to its limited volume fraction, powder charge has not been explicitly modeled but accounted for by a suitable choice of collision contact parameters [83], as will be discussed later.

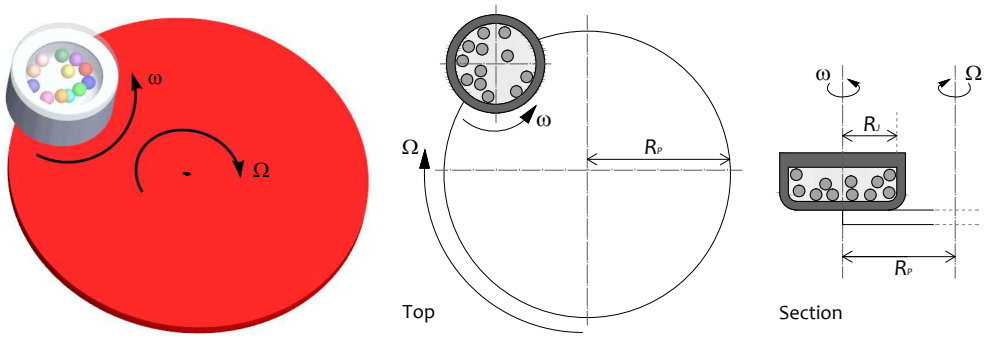

Figure 3.4: Schematic representation of a planetary ball-mill. Right, three-dimensional view; middle and left, definition of the jar radius R_j and the distance between axis of rotation (angular velocity ω) and revolution (angular velocity Ω) R_p.

The Hilber-Hughes-Taylor (HHT, [155, 156]) integrator, with automatic step tuning, was adopted setting a maximum numerical error of 10^{-8}.

The mill The angular velocities ω and Ω (see figure 4.11) were applied, respectively, to the two hinges (features predefined in the MSC.Adams software) connecting (i) the jar (radius R_J) to the main disk (radius $R_P = 125$mm) and (ii) the latter to the ground reference frame.
Milling media were randomly placed inside the jar, in the gravitational field, and angular velocities were gradually increased to the target values during the first second of simulation, which lasted overall twenty-four seconds. To allow motion homogenization, the first four seconds were discarded during data analysis.

Jar (AISI 304)		Spheres (AISI C1020)	
radius	32.5mm	number	12
volume	80cm^3	radius	6mm
density	8.03g/cm^3	density	7.85g/cm^3
Young modulus	193GPa	Young modulus	200GPa
Poisson ratio	0.29	Poisson ratio	0.29

Table 3.1: Geometrical and physical properties of jar and milling media for the presented case study.

Contact modeling The most critical ingredient in the model of a ball mill is the contact law.
Contact models belong either to the (i) discrete or (ii) continuous approach [25]. While (i) is based on momentum balances, in (ii) a force-displacement law is added to the equation of motion, a combination of a spring in parallel with a damper, causing energy dissipation, plus a friction element. The most significant formulations are based on a combination of either linear or non-linear spring or damper but more complicated schemes, such as those based on Mindlin's work or on the introduction of plasticity, have also been proposed [18, 25, 26, 62, 72].

The contact force is defined by the hard-coded *impact function* [81], based on the non-linear spring (F_k) and linear damper scheme (F_d) proposed by Dubowsky and Freudenstein (impact pair model, [72]),

$$F_c = F_k + F_d = ku^n + c\dot{u}, \tag{3.1}$$

being u and $\dot{u}$ the relative displacement and velocity of the colliding bodies, whereas k and c are the spring stiffness and the damping coefficient. With respect to the above formulation, to prevent discontinuities, the impact function defined within MSC.Adams implements a damping coefficient which depends on the relative displacement of colliding bodies,

$$c = -c_m\left(\frac{u}{d}\right)^2\left(3 - 2\frac{u}{d}\right), \tag{3.2}$$

and varies from zero to c_m when the relative displacement is greater than or equal to d. With the exponent $n = 3/2$, an estimate of k can be derived from the Hertzian theory of contact [26],

$$k = \frac{4}{3\pi}\left(\frac{1}{\eta_i + \eta_j}\right)\sqrt{\frac{R_i R_j}{R_i + R_j}}, \tag{3.3}$$

for the contact between sphere i and j, with radius R, and

$$k = \frac{4}{3\pi}\left(\frac{1}{\eta_i + \eta_j}\right)\sqrt{R_i}, \tag{3.4}$$

for the contact between sphere i and a plane (jar surface). The parameter $\eta_i = \left(1-\nu_i^2\right)/\pi E_i$ accounts for elastic properties of materials, being ν the Poisson ratio and E the Young modulus. The solution of the classical problem of damped vibration of a mass spring system provides a guess of the damping parameter [72],

$$c_m = -2\ln(e)\sqrt{\frac{1}{\ln^2(e)+\pi^2}}\sqrt{m_e k^*}, \tag{3.5}$$

being $e = \sqrt{h/h_0}$ the restitution coefficient, accounting for the difference from initial (h_0) and final (h) height in a drop test, $1/m_e = 1/m_i + 1/m_j$ and k^* [61],

$$k^* = \left(\frac{320}{81} m_e \dot{u}_{n0}^2 E_e^4 R_e^2\right)^{1/5}. \tag{3.6}$$

Geometrical and elastic properties are expressed, respectively, as $1/R_e = 1/R_i + 1/R_j$ and $1/E_e = 1/E_i + 1/E_j$ whereas $\dot{u}_{n0}$ is the relative velocity during the collision, assumed to be an average value for the discussed model.

sphere-sphere generalized contact stiffness, k_{ss}	252,146N/mm$^{3/2}$	eq.3.3
sphere-plane generalized contact stiffness, k_{sp}	350,236N/mm$^{3/2}$	eq.3.4
restitution coefficient, e	0.516	drop test, $e = \sqrt{h^*/h_0}$
relative impact velocity, $\dot{u}_{n0}$	3,309mm/s	statistical analysis of velocities
sphere-sphere contact damping, $c_{m,ss}$	10.1kg/s	eq.3.5
sphere-plane contact damping, $c_{m,sp}$	17.5kg/s	eq.3.5
full damping penetration depth, d	0.211mm	fit of experimental drop test results

Table 3.2: Values used for the contact model and method used for their derivation.

While calculations provide a reasonable first-order guess, experiments can account for simplifying assumptions in theories. The most straightforward approach is comparing a simulation of a drop test (ball impinging on a plane) against experimental results [84, 86], measuring the first rebound height (h) and fitting d. This implies that some spread in the damping parameter is introduced depending on the compenetration. Even if more refined contact models exist, it is worth noting that physical insights can be captured also from simpler (but more robust) schemes. Dealing with more complicated descriptions of phenomena is conditioned to a rigorous and extended procedure of parameters fitting.

Among the possible schemes to account for friction at the contact location, the Coulomb model (hardcoded in MSC.Adams) was implemented. In this case, parameters are the static (μ_s) and dynamic (μ_d) friction coefficients. Again, to avoid discontinuities MSC.Adams expresses the friction coefficient as a function of the slip velocity (v),

$$\mu = \begin{cases} \mu_s \left(\dfrac{v}{v_s}\right)^2 \left(3 - 2\dfrac{v}{v_s}\right) & 0 \le v < v_s \\ \mu_s - (\mu_s - \mu_d)\left(\dfrac{v - v_s}{v_d - v_s}\right)^2 \left(3 - 2\dfrac{v - v_s}{v_d - v_s}\right) & v_s \le v < v_d, \\ \mu_d & v \ge v_d \end{cases} \tag{3.7}$$

therefore gradually varying from the static to the dynamic values.

	Steel-Steel	Steel-Fluorite	
μ_s	1.0	0.25	literature
μ_d	0.8	0.2	tribological test
v_s	1mm/s	1mm/s	statistical analysis of velocities
v_d	10mm/s	10mm/s	statistical analysis of velocities

Table 3.3: Friction coefficients, stiction (v_s) and friction (v_d) transition velocities used in the simulation. Pin-on-disc tests were performed using CSM tribometer [51].

Results and discussion

Calcium fluoride (CaF_2) was ground using the above-described mill under several operating conditions (reported in the following paragraph) and ball milling effect was indirectly assessed by a rigorous characterization of the processed material either by (i) Scanning Electron Microscopy (SEM) and (ii) X-ray Powder Diffraction Line Profile Analysis (XRPD-LPA, [157, 158]). Concisely, the latter consists in extracting structural and microstructural information from the width and the shape of diffraction peaks through suitable models. XRPD data were therefore analyzed by the Whole Powder Pattern Modeling approach (WPPM, [140–142]), so to provide the distribution of crystalline domains (assumed to be spherical) sizes, in terms of average ($\langle D \rangle$) and standard deviation of a lognormal size distribution, and dislocation density (ρ), expected to increase as a result of the milling procedure [93, 159–164]. The more the process is protracted in time, the more the average crystallite dimension decreases and the density of defects increases.

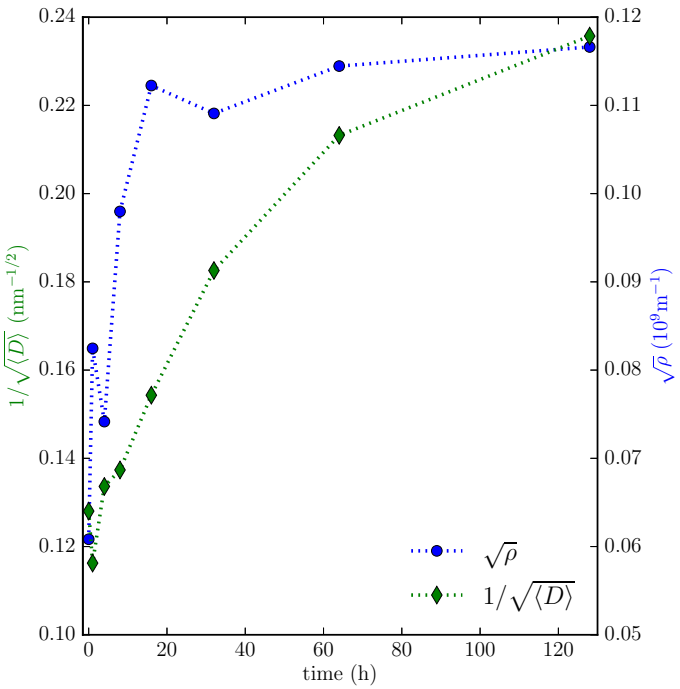

Figure 3.5: Average crystallite size ($\langle D \rangle$) and dislocation density (ρ) as a function of the milling time presented from the point of view of the Hall-Petch law (yield stress) and Taylor equation (work hardening) [165].

Interestingly, $1/\sqrt{\langle D \rangle}$ is related to the yield stress (σ_y) through Hall-Petch law [166, 167] and $\sqrt{\rho}$ is connected to the work-hardening through Taylor equation [168]: qualitatively, figure 4.12 illustrates the increasing in yield stress and work-hardening as a function of milling time.

Analysis of results Computer simulations provide the complete set of dynamical variables for each milling body as well as quantities associated to each contact event, therefore allowing an outright understanding of the the time evolution of the investigated system. Naturally, visual inspection of trajectories provides information on (i) motion regimes and (ii) regions characterized by high impact frequency and/or intensity, therefore potentially prone to significant wear. Moreover, each computed quantity can be broken down with respect to the local impact reference frame, therefore allowing to design the preferential direction for stress exchange. For example, exfoliation of graphite can be enhanced if shear load is preferentially transferred [15, 16, 152]. To quantitatively characterize each simulation, two parameters have been used. First one, the specific impact energy (or impact power, E_I/τ) computed in the impact reference frame [18, 22, 26, 82, 117, 136], provides an estimate of the amount of energy available for grinding the mill charge

$$\frac{E_I}{\tau} = \frac{1}{2\tau}\sum_{j=1}^{C}\frac{m_{1j}m_{2j}}{m_{1j}+m_{2j}}\,\dot{u}_j^2, \tag{3.8}$$

where m_i is the mass of the i-th colliding body, $\dot{u}$ the relative velocity and C is the number of points sampling collisions during the simulation time period (τ) with mean output step size of $\approx$ 1E-3 (resulting from setting MSC. Adams software integrator parameters $h_{max} =$ 1E-6 and $step = 100$). It should thus be stressed that the absolute scale for the power, implicitly depends on the choice of the integrator parameters and therefore it is arbitrary and not directly comparable with power available in a real apparatus [169] [†].
The relative velocity, and in turn the specific energy, can be decomposed into a normal ($\dot{u}_n$) and a tangential ($\dot{u}_t$) component with respect to the impact reference frame.
The second parameter provides a geometrical view of the simulation. Inspired by statistical mechanics, given the number of milling media N and the jar volume V, the Cylindrical Distribution Function (Cylindrical Distribution Function (CDF)),

$$g\left(r\right) = \frac{1}{2\pi h r \Delta r}\frac{V}{N}\left\langle \sum_{i=1}^{N}\delta\left(\mathbf{r}_i\cdot\hat{r} - r\right)\right\rangle_{\tau}, \tag{3.9}$$

expresses the time-averaged density of milling media as a function of the distance from the jar axis ($\mathbf{r}_i\cdot\hat{r}$ for the i-th body), *i.e.* the probability of a given cylindrical shell having width Δr of being occupied ($\delta\left(x\right)$ is the Dirac's delta function and $\langle\rangle$ indicates the time average over the period τ). For a cylindrical jar, the more the CDF is uniform across the radius, the more the motion is random and the mean free path is large. To condense the randomness of motion, *i.e.* the absence of strong localization of milling media, in a single parameter, the reciprocal of the variance of the CDF histogram ($1/\sigma$) has been evaluated: the more uniform is the $g\left(r\right)$ the larger is $1/\sigma$ whereas, the more localized is the motion the smaller is $1/\sigma$.

Simulations Within the wide set of parameters characterising the process, in this work the effect of jar (ω) and plate (Ω) velocities on milling efficiency has been investigated. Following the approach by Rosenkranz *et al.* [18], the mill feed was accounted for by modifying friction coefficients, μ_s and μ_d (see

[†] In the original printed version C was not correctly defined. The proper description of this quantity here reported can be found in [169]

table 3.3). The observation was derived from the analysis of camera images revealing the formation of powder coating layers on balls and jar surfaces, strongly modifying friction conditions. It is also worth noting that for the presented case the powder charge volume is much smaller than that of the milling chamber and balls (volume fraction $< 1\%$), so that the powder layer should not substantially affect restitution and thus the damping coefficient. Therefore, two extreme conditions have been simulated, namely characterized by (i) steel-steel and (ii) steel-fluorite friction coefficients. Moreover, to maximize energy exchange, jar and plate were rotated counter-clockwise [82].

Figure 3.6 illustrates the outcome of selected simulations ($\omega = -320, -600, -800$ rpm and $\Omega = 200$ rpm), illustrating both trajectories and the CDF for different motion regimes. In the first column, above-mentioned quantities are computed for a low jar velocity ω: as made apparent from the trajectories, motion is not random and space regions of higher occupancy are present. Consequently, the CDF is not uniform. With respect to the previous case, the motion described within the second column is more random, with trajectories across the whole jar (longest mean free path), so that the observed CDF is nearly uniform. The last case, corresponding to high jar velocity, as clearly shown by trajectories, is characterized by balls chiefly sticking to the jar surfaces and consequently probability of crossing some regions is far from being uniform.

The specific impact energy (or impact power, equation 3.8) for a set of simulations performed at different fixed value of plate angular velocity Ω for the steel-steel interaction case is reported in figure 3.7a. Interestingly, the effect of this parameter only affects the total amount of kinetic specific impact energy involved in the process whereas it does not alter the location (in terms of $\omega/\Omega + 1$) of the maximum energy exchange (corresponding to the central column in figure 3.6), therefore suggesting that for the specific set of coefficients (representing the interaction between two specific materials) it is the geometry of the system that determines the most efficient milling condition. Particularly, it exists a critical ratio of angular velocities (expressed as $\omega/\Omega+1$) corresponding to the maximum energy transfer: with respect to figure 3.6, ball motion is disordered, with trajectories across the whole jar, below this threshold (cascading to cataracting regime), whereas, above it, balls tend to stick to the jar surfaces (rolling).

As anticipated, the specific impact energy can be separated into a normal and tangential component with respect to the local impact reference frame. Figure 3.7b depicts equation 3.8 computed for the above-described set of simulations performed at $\omega = 200$ rpm. The contribution of the tangential component is higher, but the two trends are qualitatively similar, with the maximum of energy exchange corresponding to the same $\omega/\Omega+1$ abscissa of ≈ 2.6. The geometrical parameter, quantifying the randomness of motion of the milling media inside the jar and, in turn, the mean free path, is reported in figure 3.8a. Again, the location of the maximum is shared across simulations with different plate angular velocities and its value does not show a significant dependency on Ω. A comparison between the energetic and geometrical parameters is shown in 3.8b for the steel-steel interaction case at $\Omega = 200$ rpm: the qualitative agreement of the two demonstrates that the more random is the motion, the higher is the energy exchange.

So far, only the steel-steel interaction (no powder charge) has been considered. To validate the model, a comparison of simulations and experimental results, *i.e.* grinding of calcium fluorite, was performed.

The effect of the presence of the ceramic powder in the milling system was taken into account by modifying the parameters of the friction contact model (see Table 3.3): figure 4.17 illustrates the comparison between the specific impact energy computed for simulations performed at $\Omega = 200$ rpm using both coefficients representing the no-feed (red) and the fluorite powder (grey) cases. As demonstrated in the plot, fluorite presence is responsible for a shift of the maximum energy exchange condition, from $\omega/\Omega + 1 \approx -2.6$ to ≈ -3.0, and an increasing amount of energy exchanged. The same figure also reports some interesting experimental results for fluorite powder ball-milled in a P4 mill under the same nominal conditions as in the simulations. Experimental data, as provided by LPA of the XRPD patterns, are proposed in terms of average crystallite dimensions (sphere diameter) $\langle D \rangle$, and dislocation density, ρ. In particular the Hall-Petch trend ($1/\sqrt{\langle D \rangle}$) and the Taylor trend ($\sqrt{\rho}$), which are both relevant to plasticity and

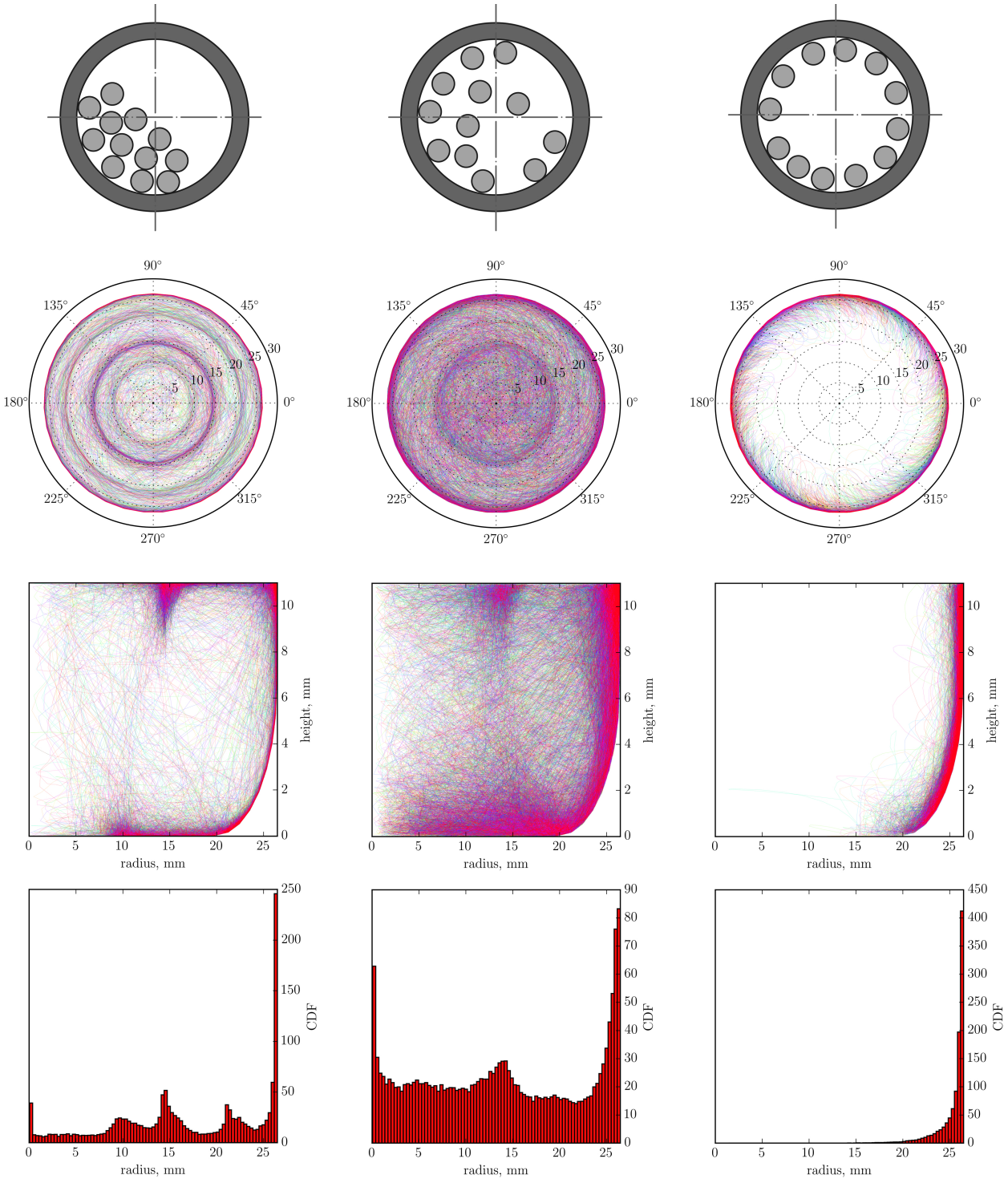

Figure 3.6: Top row, scheme of typical motion regime, from left to right (i) cascading, (ii) cataracting and (iii) rolling. Second and third row, trajectories (lines) within the jar ($\omega = -320, -600, -800$ rpm and $\Omega = 200$ rpm), polar coordinates (top) top view and (bottom) section. Bottom row, CDF (equation 3.9). Left to middle, the uniformity of the histograms increases (random motion); middle to right, balls tend to stick to the jar surfaces.

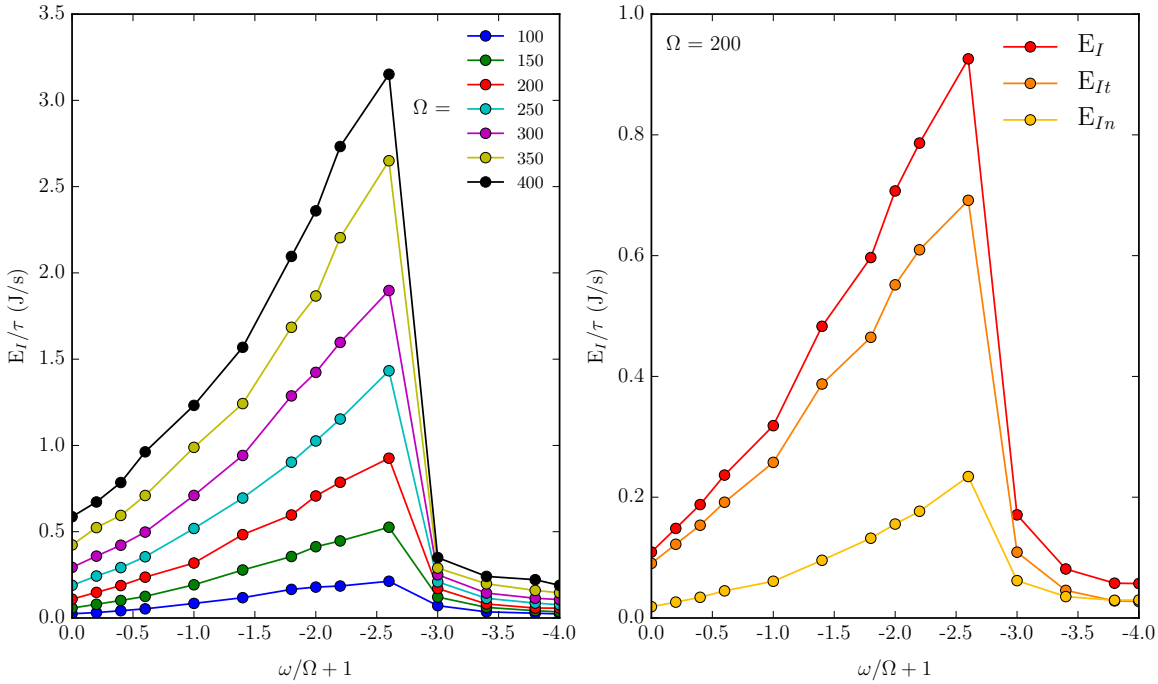

Figure 3.7: Specific impact energy for the steel-steel case as a function of the jar to plate angular velocities. Left, effect of incrementing the plate velocity Ω: while the specific energy increases, interestingly the location of its maximum is approximately not changing. Right, the specific energy of the curve with $\Omega = 200$ rpm is broken down into its normal (E_n) and tangential (E_t) components (with respect to the local impact reference frame).

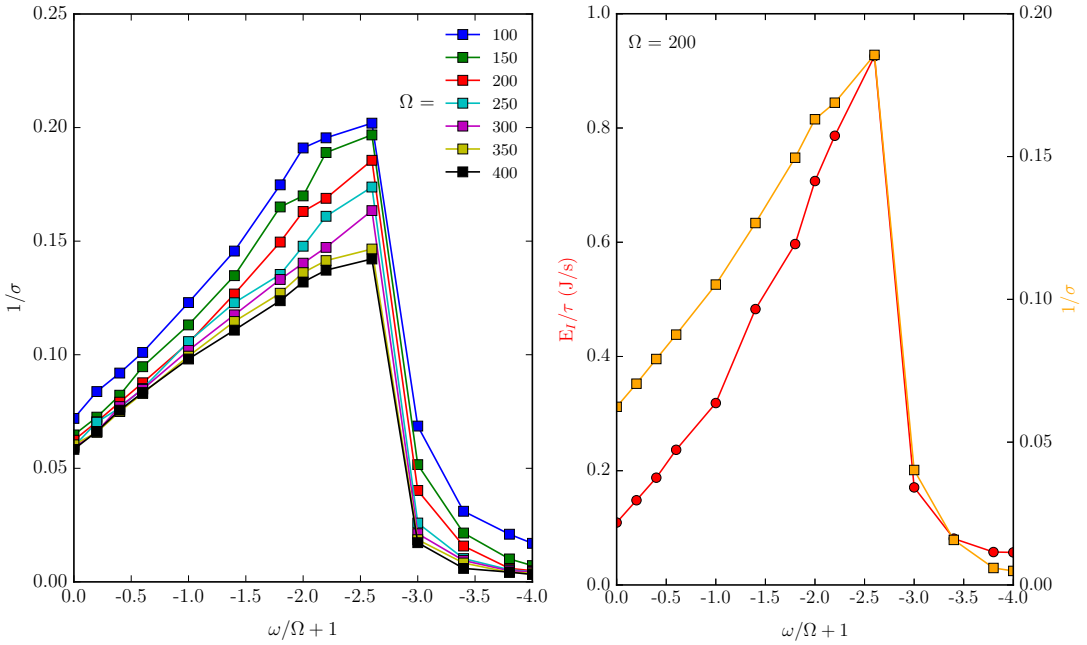

Figure 3.8: Left, geometrical parameter for the steel-steel case as a function of the jar to plate angular velocities Right, comparison of the geometrical parameter and the specific impact energy for the simulation with $\Omega = 200$ rpm: the behaviour is approximately the same.

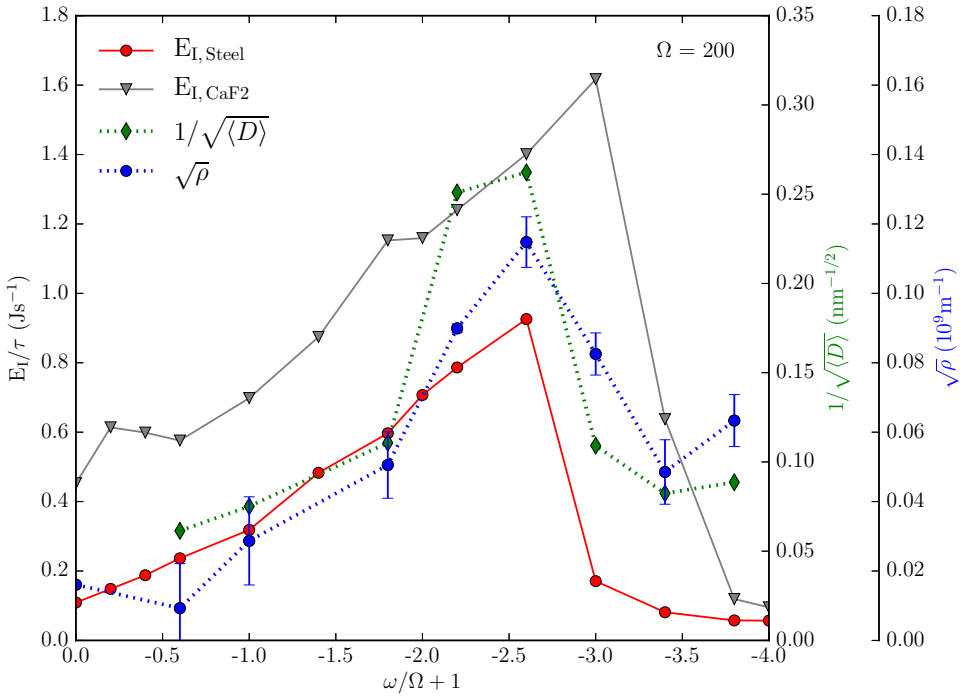

Figure 3.9: Specific impact energy for $\Omega = 200$ rpm and both steel-steel (red) and fluorite-fluorite (gray) interaction coefficients. LPA from XRPD data of ball milled calcium fluoride are also reported. Particularly, the reciprocal square root of the average crystallite size (green) and the square root of the dislocation density (blue), respectively proportional to the Hall-Petch and Taylor trends.

in general to the powder comminution features, are illustrated. Impact kinetic energy computed from simulations nicely maps the trend of the milling efficiency, thus providing a further validation of the proposed approach to simulate the milling process.

Conclusions and further developments

In this work a computer model for the P4 planetary ball mill has been presented and the effect of plate and jar velocity investigated. Two extreme conditions have been simulated, namely (i) steel-steel interaction (no mill charge) and (ii) steel-fluorite, by changing friction coefficients. Both cases have been analyzed from energetic and geometrical points of view. Results show that these, described by the specific kinetic impact energy and motion randomness parameters, are strictly related. In particular, the maximum value of the two parameters has been found to correspond to the same speed ratio, $\omega/\Omega + 1$ (cataracting motion regime), clearly indicating that the more the motion is complex the higher is the energy available for grinding. Moreover, for each set of contact coefficients, representing one the two milling conditions analyzed, results point out that the increment of plate angular velocity Ω, has an influence only on the amount of energy involved and not on the maximum location, suggesting that the geometry of the system dominates. The more efficient grinding condition was found to be at $\omega/\Omega + 1 \approx -2.6$ for the case of no steel-steel and at $\omega/\Omega + 1 \approx -3.0$ for steel-fluorite. The shift of the maximum is therefore due to the lowering of friction and indicates that, when fluorite is present, higher velocity ratios are required to achieve the most efficient grinding. Simulation output were also indirectly compared with experimental data from XRPD-LPA of ground fluorite. Particularly, average crystallite size and dislocation density have been characterized and related to mechanical properties through Hall-Petch law (yield stress) and Taylor equation (work hardening). In spite of the simplicity of the model used to simulate contacts, a good

agreement has been found within the two extreme conditions. The choice of a straightforward contact scheme is due to the not trivial calculation and tuning of model coefficients, which are the key ingredient for meaningful and reliable simulations: schemes depending on few parameters, easily estimable through simple experiments, support quick predictions of more efficient milling conditions for a given material, thus reducing and steering the experimental effort in fine-tuning the ball milling process.
As a further development, images of the milling process are going to be recorded through a high-speed camera directly mounted on the jar, therefore allowing more precise coefficients (and complicated contact models) to be retrieved *via* direct match of simulated and experimental trajectories. Guided by simulation outputs, molecular dynamics calculations are currently running aimed at understanding defect formation from an atomistic point of view. Finally, the power of simulations will be exploited to design more efficient jars.

Acknowledgements

The present work was partly supported by Fondazione Caritro, under project No 2013-0247 "Mechanical activation to improve bioavailability and reduce adverse effects of drugs in the therapy of chronic diseases" The authors are especially grateful to Dr. D. Catelani (MSC Software) for precious collaboration and support to the research work. N.M.P. is supported by the European Research Council (ERC StG Ideas 2011 BIHSNAM no.279985 on "Bio-inspired hierarchical supernanomaterials", ERC PoC 2013-1 REPLICA2 no. 619448 on "Large-area replication of biological anti-adhesive nanosurfaces", ERC PoC 2013-2 KNOTOUGH no. 632277 on "Super-tough knotted fibres"), by the European Commission under the Graphene Flagship (WP10 "Nanocomposites", no. 604391) and by the Provincia Autonoma di Trento ("Graphene nanocomposites", no. S116/2012-242637 and reg. delib. no.2266).

3.3 Remarks on impact energy calculations

In the previous section the expression 3.8 (E_I/τ)

$$\frac{E_I}{\tau} = \frac{1}{2\tau}\sum_{j=1}^{C}\frac{m_{1j}m_{2j}}{m_{1j}+m_{2j}}\,\dot{u}_j^2,$$

was used to estimate the maximum impact kinetic energy available within a second of simulation time (impact power). This quantity refers to the so-called *Stress Energy*, (SE) [18, 135]

$$SE = \frac{1}{2}\frac{m_{1j}m_{2j}}{m_{1j}+m_{2j}}\,\dot{u}_j^2, \tag{3.10}$$

defined as the maximum amount of energy that can be supplied to the mill charge in a single stress event.
Equation 3.8 and slightly modified definitions (*e.g.* normalised over the mass of the mill charge rather than over the simulation time), are reported by several works [18, 82, 117, 135, 136, 170]. In particular, in many of these, the summation in 3.8 runs over the total number of ball-ball and ball-jar collisions, so that the total amount of energy provided by the impacts occurring during the simulation time is effectively computed. However, the number of impacts can not be easily estimated if a continuous approach is used for modelling the collisions, as in the case of the software MSC.Adams as well as in many others DEM softwares – *e.g.* LIGGGHTS [137]. Within this approach indeed, the description of each collision is expressed by several calculation points, depending on the integrator settings. Since this can result in a huge amount of data, a sampling procedure is necessary to produce exhaustive but, at the same time, processable output files. As a consequence – for a process like the ball milling, involving a large number

of collisions – some events can be sampled by more than a single calculation point in the output file (oversampled collsions) whereas others can not be sampled at all. Therefore, in the previously reported paper [169], the summation in expression 3.8 did not run over the number of collisions but instead over the number of data points sampling the collisions, called C. The next sections however will show that the presented results are not affected by the sampling procedure.

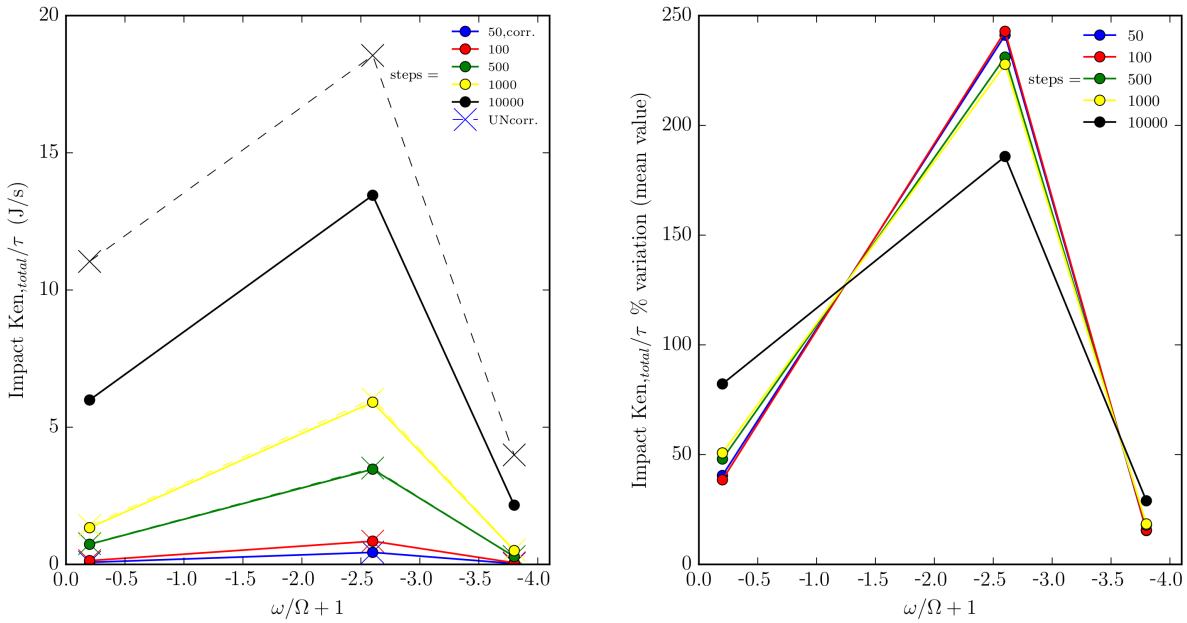

Figure 3.10: Left, trend of impact power (equation 3.8) for simulations performed at $\omega/\Omega + 1$ = -0.2, -2.6, -3.8, for different values of *step*. The impact power was computed running the summation in equation 3.8 over the total number of points sampling the collisions (crosses) and also over the estimated number of impacts (*i.e.* determined by discarding the sampling points after the first in oversampled collisions). For both cases and for all the values of *step*, curves approximately follow the same trend. Right, deviation (%) of each impact power point from the corresponding average value. All the *step* curves show approximately the same variation except from the *step*=10000 case, at which the variation reduces.

Integrator and sampling parameters

In MSC.Adams simulations, the sampling procedure is ruled by the user-defined *step* parameter, governing the output frequency, *i.e.* the total number of times over a well defined simulation period the simulator is required to provide an output information and to dump it to a file (*e.g.* , *step*=100 over 1 second simulation results in an dump time of 0.01 seconds). This variable is also closely connected to the integrator time step being the latter equal to 1/ *step* unless a different value of the variable h_{max} (defining the maximum time step the integrator is allowed to take) is specified (see section 2.2).
However, if contacts among modelled bodies are detected, the recipe presented above does not apply anymore. Indeed, to better handle the contact dynamics, the software automatically reduces the integration time step and, proportionally, increases the number of output points describing each impact. These feature can not be completely controlled by the user and depend on (i) the complexity of the event (*e.g.* for a multiple or a two bodies collisions different time steps are used) and (ii) the required output *step*, in order to avoid an excessive growth of the expected calculation time and output file size. Therefore, the

number of output points sampling each collision can not be known *a priori* and C varies as a function of the sampling procedure.

3.3.1 Analysis on the effect of the sampling procedure on impact power

Since in [91] C was used to compute equation 3.8 instead of the exact number of collisions, the assessment of the independence of the proposed result on the sampling procedure is necessary.
Simulations of the planetary ball milling, lasting 6 seconds, were performed for three velocity ratios ($\omega/\Omega+1$ = -0.2, -2.6, -3.8, *i.e.* corresponding respectively to the initial, the maximum and one of the last points of the impact power curve reported in figure 3.7), with fixed h_{max} = 1 E-6 and increasing value of the *step* variable (*step* = 50, 100, 500, 1000, 10000, where 100 was the value adopted in simulations presented in [91]).

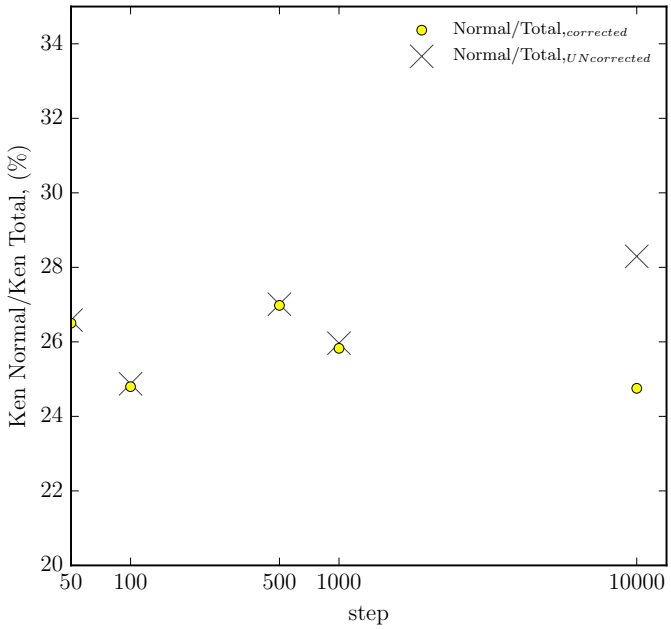

Figure 3.11: Fraction of normal-to-total impact power (in percentage), reported as a function of the *step* parameter. Maximum difference among reported data is around 2%, therefore indicating that the fraction of transferred energy in normal and tangential directions is not influenced by sampling procedure. Therefore, for all the values of the *step* parameter, the software provides the same description of the process dynamics.

For every simulation the impact power (equation 3.8) was computed and, the curves corresponding to each tested *step* value, are shown in figure 3.10a. It should be noticed that 2 series of data are reported (uncorrected– crosses– and corrected – circles), since, as will be better explained later, a procedure aimed at removing the oversampling was applied to the output data. However, for both the series, it can be seen that the variable *step* does not influence the trend of the impact power, since for all the curves, $\omega/\Omega+1$ = -2.6 corresponds to the maximum and $\omega/\Omega+1$ = -0.2 provides an amount of power smaller than -2.6 but larger than the $\omega/\Omega+1$ = -3.8 condition. This was further confirmed by computing, for every *i-th*

step set of simulations, the deviation from the average of each impact power value

$$\begin{aligned} \mathrm{E_{I,mean,step_i}} &= \frac{E_I|_{\omega/\Omega+1=-0.2,step_i} + E_I|_{\omega/\Omega+1=-2.6,step_i} + E_I|_{\omega/\Omega+1=-3.8,step_i}}{3} \\ variation\%|_{\omega/\Omega+1=-0.2,step_i} &= 100 \cdot \frac{E_I|_{\omega/\Omega+1=-0.2,step_i} - E_{I,mean,step_i}}{E_{I,mean,step_i}} \\ variation\%|_{\omega/\Omega+1=-2.6,step_i} &= 100 \cdot \frac{E_I|_{\omega/\Omega+1=-2.6,step_i} - E_{I,mean,step_i}}{E_{I,mean,step_i}} \\ &\dots \end{aligned} \tag{3.11}$$

No substantial differences among the trend of the resulting curves (and, in turn, in the impact power trend) are highlighted in figure 3.10b. The only exception can be noted for *step* = 10000, a condition exhibiting a less steeped curve, indicating a reduced difference among the impact power provided by the three $\omega/\Omega + 1$ tested conditions.
Also the ratio between normal and total impact power, reported in figure 3.11, does not evidence a strong dependence on *step* (the maximum variation is approximately of the order of 2 %). The consistency of the proportion between the fraction of energy provided in normal and tangential direction suggests that the milling process dynamics is well and equally described independently form the configuration of the sampling procedure.

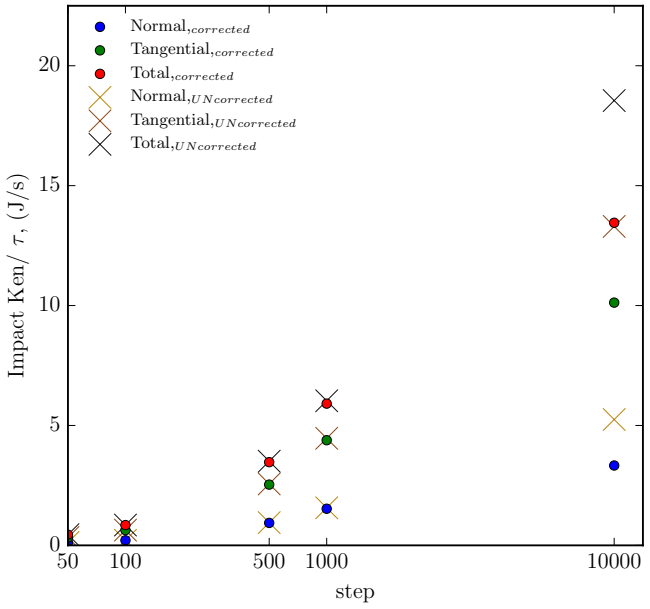

Figure 3.12: Impact power computed before (crosses) and after (points) the procedure for removing extra-points. It can be seen that the correction significantly affects only the *step* = 10000 case.

These results confirm that speculations reported in [91] about the effect of the different milling conditions on the grinding performance are reliable independently from the sampling procedure.
However, on the contrary, figure 3.10a highlights that the magnitude of the impact power is a function of the *step* parameter. Since in the calculation of equation 3.8, it would be correct to consider only a single point for each collision, an investigation on the effect of the oversampling on the computed impact energy is proposed.

In a system like the planetary ball mill, characterised by a large amount of (mainly multiple) collisions simultaneously occurring, separating each pair-contact – therefore determining the exact number of collisions – is not an easy task. To roughly estimate if more than one data point is sampling the same event (extra points) the average duration of a two-body impact was used as a criterion to filter the output data. Indeed, if subsequent data points are closer in time than this quantity, they should be part of the same collision event.
Simulations of two spheres impacting at different angle and velocity ($v_{rel,i}$ = 10, 100, 1000, 2000 mm/s), performed for fixed h_{max} = 1 E-6 and increasing *step*, provided the estimate of the average maximum duration of a collision, Δ_{max} = 3.7 E-4. Besides this quantity, also the number of output points given by each simulation was registered and it is reported in 3.4 for the case of v_{rel} = 100 mm/s. It can be seen that, as expected, output points increase with *step* and particularly, for *step* less than 1000 only a single point, corresponding to the beginning of the collision event, is provided. According to this observation, being simulations presented in [91] performed with *step* = 100, a reduced number of extra points can be reasonably expected.

step	output points	impact duration (Δ)	
10	1	-	inital point
50	1	-	inital point
100	1	-	inital point
500	1	-	inital point
1000	1	-	inital point
10000	4	8E-5	-
100000	38	9E-5	-
200000	61	9E-5	-

Table 3.4: Results of the simulations of a central impact between two spheres with relative initial velocity equal to 100 mm/s. Simulations were performed with h_{max} = 1 E-6 and increasing parameter *step* so to investigate the influence of the sampling procedure on the number of output points per collision. For each value of *step*, the table reports the duration of the contact event (if more than an output point was given) and the number of output points. If a single calculation point is given, also its position along the curve describing the evolution of the contact event, is provided.

step	$Oversampled Collisions$
50	2
100	8
500	146
1000	482
10000	29900

Table 3.5: Estimated number of oversampled collisions for simulations corresponding to every *step* investigated.

However, to deeply investigate the effect of oversampling in planetary ball milling modelling results and its dependence on the *step* variable, the above-mentioned simulations performed with different number of *step* and $\omega/\Omega + 1$ = -2.6 were exploited. An algorithm (i) computing the difference in time between each output point and the prior one and (ii) evaluating if the difference is less than Δ_{max}, was developed to estimate the number of collisions sampled by more than one calculation point. Results are reported in

table 3.5 and it can be seen that only for values of *step* greater then 1000 the oversampling is remarkable. Anyway, all the calculation points after the first were removed from oversampled collisions, so to take into account only the velocity at the beginning of each contact event in the calculation of equation 3.8, as required by the definition of kinetic energy [87].
It should be noted that, assuming the proposed criterion to be sufficiently reliable, after this procedure the parameter C should be approximately equal to the total number of detected impacts.
Figure 3.12 reports, as a function of *step*, the impact power computed after and before the removal of extra points and it can be seen that, for both cases, this quantity does not converge to a common value but, on the contrary, steadily grows with the parameter *step*. Therefore, a value suppling not over/undersampled data can not be deduced and, it can be stated that, in terms of magnitude, the impact power strictly depends on the sampling procedure and, as highlighted in [169], its absolute value results arbitrary and not directly comparable with power available in a real apparatus.

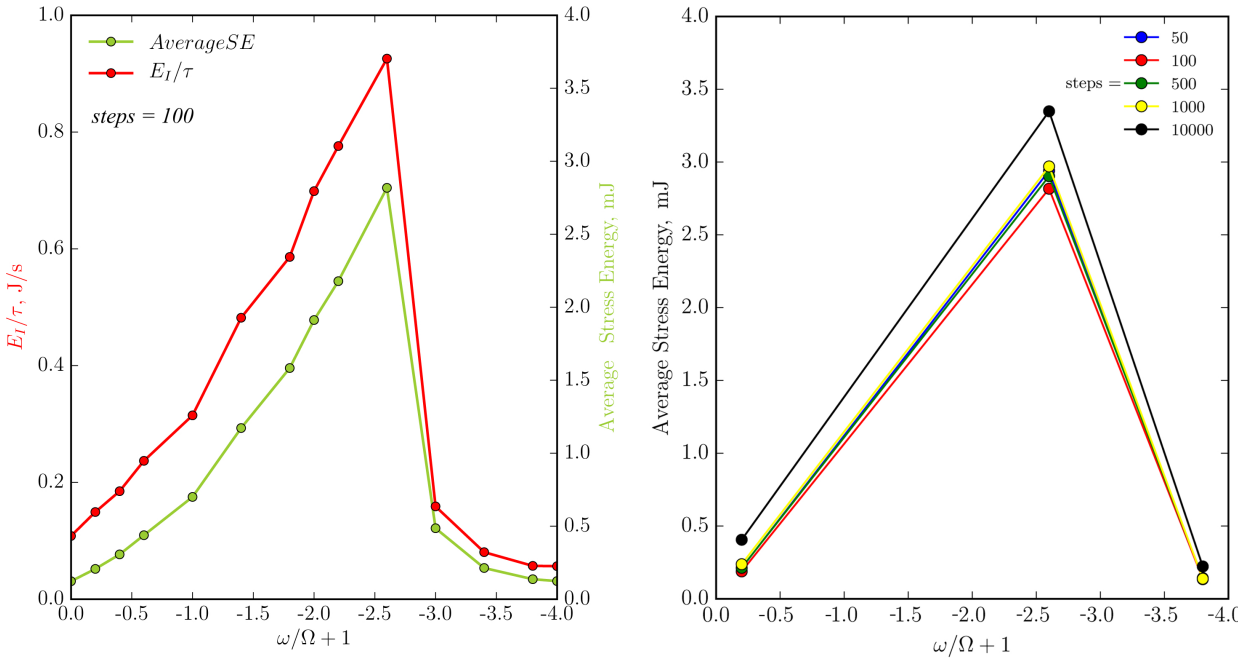

Figure 3.13: Left, comparison of E_I/τ and average SE computed from simulations performed with *step* = 100, for different jar-to-plate velocity ratios. Interestingly, the two quantities share the same trend and therefore are both reliable for speculations about the overall performance of the grinding process. Right, comparison of SE calculated from simulations performed varying the *step* variable. The almost complete overlap of the resulting curves indicates that the magnitude of this quantity is not dependent on the sampling procedure.

However, as already introduced, the amount of energy effectively involved in grinding relates not only to the impacts but also on other several phenomena (*e.g.* heat transfer) hardly considerable in a multibody numerical model. Therefore, the goal of this kind of simulations should not be the exact computation of the amount of the available impact power but rather the description and the comparison of the effect of different milling conditions, which can be deduced from the trend of a representative parameter, *e.g.* the impact energy, computed for a common sampling procedure.
Anyway, in the next chapters, 3.8 is replaced by the weighted average of the probability distribution of the Stress Energy (equation 3.10), calculated (after the removal procedure here proposed) for every detected contact event. This quantity is much more immediately understandable than E_I/τ, representing the average kinetic energy supplied by a single event. Moreover, it exhibits the same trend of E_I/τ, as illustrated in figure 3.13 left for the 100 step case, and, interestingly, in terms of magnitude, is much less

influenced by the sampling procedure. Indeed, as a difference with the E_I/τ (see figure 3.10 left), figure 3.13 right, shows the average SE curves, obtained from simulations performed with a different number of *steps*, to almost completely overlap, thus highlighting that the magnitude of this quantity does not vary as a function of the sampling variables.

3.3.2 Analysis on the effect of simulation time on impact power

Data reported in [91] refer to simulations of the ball milling lasting 24 seconds, an amount of time reasonable both in terms of statistics and amount of data to be processed.
In order to investigate the connection between the output of equation 3.8 and simulation time, τ, a 60 seconds simulation of the process was performed ($\omega/\Omega + 1$ = -2.2, *step* = 100) and divided into several time intervals (*time range*, in figure 3.14). Equation 3.8 was computed for each interval, assuming C equal to the number of points sampling the collision within the considered *time range* and τ = *time range*. Figure 3.14, shows that the resulting total power and its components are stationary and therefore not dependent on simulation time. This suggests also that (i) the motion regime, corresponding to the investigated velocity ratio, develops already at the very beginning of the simulation and remains the same for its entire duration; (ii) for all the simulation time, contacts are resolved in the same way in terms of output and integration step; (iii) the amount of data provided by 24 seconds of simulation are statistically sufficient to describe the motion dynamics.

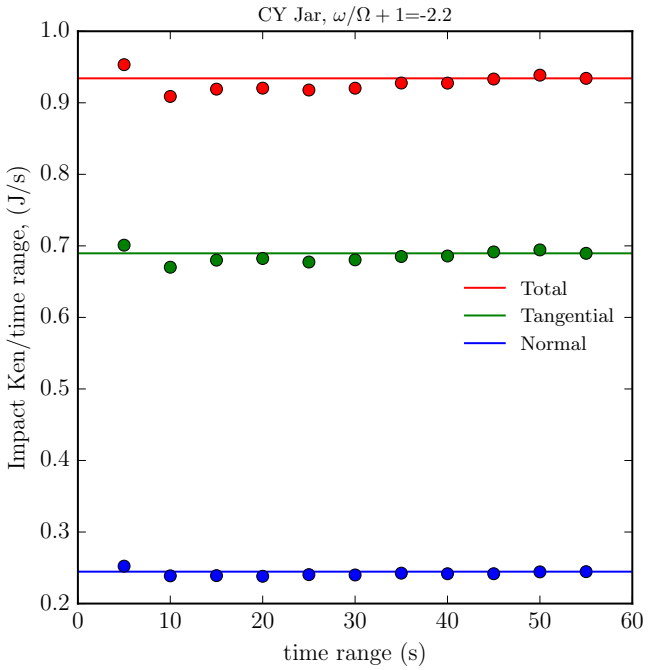

Figure 3.14: Impact power computed for the different time intervals in which a 60 seconds planetary ball milling simulation was divided. The time-stability of this quantity highlights that it doesn't depend on simulation time.

Chapter 4

The effect of jar shape on process efficiency: simulations and experiments

Chapter 3, presenting a multibody-dynamics model for the planetary ball milling process pointed out that different balls motion regimes, discernible in terms of disorder (*e.g.* balls sliding or swirly crossing the grinding chamber), can establish depending on the setup of the milling variables. In particular, it was shown that the higher the motion complexity (*i.e.* the larger the mean free path of balls) the greater the energy involved in impacts and the size reduction of the mill charge.
Therefore, it can be deduced that collisions direction and intensity and, consequently, the characteristics of the end product, are determined by ball movement inside the jar which, in turn, depends on the mill configuration.
While literature proposes several works analysing the influence of parameters such as the number and dimension of balls [171–173], the angular velocities of revolving parts [18, 82, 117, 171], the balls filling ratio [117] and friction [18], much less attention has been given to the shape of the jar, generally assumed to be cylindrical. The following sections deal instead with the re-design of its internal profile, considered an alternative and advantageous way to perturb the milling media dynamics so to enhance process efficiency.
4 innovative designs (see figure 4.1) are proposed [‡], breaking the cylindrical symmetry of the standard jar in different way but pursuing the same goal of disordering ball movement. Particularly, obstacles or polygonal profiles were devised so to drive balls along *ad hoc* designed trajectories, especially promoting impacts with high axial velocity component, deemed as the most effective in the comminution process of brittle materials (such as fluorite, used here as testing material). Indeed, generally speaking, while shear actions could produce plastic deformation, compressive forces exchanged in normal direction with respect to the impact reference frame should promote size reduction of particles [1, 15, 174].
Investigations on the newly designed jars are carried out through different approaches. In particular, the previously presented multibody dynamics model of the process is exploited and, consistently with the prior example, results validation is accomplished by XRPD-LPA of ground CaF_2. Moreover, model validation is here further enforced by *in operando* video recordings, giving a quick insight on the real grinding process. For the experimental testing, newly designed jars prototypes were produced at the mechanical laboratory of the University of Trento.

The present chapter is divided into two sections and, while the first reports an overview of the results for all the proposed new designs of the jar, the second focuses on the so-called Half-Moon one.

[‡]Designs were conceived by M. D'Incau and introduced in [138]

4.1 Four new designs for the jar of the planetary ball mill [†]

As already introduced, an alternative approach to modify and possibly improve the milling process could be re-designing the internal shape of the jar. Figure 4.1 proposes 4 jar shapes that, in different way, could in principle enhance the amount of impacts with high-normal-relative-velocity component and therefore improve the comminution of the mill charge. Particularly, the 1-Lifter jar (1L) and the 3Lifters (3L) designs (figure 4.1, center) were inspired by the tumbling ball mills (presenting a cylindrical lined shell) and introduce respectively 1 and 3 obstacles (lifters) along the jar wall, shooting balls in different directions, depending on impact angles and the velocities, therefore strongly disordering ball movement. The number of the lifters was properly planned: in fact, a large number of lifters enhances the balls motion complexity and the amount of collisions but, at the same time, reduces the internal volume of the jar and, in turn, the maximum flight length and the velocity of balls. Also lifters shape and dimension deserved specific attention and in particular, rounded profiles were preferred over sharp edges so to prevent the formation of regions barely accessible by milling media where powder could accumulate (and therefore would not be ground).
The Half-Moon (HM) shape (figure 4.1, left) was inspired by the theoretical analysis on the ideal trajectory of a single ball in a standard cylindrical jar (CY), proposed in literature [111]. Theory suggests that a ball should move as an integral whole with a point on the vial circumference until, by a given composition of the inertial forces, it is launched against the opposite point, perpendicularly to the jar surface. This results in a high velocity impact, transferring a large amount of energy especially along the axial direction. However, in a real scenario, due to the interactions with many balls and the mill charge, this ideal trajectory hardly takes place. Therefore, the HM design, introducing a flat surface halfway between the curved wall and the axis of a CY jar, was conceived so to drive the balls along the above-described *ideal path*. Finally, the Triangular jar (T) (figure 4.1, right) can be considered an amplification of the HM concept as it presents 3 flat surfaces therefore resulting in a polygonal shape.

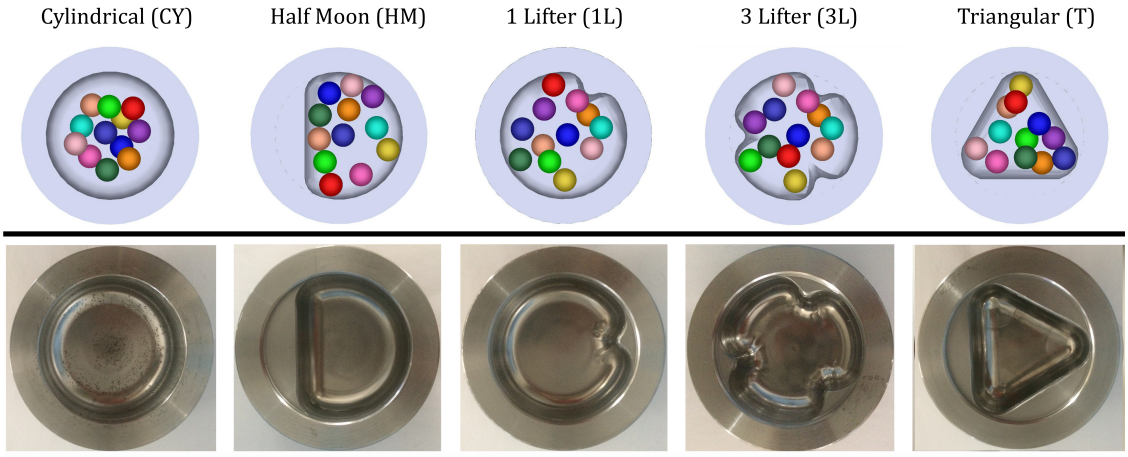

Figure 4.1: New designs for the internal shape of the jar of the planetary ball mill. Top, parasolid models for the multibody dynamic simulations. Bottom, prototypes of stainless steel jars.

[†]For the results reported in this section, my main contributions were developing the multibody-dynamics models, performing the simulations and analysing the output data, executing the *in operando* camera recordings and part of the milling experimental tests. In collaboration with L. Gelisio, I also designed and builded the apparatus for camera recordings. M. D'Incau conceived the jars designs, performed part of the experimental tests and collected the XRPD data. P. Scardi modelled the XRPD patterns. Images reporting XRPD data are courtesy of M. D'Incau and P. Scardi.

4.1.1 Methods

Newly designed jars were investigated through experiments performed with the planetary ball mill Fritsch Pulverisette 4 (P4, [109]) and numerical simulations. Jar-to-plate velocity ratio, expressed as $\omega/\Omega + 1$, was varied between 0.0 and -4.0 (with fixed Ω and increasing ω) for each set of analyses.
12 carbon steel (AISI C1020) balls were placed inside the stainless steel jars (AISI 304), characterised by the internal volumes reported in table 4.1. All the other geometrical and physical properties of the milling process are listed in table 4.2.
Experimental tests were performed on CaF_2, grinding 2.1 g of powder under different velocity ratios. For CY and HM jars, samples were ground also for different milling time (1h, 4h, 8h, 16h, 32h and 64h) so to investigate the effect of this variable.

Jars Internal Volume)	
Cylindrical (CY)	72ml
Half Moon (HM)	60ml
1 Lifter (1L)	71ml
3 Lifters (3L)	69ml
Triangular (T)	51ml

Table 4.1: Internal volume of the newly designed jars.

Camera recordings - Experimental set-up

Balls motion inside the jars was monitored *in operando* by means of a high speed camera (Sony Action Cam HDR-AS200V, 240 fps, 1280X720 pixel resolution). Since the camera was directly installed on the jar through an expressly designed slot (see figure 4.2), the recorded balls trajectories refer to the vial reference frame. The visibility of milling media was allowed by a transparent polycarbonate lid and 50 LEDs mounted on a ring (*i.e.* an automotive angel eye). A first group of recordings was taken without the mill feed and then calcium fluoride was added for a new batch of observations. This way, the effect of the mill charge was clearly highlighted. Both qualitative and quantitative information could, in principle, be extracted from the camera recordings [175]. So far, only a qualitative analysis of ball movement and its dependence on the jar shape and the velocity ratio is proposed but the determination of the trajectory and velocity of the single balls is in progress.

Computer Simulations

The newly designed jars were tested through the multibody dynamics model described in detail in chapter 3. Since the same milling media and mill charge of the former example were adopted, parameters ruling contacts as well as friction coefficients for the (i) steel-steel (no mill charge) and the (ii) steel-fluorite interactions (*i.e.* jar or balls surface completely covered by fluorite) are reported in table 3.2 and 3.3.
It should be noticed that, beside providing more reliable suggestions about the milling process, the simulation of these two extreme conditions allowed a direct comparison between simulated movies and camera recordings for the steel-steel case and further speculations on the effect of the powder. In addition to the quantities characterising the motion of each body, also deducible from camera recordings, modelling granted access to the description of contact events and, in particular, in the following sections the relative velocities of colliding bodies decomposed into normal (axial) and tangential components with respect to the local impact reference frame are exploited, so to estimate the available average kinetic energy.

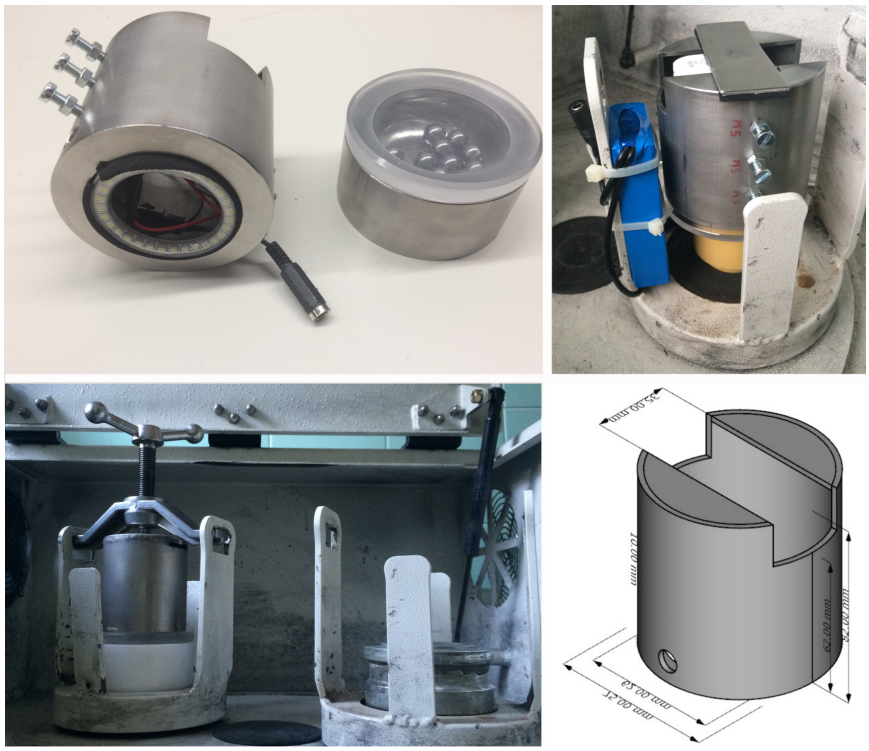

Figure 4.2: Top left, slot used for mounting the high speed camera directly on the jar equipped with a transparent lid; top right and bottom left, the slot mounted in the P4 planetary ball mill; bottom right, 3d model of the slot.

XRPD-LPA

The effect of grinding the calcium fluoride powder was assessed by XRPD-LPA [157, 158]). Data collection was performed on a Rigaku PMG/VH diffractometer, using CuKα radiation monochromatized by a pyrolytic graphite curved crystal in the diffracted beam. LPA was based on the WPPM approach, briefly introduced in section 3.2 (more details can be found in *e.g.* [140–142]). As well as in the previous work, the analysis provided the average size ($\langle D \rangle$) of the crystalline domains – assumed to be spherical and dispersed according to a lognormal distribution – and the average dislocation density (ρ), considering the primary slip system and the elastic constants of fluorite. Particularly, the more efficient the process, the more $\langle D \rangle$ is expected to decrease (higher comminution) whereas ρ, is supposed to grow [93, 159–164].
As will be better explained in section 4.2, the analysis was based on the presence of one or two fractions of fluorite, depending on the efficiency of the specific grinding vial and milling conditions. In particular, a single fluorite phase was considered when the end product was a homogeneous fine powder whereas an additional phase was introduced to model a coarse (little or not ground) powder fraction, present in varied percentages together with the fine fraction when the grinding process was not efficient or not sufficiently long. Differently from the previous work, where the PM2K [176] computer program was used, in this case the WPPM model was included as a macro within the software TOPAS (version 6, [177]), a powerful tool for Rietveld refinement implementing the structural model of the present phases, acting as a constraint adding robustness and reliability to the analysis. In particular, besides the number of fractions of fluorite (respectively fine and coarse), the analysis also considered a minor fraction of MgO (contaminant phase in the starting powder, around 0.5%), and the amount of steel contamination, modelled as ferritic iron.

4.1.2 Effect of jar shape on balls motion, average impact kinetic energy and comminution

In a planetary ball mill, equipped with a standard cylindrical jar, generally 3 different balls motion regimes (cascading, cataracting, rolling) tend to arise, as a function of the jar-to-plate velocity ratio [18, 82, 115, 175]. Particularly, for the mill configuration proposed in section 3.2 (and in [91]), for the steel-steel interaction (no mill feed) the multibody dynamics simulations of the milling process showed that, for the lower $\omega/\Omega + 1$, balls move along the jar wall as a compact group into cascading motion. Then, at increasing jar velocity, they detach from the group and collide against other balls or the jar wall, gradually enhancing the motion disorder, till $\omega/\Omega + 1$ = - 2.6, where the maximum complexity (cataracting regime) is reached. Above this threshold, a sharp change occurs as balls stick to jar surface (rolling mode). Owing to the larger number of high-velocity impacts, the cataracting mode was demonstrated to be the most effective in transferring energy to the mill charge [91] and, therefore, jars here presented (HM, 1L, 3L, T, figure 4.1) were designed in order to promote this kind of motion. *In operando* monitoring of the process, both with simulations and camera recordings, revealed that balls hitting the new profiles disorder the motion already from the lower $\omega/\Omega + 1$. The beginning of the cataracting regime can be fixed at approximately $\omega/\Omega + 1$ = -1.8 and it extends till about -2.2, namely over a wider range than in the CY jar therefore suggesting newly designed jars to be less sensitive to the milling parameters that differ from jar shape.
A quick insight on motion modes detected for the CY and the 3L jars is reported in figure 4.3. The nice agreement among camera recordings and simulations images should be noticed, both in terms of motion regimes and their variation with $\omega/\Omega + 1$, thus providing a further validation of the modelling results.
Beside the influence of the velocity ratio, both simulations and video recordings performed with different Ω (but under the same $\omega/\Omega + 1$ velocity ratios) showed this variable to affect the position of balls along the vertical dimension (height) of the jar. Indeed, as illustrated in figure 4.4, regardless of jar shape, at increasing Ω balls tend to dispose in multiple superimposed layers along the jar height whereas at lower values (*e.g.* Ω = 50rpm) their motion is mainly confined to the bottom region of the vial.
Moreover, for low Ω, the above-mentioned typical 3 motion regimes are clearly identifiable in camera images and for this reason both simulated and recorded images reported in figure 4.3 refer to Ω = 50rpm. For higher Ω instead, the cascading and cataracting regimes become hardly distinguishable in camera recordings. This probably relates to the increased amplitude of vibrations produced by engine operations and, above all, to the contacts occurring between the highest layer of balls and the jar lid, made of polycarbonate. In fact, the reduced stiffness and the increased damping, diminishing the impact kinetic energy, as well as the lowered friction, tend to hinder the balls to fall down to the bottom of the vial, consequently altering their motion.
On the contrary, for all the Ω the transition to the rolling regime is clearly visible and approximately corresponds to the same $\omega/\Omega + 1$. Therefore, as already discussed in [91], it can be supposed that this variable doesn't significantly affect the motion regime which, all else being equal, mostly seems to depend on the jar-to-plate velocity ratio. Moreover, in [91, 92] an increase of the amount of available impact energy with Ω was suggested and it was confirmed by experimental milling of calcium fluoride (as reported in [138]) showing Ω = 200rpm to give the best results in terms of comminution.
Simulations performed adopting the latter Ω provided with the relative velocities of colliding bodies, $\dot{u}$, which were also decomposed into the normal ($\dot{u}_n$) and tangential ($\dot{u}_t$) components with respect to the impact reference frame. These quantities were exploited to compute, for each k-th impact, the Stress Energy (SE), defined as the maximum kinetic energy that can be supplied to the mill charge in a single collision event (see section 3.3 and [12, 18, 117, 135]),

$$SE_k = \frac{1}{2}\frac{m_i m_j}{m_i + m_j}\dot{u}^2,$$

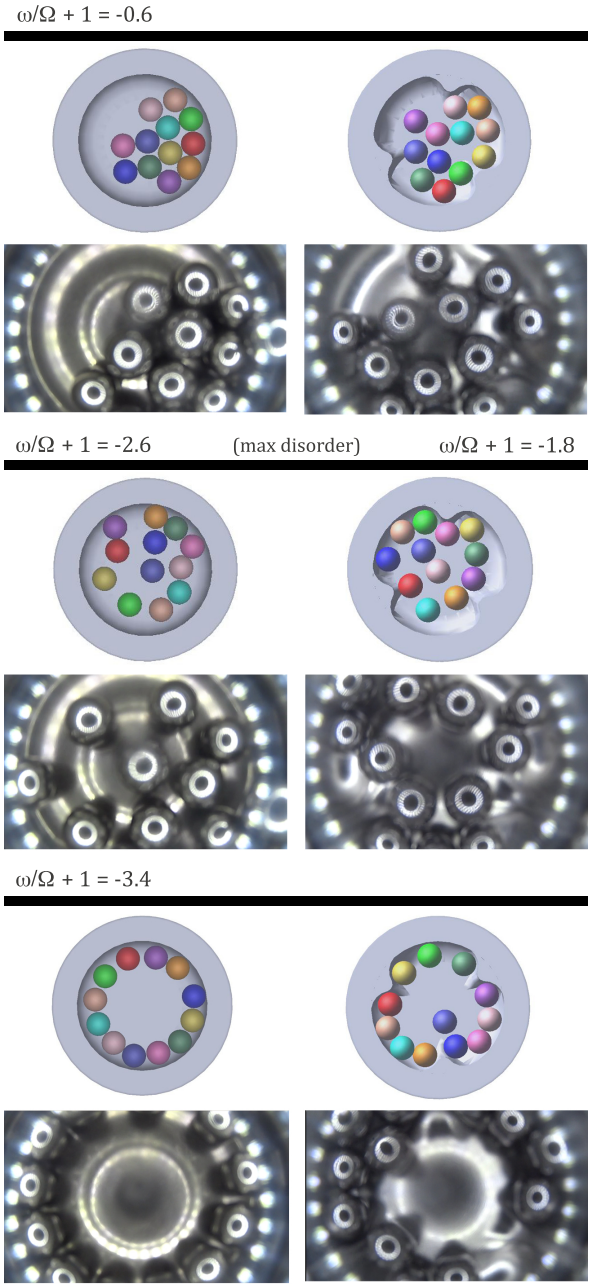

Figure 4.3: Comparison of ball movements in the CY and 3L jars from simulations and camera recordings for three $\omega/\Omega + 1$ values ($\Omega = 50$rpm), highlighting the development of three different motion regimes. A good agreement between simulated and recorder images can be appreciated.

being m_i , m_j the masses of the i-th and j-th impacting bodies (for ball-jar contacts $m_{jar} = \infty$ as $m_{jar} \gg m_{ball}$). Since simulations provide a continuous description of impacts, data were filtered in order to take into account only the velocities at the beginning of each contact event. As better explained in section 3.3, this was accomplished by estimating a reasonable maximum duration of a two-body collision from simulations of two spheres impacting at different angle and velocity, and discarding from calculations data closer than this minimum time period.
For each tested $\omega/\Omega + 1$ the weighted average of the probability distributions of the SE was computed,

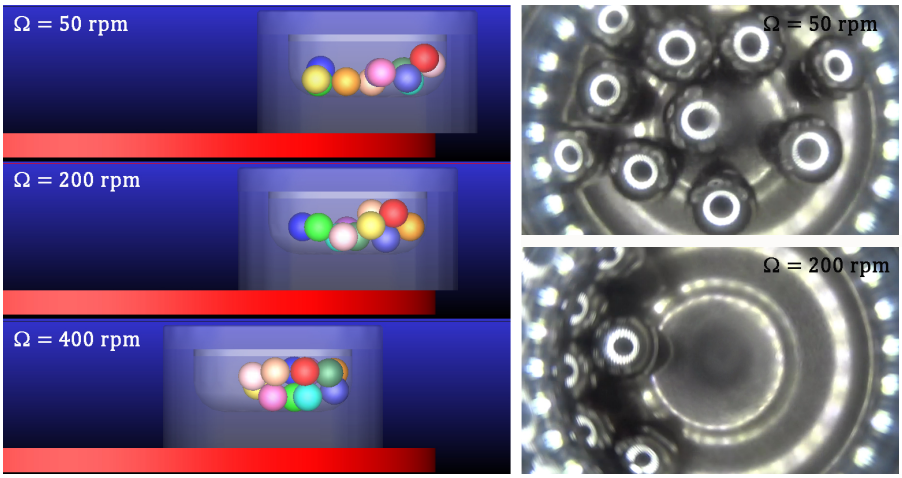

Figure 4.4: Influence of plate velocity on position of balls inside the jar during milling, showed both by simulations (left, Ω = 50, 200, 400rpm and $\omega/\Omega + 1$ = -2.6) and camera recordings (right, Ω = 50 and 200rpm and $\omega/\Omega + 1$ = -2.6). With the increase of Ω, milling media tend to assemble in superimposed layers along jar height.

both for the normal and the tangential components of relative velocity, and normalised over the internal volume (V) of the jars (see table 4.1) in order to account for the different limitation in ball movement and velocity. This quantity, estimating the average stress energy density involved in an impact, is reported in figure 4.5, both for the steel-steel (upper part) and the steel-fluorite (lower part) interactions, since real grinding is expected to fall in-between these two boundary conditions. For the steel-steel case, both the normal and the tangential impact average energy components present a maximum peaked at $\omega/\Omega + 1$ = -2.6 for the CY and a range of almost comparable maximum values extended from approximately $\omega/\Omega + 1$ = -1.8 to -2.2 for the other jars. These ranges of velocity ratios, optimal in terms of stress energy density, nicely agree with the conditions of the most disordered balls motion revealed by camera recordings, thus further supporting the close relation between balls motion and available energy, pointed out in section 3.2. Moreover, section 3.2 showed that for the CY jar the reduction of friction due to the presence of fluorite promotes an increase of the average impact energy, especially in the tangential direction, and a shift to more negative $\omega/\Omega + 1$ of the maximum value. However, these effects are much less evident for the newly designed jars, suggesting that the process is more affected by jar shape than by the other milling variables, including the characteristics of the mill charge.
What is even more important to notice is that the average stress energy density in normal direction (figure 4.5, left) is larger for the newly designed jars than for the CY, starting from the very first $\omega/\Omega + 1$ and till approximately $\omega/\Omega + 1 = -2.6$, where the rolling begins. This relates to the greater complexity of motion modes establishing in the newly designed jars, particularly increasing the number of impacts with high normal relative velocity component with respect to the CY one, as highlighted in the left part of figure 4.6. On the contrary, the right part of the same figure, reporting the probability distribution of impact relative velocities in tangential direction, shows that larger values are overall provided by the CY. However, this velocity component mainly relates to the slip among colliding bodies and the corresponding stress energy (see figure 4.5, right) was shown to promote especially processes like exfoliation and/or incorporation of defects [1, 15, 16, 174, 178]. The normal component of exchanged energy is instead generally supposed to be more effective for the comminution of brittle materials [1, 15, 174] and therefore the new jars, providing with a larger fraction of significative events along this direction, are expected to give better results in terms of end product size reduction than the CY. Validation of this prediction was addressed by WPPM analysis of experimental XRPD patterns collected on fluorite samples ground for 32 hours under different velocity ratios, suppling the average crystallite dimensions ($\langle D \rangle$) of the end products.

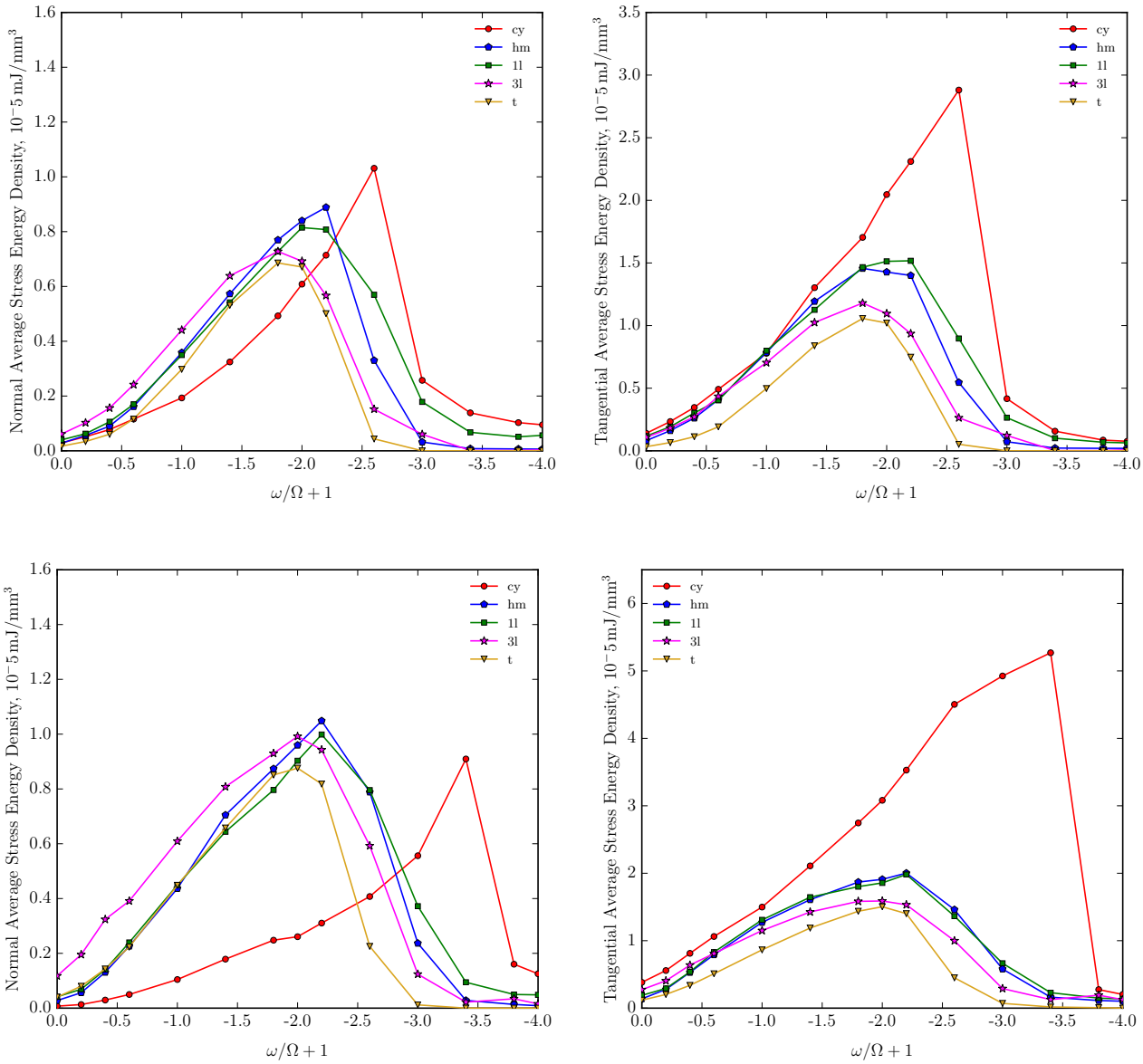

Figure 4.5: Average stress energy density of impacts in normal (left) and tangential direction (right) as a function of $\omega/\Omega + 1$. These quantities are shown for the the steel-steel and for the steel-fluorite interactions, respectively, in the upper and in the lower part of the picture.

As anticipated in subsection 4.1.1, in case of barely efficient grinding conditions, the resulting powder is not homogeneous, showing the coexistence of a ground (fine) and a less-to-not ground (coarse) fractions, requiring a bimodal distribution of sizes to properly modelling the XRPD data. For every tested condition, XRPD-LPA provided with an estimate of the percentage of the two fractions, the ratio of which is reported in figure 4.7. Interestingly, almost in line with simulations results, best grinding performance – *i.e.* providing with a homogeneous and finely ground end product, modelled by a single distribution (ratio in figure 4.7 equal to 1) – range from approximately $\omega/\Omega + 1$ = -1.8 to -3.0 for the CY, whereas correspond to lower velocity ratios (from about -0.6 to -2.2) for the other jars. It is worth noting that, the 1L seems to behave differently from the other newly designed jars since a larger fraction of coarser

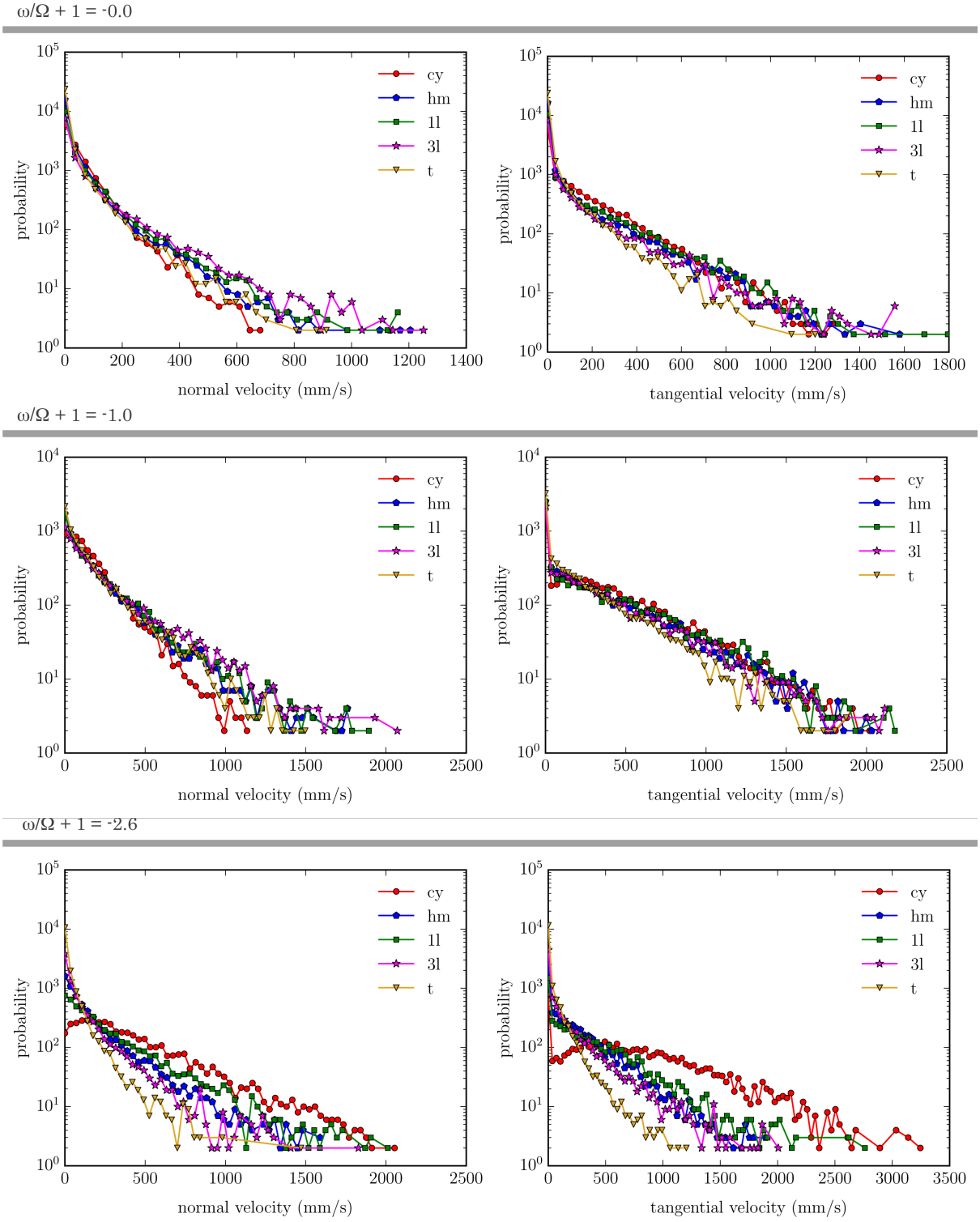

Figure 4.6: Probability distributions of normal (left) and tangential (right) components of the relative velocities of colliding bodies. In normal direction, especially at high velocity, the new jars exhibits a larger number of impacts than the CY till $\omega/\Omega + 1 =$ -1.8 ($\Omega = 200$rpm). In tangential direction instead the CY jar, more or less markedly, exceeds the others.

powder can be detected for the lower velocity ratios (from $\omega/\Omega+1$ = -0.6 to -1.4). However, LPA revealed that this fraction can not be actually considered as coarse, exhibiting smaller $\langle D \rangle$ (nanometer range) with respect to the coarse fraction produced by the CY. It can therefore be stated that, although a slightly reduced homogeneity of the end product with respect to the other newly designed jars, at low velocity ratios also the 1L performs well and, above all, better than the CY in terms of comminution of the mill charge.

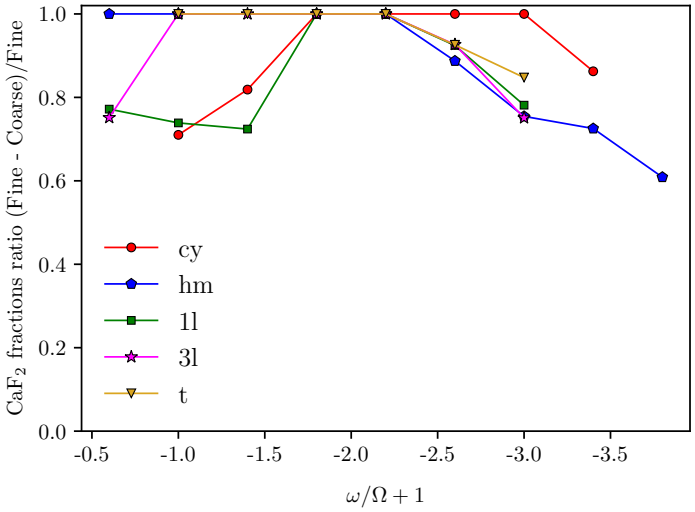

Figure 4.7: Ratio of fine and coarse fractions of calcium fluoride ground for 32h, under different velocity ratios and Ω=200rpm. The presence of the coarse fraction implies not efficient grinding, while a uniform and finely ground end product indicates that proper milling conditions were adopted. Best milling conditions range approximately from $\omega/\Omega + 1$ = -1.8 to -3.0 for the CY and from about $\omega/\Omega + 1$ =-0.6 to -2.2 for the others jar.

4.1.3 Effect of jar shape on milling time

Above reported experimental data were inferred from samples ground in all the jars for 32h, a milling time that previous studies (see [138]) demonstrated to be optimal for the CY to produce a sufficiently homogeneous end product. However, this amount of time could be an upper bound for the newly designed jars, showing higher efficiency in comminution than the CY.
To validate this hypothesis, the CY and the HM jars (the latter chosen as representative of all the newly designed jars) were experimentally tested under six different milling times (1h, 4h, 8h, 16h, 32h and 64h). Experiments with fluorite were performed for two velocity ratios, namely $\omega/\Omega + 1$ = -1.0 and $\omega/\Omega + 1$ = -2.6, the former being within the range of ideal milling conditions for the HM and the latter favourable to the CY. XRPD-LPA results are reported in figure 4.8 in terms of (a) mean domain size, $\langle D \rangle$, (b) percentage of fine fluorite fraction, (c) iron contamination percentage and (d) average dislocation density, ρ.
The a, b left part of figure 4.8 ($\omega/\Omega + 1$ = -1.0) demonstrates that for milling time shorter than or equal to 32 hours, the CY jar gives a non-homogeneous end product, with a relevant coarse fraction of several hundred nanometres of mean domain size. On the contrary, with the HM jar, a single fluorite phase, uniformly and finely ground, is obtained even after short milling time (*e.g.* 1 hour).
At $\omega/\Omega + 1$ = -2.6 (figure 4.8, right a and b) the rolling regime establishes in the HM jar and this reflects in an end product with a fraction of coarse grains also for prolonged milling time (*e.g.* 64h). A more uniform fine powder is instead delivered by the CY, operating under best milling conditions, although

for a grinding time not shorter than 16 hours.
It should therefore be highlighted that, when operating under favourable mill configuration, the HM jar (and more likely also the other newly designed ones) requires much shorter milling time than the CY to produce a well-ground end product. It can thus be suggested that the design of new shapes for the jar of the planetary ball mill could represent an alternative way for diminishing the grinding process overall duration, allowing to save time and energy.

Besides size reduction, XRPD-LPA provided information on the dislocation density (ρ) produced by the two jars, reported in figure 4.8d. It can be seen that at $\omega/\Omega + 1$ = -1.0, the HM jar immediately engenders a certain dislocation density which is then constant as a function of milling time, whereas for the CY it increases with time. For $\omega/\Omega + 1$ = -2.6 instead, for both jars this quantity steeply grows in the first 1-8 hours.
Figure 4.8c also highlights the influence of milling time on iron contamination from the grinding media of the end product. Although more hints about this phenomenon will be reported in the next subsection, it should be noticed that the iron content is larger for powders produced with the HM than with the CY, especially if jar-to-plate velocity ratio is high and outside to the best milling conditions range (*e.g.* ω/Ω+1 = -2.6, right side of figure 4.8). However, what is more important to notice is that iron contamination closely relates to milling time and for the HM in particular, it is shown to reach approximately the 15% of the sampled powder for the longest milling time whereas for 1h milling it is almost absent, long enough for HM to work properly. Therefore, for the newly designed jars contamination can be controlled by properly choosing the milling time.

4.1.4 Effect of jar shape on wear

During the grinding process, wear of milling media and/or jar (depending on their mutual composition and surface hardness) is inevitably engendered by mutual friction and collisions. Debris are mixed with the charge, leading to the contamination of the end product [8, 12, 110]. While in a few cases wear has been demonstrated to play a positive role by introducing reagents or catalysts [110, 179], it generally deteriorates the quality of the end-product, to the point that sometimes contaminants must be removed in a post-process step [170, 180]. As a general tendency, wear increases with milling time and angular velocities (as suggested also by figure 4.8d) while it is reduced by high mill charge adhesion [12, 181] and it is also strongly affected by number and diameter of balls, ruling the amount of collisions [170, 181].
In order to assess the influence of jar shape on this phenomenon, the Fe content of samples, ground in all the presented jars for 32h under different velocity ratios, was estimated through XRPD-LPA of collected patterns. Results are reported in figure 4.9 as a function of $\omega/\Omega + 1$, and, with respect to the CY, higher Fe contamination is immediately observable for the the newly designed jars, especially for the T and 3L.

All milling variables except from jar shape being equal, a plausible explanation of the increase of wear could relate to the obstacles introduced for the design of the new profiles, driving balls along trajectories that could promote the development of regions with higher impact density and magnitude, in principle more wear prone. This hypothesis is supported by figure 4.10 depicting, for Ω = 200rpm and $\omega/\Omega + 1$ = -1.8, the maps of the balls-jar contact events and their magnitude in terms of normal relative velocity (see the color scale) obtained from simulations. Beside indicating an increase in the number of high normal velocity impacts for the newly-designed jars, maps also reveal a not uniform distribution of collisions density, with a concentration of high-velocity events near the corners. On the contrary, in the CY jar this kind of collisions is randomly distributed along the whole internal profile.

It can be concluded that, in addition to the performance in comminution, the influence on wear has to be properly considered while choosing the most suitable jar shape for each grinding operation. Anyway, many strategies can be adopted to limit or even avoid this phenomenon. The most immediate and crucial is the careful selection of jar and balls materials [12, 182] and particularly, it should be noticed that using

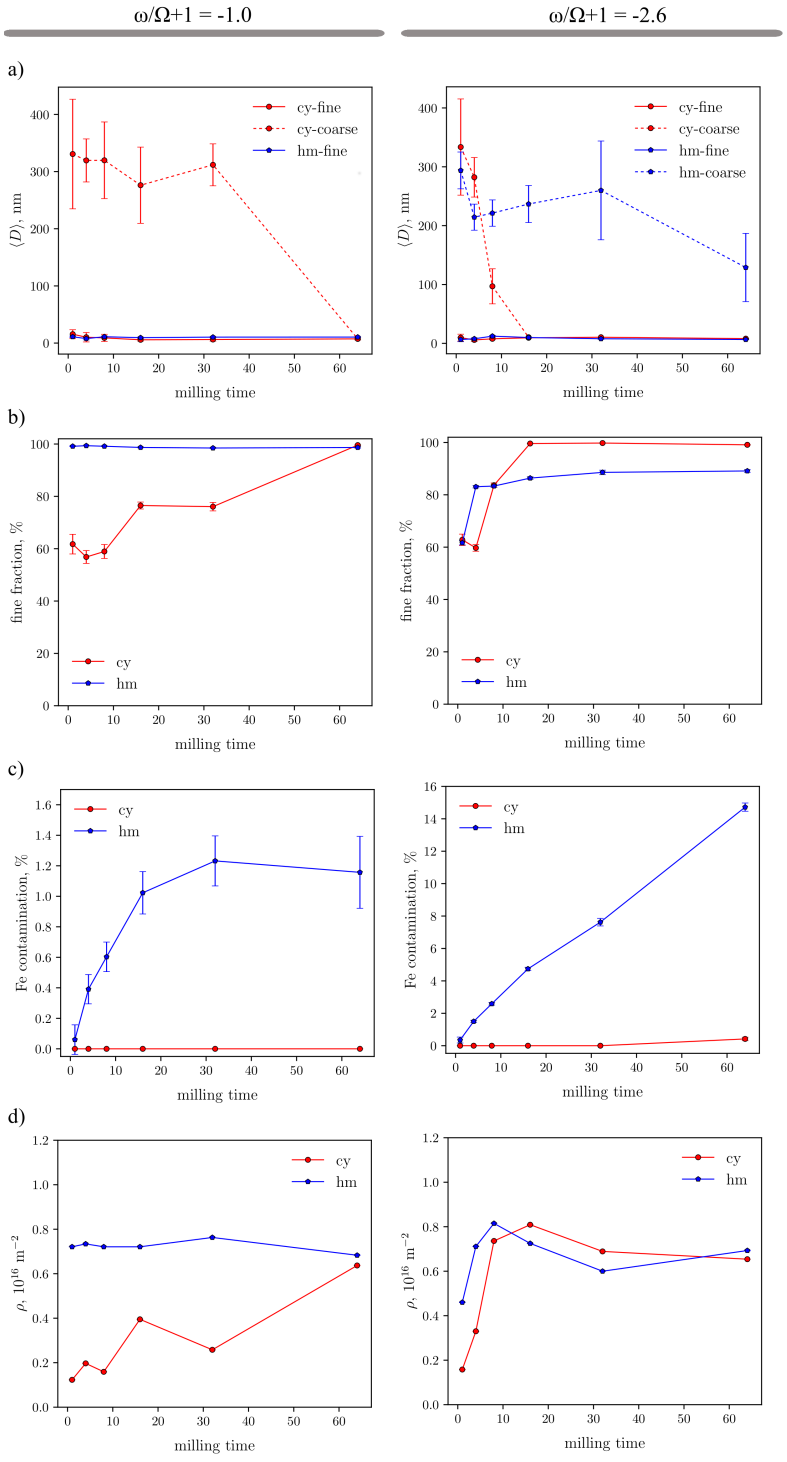

Figure 4.8: LPA data for calcium fluoride milled in the CY and the HM jars for different milling times and $\omega/\Omega + 1$ = -1.0 (left), -2.6 (right) velocity ratios. Data reported as a function of milling time are (a) the mean domain size $\langle D \rangle$, (1 or 2 distinct distributions of sizes were necessary to properly model the data depending on the inhomogeneity of the powders), (b) percentage of fine fraction, (c) iron contamination percentage and (d) average dislocation density, ρ.

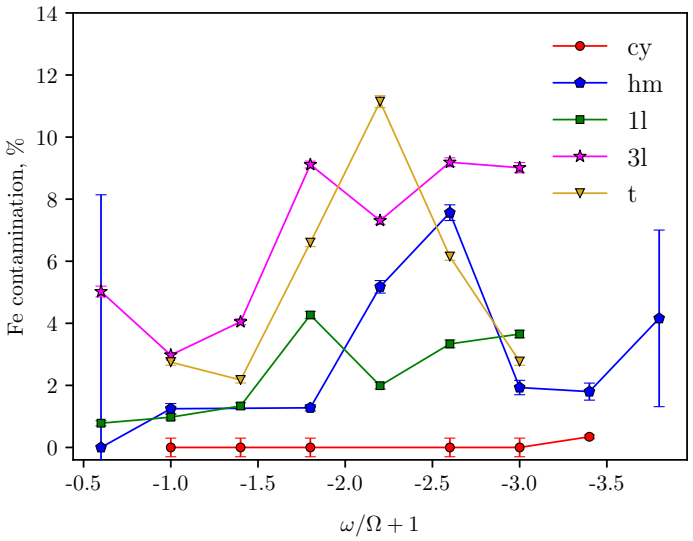

Figure 4.9: Percentage of Fe content in calcium fluoride samples ground in all the investigated jars for 32h under different velocity ratios. Higher contamination can be observed for the newly designed jars.

– when possible – the same material for the milling media and the mill feed allows to eliminate cross-contamination. Velocity ratio also plays a crucial role and, being newly designed jars efficient also at low velocity ratio, these conditions should be preferred. Finally, as introduced in the previous section, the set up of the proper milling time could provide a well ground end product as well as reduced contamination. Particularly, results reported in figure 4.8c, show that the milling time required to produce a finely ground powder are quite short when HM operates at optimal velocity ratio (*e.g.* $\omega/\Omega + 1$ = -1.0), and in this condition contamination is almost absent or comparable with that developed by grinding the same powder in a CY jar for 32h. It can therefore be concluded that adopting the new design jars is a viable solution to produce finely comminuted and homogeneous powders with limited contamination, with the advantage of a process time much shorter than required by conventional ball milling jars.

4.1.5 Conclusive remarks

At the aim of enhancing the comminution efficiency of the ball milling process, 4 new designs for the internal shape of the jar (HM, 1L, 3L, T), introducing different kind of obstacles along the perimeter of the standard CY vial, were proposed. The newly designed jars were tested through multibody dynamics simulations and *in operando* video recordings of the milling process for different $\omega/\Omega + 1$ velocity ratios. Visual inspection of simulations and camera movies showed that the new designs promote the detachment of the balls from jar walls, augmenting the complexity of balls motion with respect to the CY jar. Simulations pointed out that this reflects in an increase (i) of the number of high-normal-velocity impacts, especially effective for the comminution of brittle materials, and (ii) of the average normal stress energy available, for velocity ratios ranging from $\omega/\Omega + 1$ = -0.0 to -2.6, where balls start to roll along jar walls. XRPD-LPA, giving insights on the average crystallite size of the end product, were performed on ground calcium fluoride and confirmed simulations predictions. Indeed, starting from the lower velocity ratios and for a broader range than the standard CY, newly designed jars showed higher efficiency, providing a finer and more homogeneous end product.
Finally, the effect of milling time was investigated for the CY and the HM jars, the latter chosen as representative of all the other new designs. LPA of calcium fluoride milled for different times, pointed

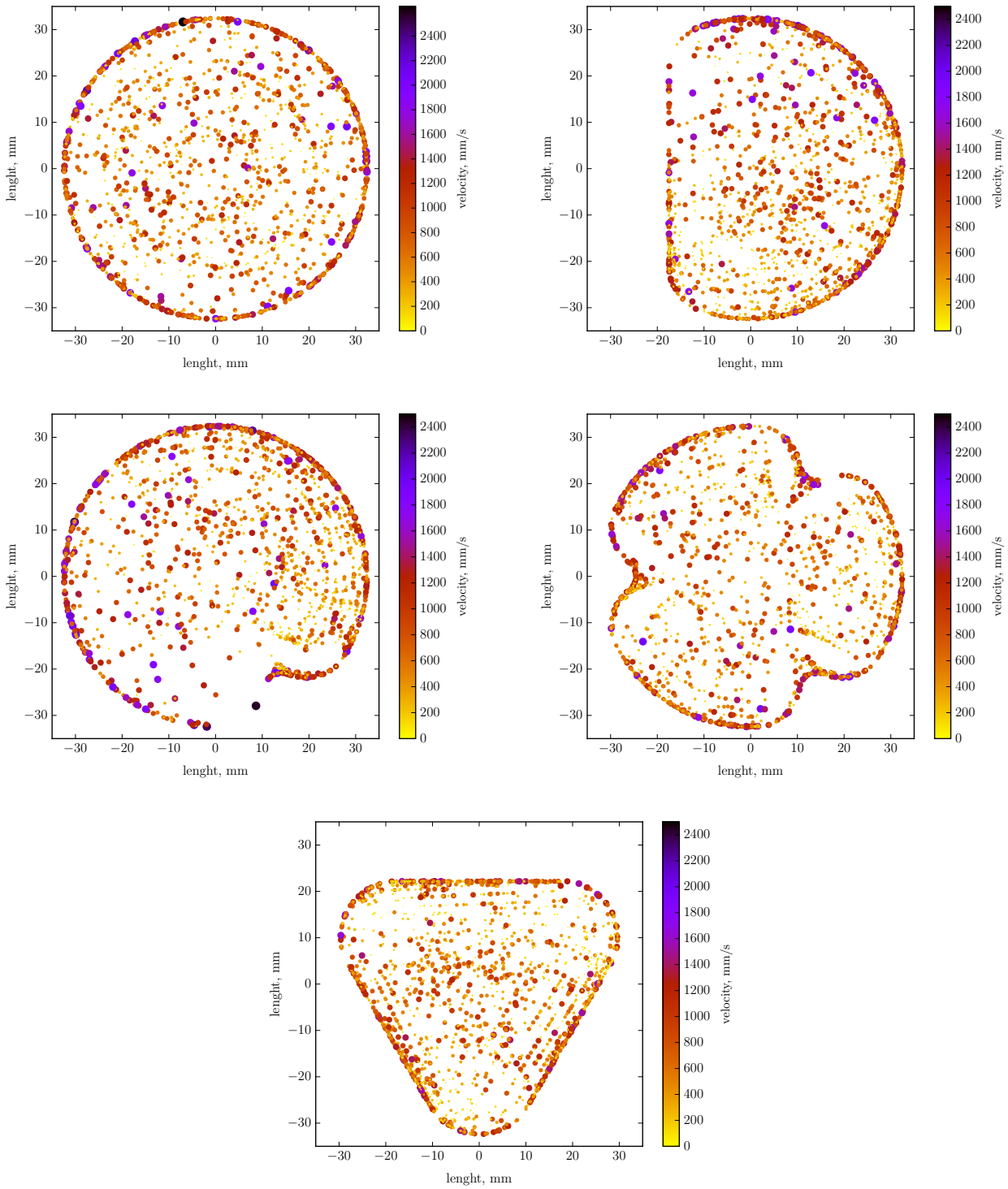

Figure 4.10: Maps of balls-jar contact events from simulations ($\omega/\Omega + 1$ = -1.8, steel-steel interaction). The normal component of the relative impact velocity during each collision defines the color scale and the radius of each point.

out that new designs produce a well ground end product even for milling time as short as 1 hour, whereas the traditional CY requires at least 16 hours to give a similar result even if best operating conditions are used. Jar shape is therefore a crucial variable for the reduction of time and energy required by the milling process. The only downside of these jars is the contamination of the end product from milling media, that can however be almost completely avoided through a proper setup of milling variables (*e.g.* jar and balls materials) and milling time.
Given the different behaviour of the presented jars, a particular shape should therefore be selected depending on the required milling results, *e.g.* in terms of normal to tangential force ratio, available power and achieved contamination.

4.2 Cylindrical and Half-Moon jars: a direct comparison

● ○ ● ○ ● *Part of this section has been adapted from [92, 183].*
In this section a more detailed comparison between the CY and the HM jar is presented. The latter was selected among the other newly-designed jars owing to the good performance demonstrated both in terms of comminution and level of contamination of the end-product.
Part of the results reported hereafter was already introduced in section 4.1 but more specific information are added, especially for microstructural properties of ground fluorite.
The first subsection reports the paper *Effect of jar shape on high-energy planetary ball milling efficiency: Simulations and experiments*, published in the *Material and Design* journal [92], resuming and comparing the experimental and modelling investigations carried out for the CY and the HM jars. It should be underlined that, despite the outcomes of the analyses on milling time and wear evidenced in section 4.1, and being contamination not relevant to this work, experimental tests lasted 32 h for both jars, so to allow the CY to operate under optimal conditions.
The second subsection explores the influence of milling time on the microstructural changes in ground CaF_2, focusing particularly on the crystallite size distribution. Presented results are published in the data article *Homogeneity of ball milled ceramic powders: effect of jar shape and milling conditions*, in the *Data in Brief* journal [183].

4.2.1 Effect of jar shape on high-energy planetary ball milling efficiency: Simulations and experiments

Authors: M. Broseghini, M. D'Incau, L. Gelisio, N.M. Pugno and P. Scardi[†]. *Adapted from [92].*

Abstract

Enhanced comminution in a planetary ball mill was achieved by suitably re-designing the jar shape. Compared with a traditional cylindrical vial of circular cross-section, the new jar was modified internally to have a flat wall portion resulting in a half moon cross-section. Results from simulations, using a multibody dynamics software, suggest that this geometry increases the number of high-velocity collisions with energy exchange along the axial direction, deemed as more effective in the comminution process. X-ray diffraction line profiles of calcium fluoride (CaF_2) ground in the two jars under equivalent conditions were used to obtain information on the microstructure resulting from the milling process and validate

[†]In this work MB developed the models, performed the simulations, analysed the results and wrote the manuscript, MDI conceived the idea, performed the experimental tests and analysed part of the experimental data, LG helped in simulations data analysis and in drafting the manuscript, NMP revised the manuscript, PS conceived the idea, analysed experimental data and revised the manuscript.

the modelling results. A better homogeneity and a faster reduction of crystallite size was achieved using the new design compared to that using the standard cylindrical vial design. Optimal operating conditions, in terms of jar-to-plate angular velocity ratio, are correlated and discussed according to the model predictions.

Introduction

Planetary ball milling is a widespread and versatile technique for the structural and microstructural property tuning of almost any kind of material. It is often used to grind materials down to the nanoscale, generally providing both comminution and incorporation of defects by extensive plastic deformation, thus supplying the conditions for mechanical activation [6, 7]. Remarkable examples being the mechanical alloying of metals as well as the direct and indirect synthesis of ceramics [8–10]. The method has also proved to be effective in the mechanical exfoliation of bulk systems, for the large-scale production of two-dimensional nanostructured materials - such as graphene and boron nitride nanosheets [15, 16], nowadays of utmost scientific and technological interest. Although rather simple in terms of geometry and working principles (see figure 4.11 and *e.g.* [12]), the versatility and efficiency of the planetary ball mill depend very much on the appropriate tuning of a multitude of milling variables. Among the others, the number and size of the balls, the jar geometry and the velocity of revolving parts should certainly be mentioned. The setup parameters strongly influence the ball trajectories, which in turn, influence the nature and magnitude of the impulsive forces transferred by milling media collisions. These forces can be divided into normal and shear components: the former should promote fracture while shear components induce plastic deformation [1, 15, 174].

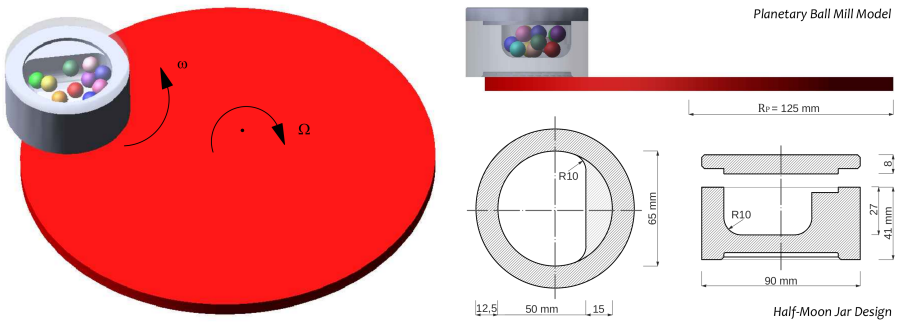

Figure 4.11: Planetary ball mill installing the Half Moon jar and definition of rotation (ω) and revolution (Ω) angular velocities. The design of the new half-moon shaped jar is also reported.

As an alternative to extensive experimental testing, deemed as expensive and time-consuming to the point of being most often unfeasible, a dynamic-mechanical model of planetary ball milling was adopted [91] to fine-tune milling parameters and establish correlations with the end-product. This model, based on a simple contact scheme depending on a few easily estimable parameters, supplies quick and accurate predictions of system efficiency under different operating conditions and is, in principle, valid for any material of interest. The effect of jar (ω) and plate (Ω) velocities was investigated, providing a detailed picture of the kinematics and dynamics of the milling bodies, together with a description of contact events, supporting an outright understanding of ball motion regimes. An assessment of the kinetic energy available, both along normal and tangential directions, was obtained and results validated against experimental data. In particular, best milling conditions, corresponding to the highest impact energy, were found to correlate with the most disordered ball motion, which develops within a well-defined range of jar-to-plate velocity ratios ($\omega/\Omega + 1$).

Beyond the influence of plate and jar angular velocities, the present work investigates the effect of jar shape on the process efficiency. Particularly, the ratio of normal-to-shear transferred loads is considered to be an essential parameter in the design of end product characteristics, in terms of structure and microstructure. To increase the number of collisions with high-normal-velocity component, a new type of jar was designed. Simulation results, obtained using the above-mentioned multibody dynamics model, were analysed in terms of kinetic energy, balls trajectories and probability distribution of velocities, in both the normal and tangential directions. The experimental validation was supported by X-ray Powder Diffraction Line Profile Analysis (XRPD-LPA) of ground calcium fluoride (CaF_2).

Methods

Planetary ball mills consist of two or more jars rotating both around its own axis and the line of symmetry of the supporting plate (radius $R_P = 125$mm, see figure 4.11). The motion of the milling media (balls) inside the vial, which is driven by the resulting field of two centrifugal forces and the Coriolis force, causes impacts that transfer compressive and shear forces to the powder charge. These forces lead to structural and microstructural alterations and/or mechanochemical effects [184, 185].
As shown by Burgio et al. [111], at optimum milling conditions the trajectory ideal for a single ball follows a point on the vial circumference until the resulting field of forces acts to carry the ball across the jar to the opposite point, perpendicularly to the jar surface. In a real scenario, trajectories depend on the interactions between many balls. In which case, forces are exchanged in every possible direction with respect to the impact reference frame.
To enhance the normal component, a Half-Moon shaped jar (HM) is proposed, with a design based on a flat surface halfway between the original curved wall and the vial axis. This way, when balls rolling along jar wall approach the flat surface, they are forced to follow the *ideal path*, therefore increasing the amount of energy along impact axis and thus causing a more intense comminution effect.

Computer Simulations Computer simulations are a useful tool to explore thoroughly and characterise the milling process, providing insights into kinematic and dynamic quantities, mostly inaccessible to experiments. In this study, the Fritsch Pulverisette 4 (P4 [109]) planetary ball mill, equipped with either the Cylindrical (CY) or the HM jar, was modelled using the multibody dynamics software MSC.Adams [81], as reported in [91]. Twelve steel balls (radius 6 mm) were placed randomly inside each jar and angular velocities ω and Ω were applied to the two cylindrical shafts connecting the revolving parts (physical properties of the milling media and jars are reported in table 4.2). Owing to the intrinsic multibody nature of the system, the solution of the Lagrangian equations of motion of the milling media was determined using the Hilbert-Hughes-Taylor (HHT, [155, 156]) integrator, with automatic step tuning and maximum numerical error of 10^{-8}. Simulations lasted 24 seconds but, to allow motion homogenisation after media insertion, the first 4 seconds were discarded during data analysis. It is worth noting that the powder charge, typically a few percent volume of the milling media, was not explicitly modelled but accounted for by a suitable selection of contact parameters and friction properties. This choice was based on the work by Rosenkranz *et al.* [18] who, by inspecting camera images revealing the formation of powder coatings on balls and jar surfaces, concluded that the presence of the mill feed strongly affects friction coefficients while not substantially influencing restitution and therefore damping properties. To account for friction within the MSC.Adams model, the force prescribed by the (hard-coded) Coulomb model was added to the equation of motion with the friction coefficient, expressed as a function of slip velocity, smoothly varying from the static (μ_s) to the dynamic (μ_d) value. These parameters can be experimentally determined, for example by pin-on-disc tribological tests [51], for each couple of analysed materials.

The contact scheme plays a crucial role, as it rules the interactions among rigid bodies. The hard-coded

CY, HM Jars (AISI 304)		Spheres (AISI C1020)	
density	8.03g/cm^3	density	7.85g/cm^3
Young modulus	193GPa	Young modulus	200GPa
Poisson ratio	0.29	Poisson ratio	0.29

Table 4.2: Physical properties of the milling media, the cylindrical and the half-moon jars for the presented case study.

MSC.Adams impact function, belonging to the continuous approach [25], adds a force-displacement law to the equation of motion, including the contribution of a non-linear spring, F_k, and a linear damper, F_d, (Dubowsky and Freudenstein impact pair model [72]),

$$F_c = F_k + F_d = ku^n + c\dot{u},$$

where u and $\dot{u}$ are the relative displacement and velocity of colliding bodies, whereas k and c are the spring generalised stiffness and the damping coefficient, respectively. To prevent discontinuities, c varies from 0 to a maximum value, c_{max}, depending on the relative displacement of colliding bodies. An estimate of c_{max} was determined from the classical solution of the damped vibration of a mass spring system [72], starting from the experimental measurement of the coefficient of restitution (ball-against-plane drop test [88]), e. Then, a parametric numerical analysis provided the u value at which c_{max} has to be applied. For the spring component, fixing $n = 3/2$, an estimate of k was derived from the Hertzian theory of contacts [26], applied both to the ball-ball and to the ball-plane (approximating the jar surface) impacts. Values of parameters introduced in contact and friction schemes in this study, are reported in table 4.3.
The typical simulation output consists of a complete set of dynamic variables for milling media as well as quantities pertaining to each contact event, thus allowing for a full understanding of the evolution of the investigated system. Moreover, each computed quantity can be decomposed into normal and tangential components with respect to the local impact reference frame, thus highlighting preferential directions for energy exchange between milling media and mill feed. The most intuitive quantities to investigate are the trajectories of milling media, offering a quick understanding of the complexity of the motion, directly related to the energy transfer mechanism (see [91]).
To compare the efficiency of the different jars, it is also useful to calculate the impact kinetic energy of the system (E_I), normalised over jar internal volume (V) and simulation time (τ), *i.e.* the impact power density. This quantity is computed in the impact reference frame to provide an upper bound estimate of the energy available for grinding the mill charge [18, 22, 82, 117, 136],

$$\frac{E_I}{(\tau\, V)} = \frac{1}{2\tau V}\sum_{j=1}^{C}\frac{m_{1j}m_{2j}}{m_{1j}+m_{2j}}\,\dot{u}_j^2, \tag{4.1}$$

where m_i is the mass of the i-th colliding body (the mass of the jar is assumed to be infinity) and $\dot{u}$ the relative velocity. The summation runs over C, which is the number of points sampling collisions during the simulation time period (τ) with mean output step size of $\approx$ 3E-3 (integrator parameters are h_{max} = 1E-6 and $step$ = 100). It must thus be stressed that the absolute scale for the power impact density implicitly depends on the choice of these parameters and therefore is arbitrary and not directly comparable with power available in a real apparatus.
The normalisation factor V accounts for the different internal volume of the jars, respectively 72 mm^3 (CY) and 62 mm^3 (HM), limiting the space for ball motion and thus the transferred energy. By introducing the components of the relative velocity along ($\dot{u}_n$) or perpendicular ($\dot{u}_t$) to the impact axis, this quantity

can be decomposed into its normal and tangential components, thus highlighting the preferential mode of energy exchange. Finally, an additional view of the energy exchange mechanism, completing the comparison between CY and HM jars, is provided by the probability distribution of the relative velocities of colliding bodies during impacts.

sphere-sphere generalized contact stiffness, k_{ss}	252,146N/mm$^{3/2}$	Hertz Theory
sphere-plane generalized contact stiffness, k_{sp}	350,236N/mm$^{3/2}$	Hertz Theory
restitution coefficient, e	0.516	drop test, $e = \sqrt{h/h_0}$
sphere-sphere contact damping, $c_{m,ss}$	10.1kg/s	Damped Mass-Spring system Sol.
sphere-plane contact damping, $c_{m,sp}$	17.5kg/s	Damped Mass-Spring system Sol.
Steel-Steel μ_s	1.00	literature
Steel-Steel μ_d	0.80	tribological test
Steel-Fluorite μ_s	0.25	literature
Steel-Fluorite μ_d	0.20	tribological test

Table 4.3: Values introduced in contact and friction models and methods used for their derivation.

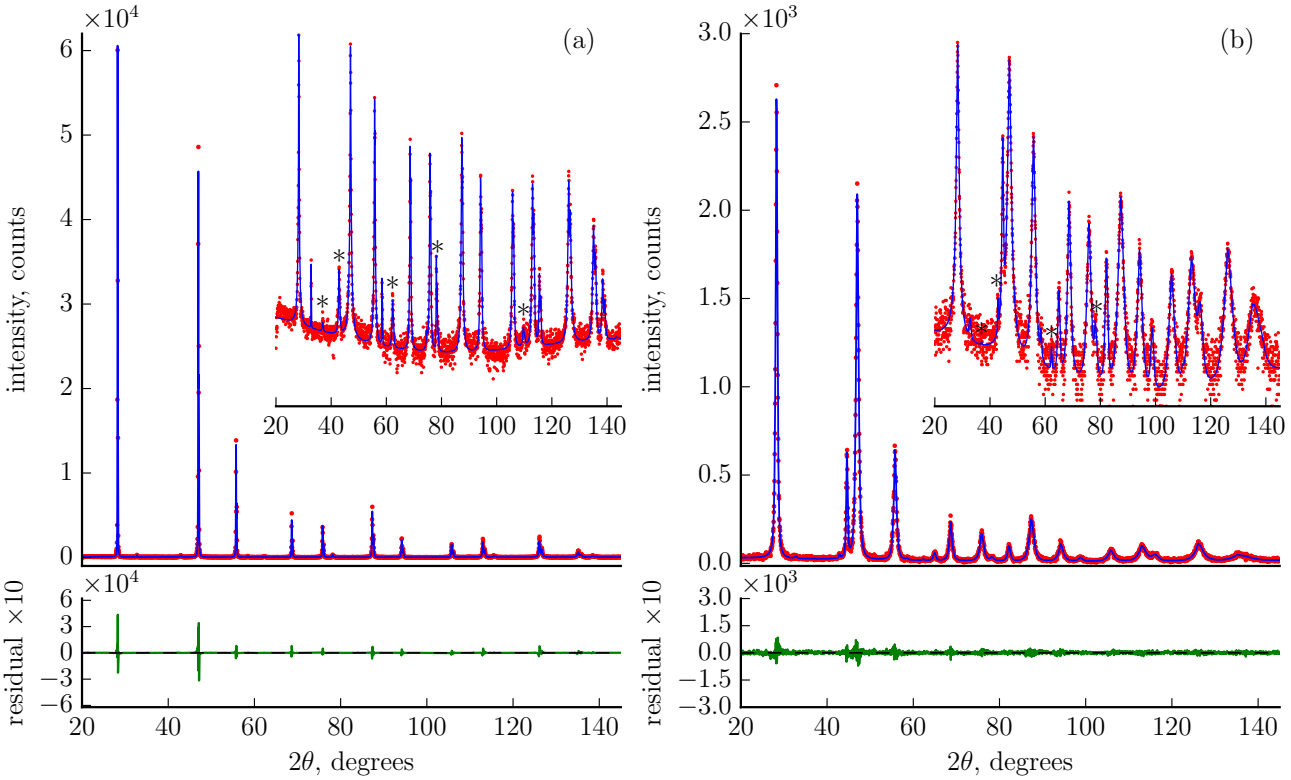

Figure 4.12: XRPD pattern of (coarse-grained) pristine fluorite powder (a); same powder after ball-milling in Half-Moon jar, for 32h at $\omega/\Omega + 1$ = -2.2 (b). Experimental data (red circle) are shown with the WPPM profile (blue line), and their difference (residual, green line below). The inset shows the same data in log scale to highlight details and profile modelling quality: some of the weak peaks (*) are from MgO, present as impurity phase and also included in the WPPM.

Experimental techniques X-Ray Powder Diffraction (XRPD) was employed to characterize the structure and microstructure of the end product, in order to assess the effect of grinding conditions and validate the model. XRPD patterns were collected using $CuK\alpha$ radiation and a Rigaku PMG/VH diffractometer with a set of optical components (slits and bent graphite analyzer crystal) producing a narrow and symmetrical instrumental line profile across a wide angular region. The instrumental response was assessed by measuring a NIST SRM sample (660a LaB_6, [186]), modelled by pseudoVoigt functions and parameterized to be used in following analyses of the powder pattern [140]. Ball milled fluorite samples were analysed under the same experimental conditions: details can be found in [91, 138]. The powder patterns were analysed by Whole Powder Pattern Modelling (WPPM, [140–142]), assuming a lognormal distribution of spherical nanocrystalline domains and dislocations generated by the grinding process [165, 187]. Besides information on mean size ($\langle D \rangle$) and dispersion of the scattering domains, the WPPM analysis provides data on the inhomogeneous strain distribution, which can be related to the dislocation density (ρ) according to the theory of Krivolgalz and Wilkens (see [140] and references therein). As an example of WPPM analysis, XRPD experimental data and modelling results for pristine and ground fluorite (HM jar, $\omega/\Omega + 1$ = -2.2) are reported in figure 4.12.

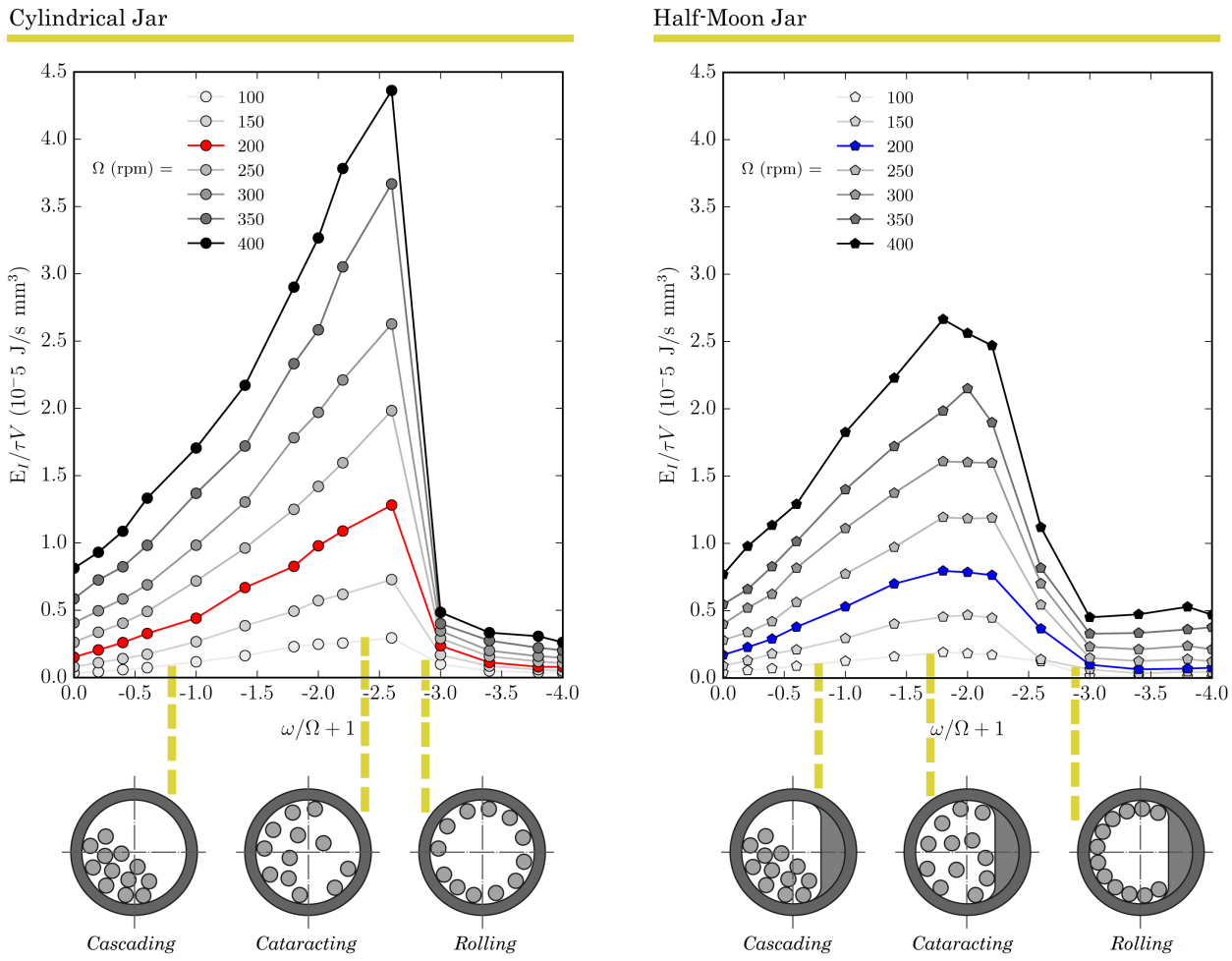

Figure 4.13: Impact power density (equation 4.1) for the steel-steel interaction, for the cylindrical (left) and the half moon (right) jars. Curves are computed for different plate velocities (Ω). The typical ball trajectories corresponding to the different conditions are also sketched.

Results and Discussion

The main purpose of this work was to investigate the different grinding actions of the CY and HM jars and the dependence of the process efficiency on the plate (Ω) and jar (ω) velocities. To properly account for mill charge and to compare numerical and experimental data collected on ground fluorite samples, two extreme conditions were simulated, namely the (i) steel-steel (*i.e.* milling media only, no mill charge) and the (ii) steel-fluorite interactions (*i.e.* jar surface completely covered by fluorite). The experimental case was expected to fall between these two boundary conditions. As previously discussed, no parameters were changed apart from the friction coefficients (Table 4.3) to simulate the two cases.
Figure 4.13 illustrates the impact power density (equation 4.1) for steel-steel interaction for sets of simulations performed at different fixed angular plate velocities Ω and increasing ω. Interestingly, Ω strongly affects the amount of energy exchanged in the process, whereas it moderately alters the location, in terms of $\omega/\Omega + 1$, of the maximum of the curve, corresponding to the maximum overall efficiency of the process. While the CY jar transfers the larger power at approximately $\omega/\Omega + 1$ = -2.6, the optimal condition of the HM jar, although less energetic than its CY counterpart, extends over a wider range, from $\omega/\Omega + 1$ = -1.8 to -2.2. The HM jar, therefore, has a more robust grinding action, being less sensitive to variations in milling parameters. Moreover, it should be noted that the volume and the longest free path for ball motion is smaller for the HM than for the CY jar, thus resulting in reduced acceleration, velocity and kinetic energy transfer from the milling media to the powder. The analysis of ball trajectories reveals a correlation between motion regimes and energetic efficiency (see figure 4.13). In particular, by decreasing the angular velocity ratio, both jars demonstrate an increasingly disordered cascading motion, until it turns into a cataracting regime, providing the best milling conditions (see [91]). Above a threshold value of angular velocity ratio, balls tend to roll on (CY) or stitch to (HM) the jar surface, therefore strongly limiting the amount of transferred energy.
Figure 4.14 reports the ball-ball (a) and ball-jar (b) components of the impact kinetic energy calculated for Ω = 200rpm, further divided into normal and tangential components with respect to the local impact reference frame. In both cases, contacts among balls clearly play the major role and the largest amount of energy is exchanged in the tangential direction. However, it is interesting to notice that the ratio of energy transferred in the normal direction to the total energy ($E_I(normal/tangential)$) is larger for the HM than for the CY jar: this information is crucial to design a milling process exchanging energy along a specific direction.
The probability distribution of the relative velocities of colliding bodies is reported in Figure 4.15 for both jars. Even if the overall efficiency, as already pointed out, is higher for CY than for HM jar, the comparison of relative velocities offers insights into the typical ranges of exchanged energies. Before and at the angular velocity ratio $\omega/\Omega + 1$ = -1.8, corresponding to the HM jar optimal milling conditions (upper part of figure 4.15), for the tangential component the CY jar exhibits a larger number of high-relative-velocity events (say, $>$ 500 mm/s). Turning to the normal velocity, by contrast, the HM jar performs better. Although the relative frequency of high-velocity impacts is tiny, it should be noticed that this type of impact exchanges the highest amount of energy, and is, therefore, the most effective event in the comminution process. In fact, fragmentation and related phenomena (*e.g.* work-hardening) are strictly nonlinear, so the sum of energy released by low-relative-velocity contacts may not be as significant as that associated to a single high-relative-velocity event [178]. In particular, impacts along the normal direction are supposed to fracture brittle powders more efficiently than impacts with a strong tangential component [1, 15, 174]; therefore, as the fraction of significant events along the normal direction is higher in HM than in the CY jar, the former is expected to be more effective in size reduction of brittle materials such as fluorite.
Figure 4.16 depicts the map of the balls-jar contact events and their magnitude in terms of relative velocity in normal direction for $\omega/\Omega + 1$ = -1.8. While in the CY jar the collision density is uniform,

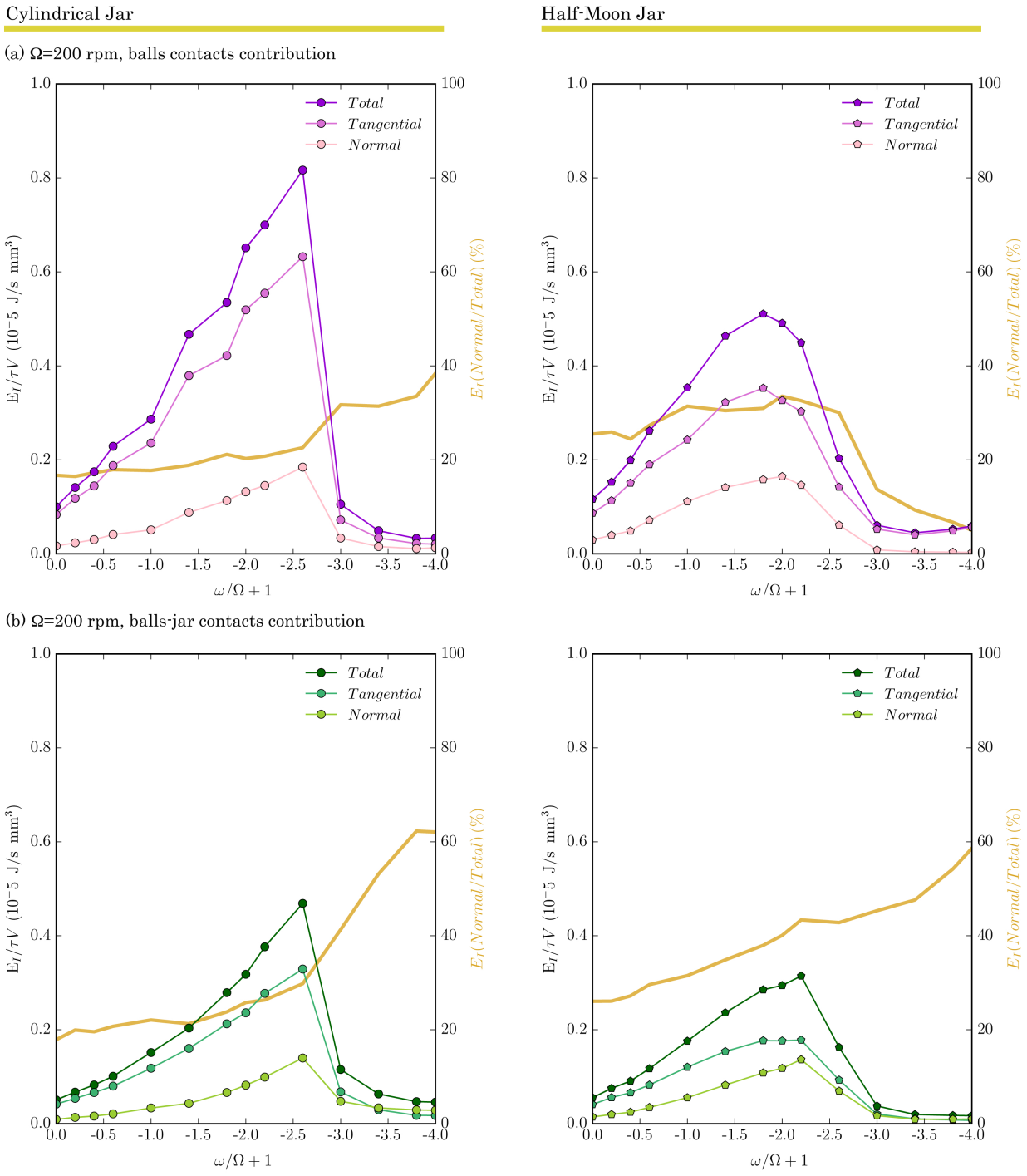

Figure 4.14: Impact power density (equation 4.1) for the steel-steel interaction, for the cylindrical (left) and the half moon (right) jar computed for Ω = 200rpm and divided into ball-ball and ball-jar contacts contributions. These quantities are also broken down into its normal and tangential components (with respect to the local impact reference frame). The yellow line depicts the fraction of energy exchanged along the impact axis ($E_I(normal/tangential)$).

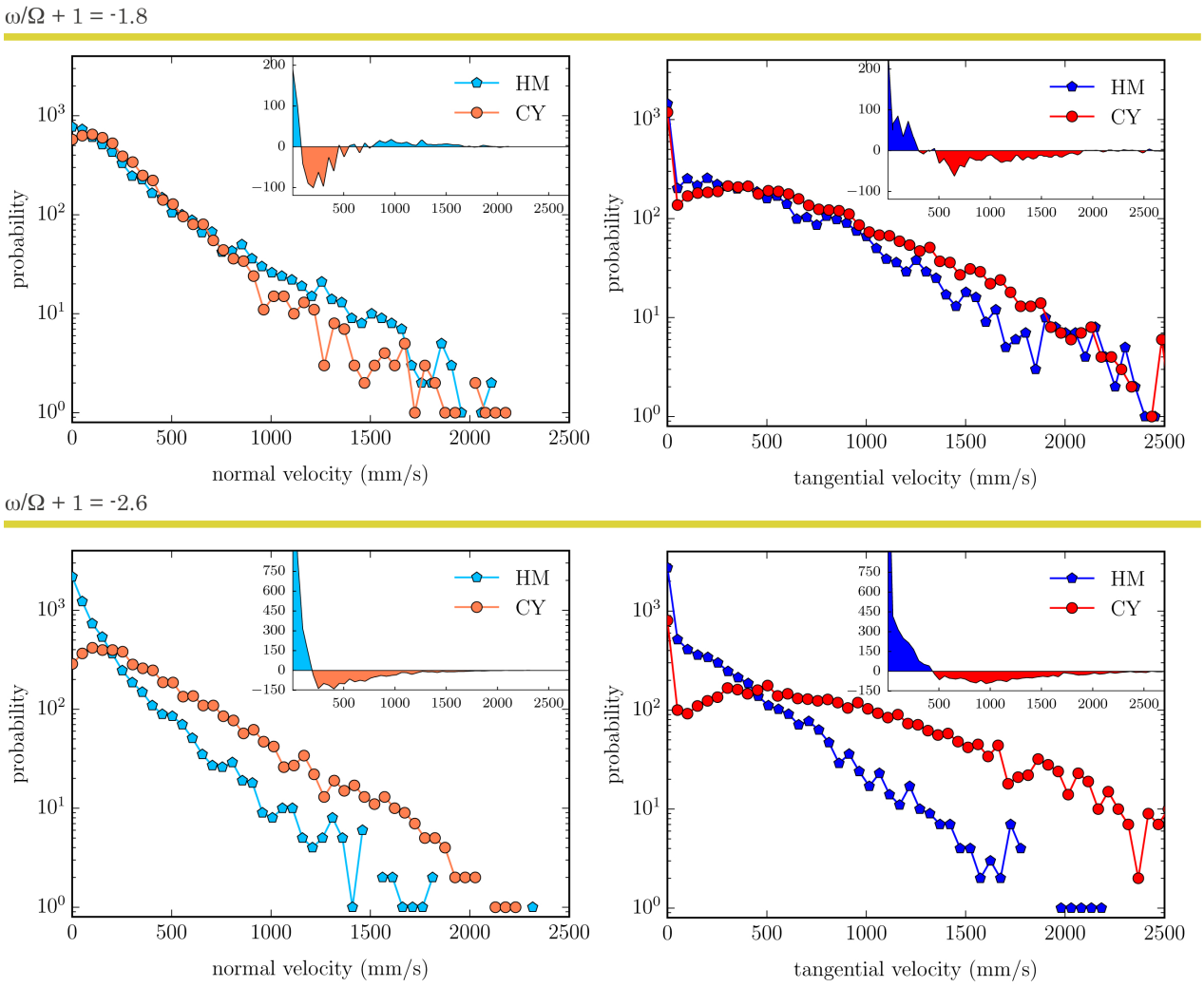

Figure 4.15: Probability distribution of normal (penetration, left) and tangential (slip, right) components of the relative velocity of colliding bodies for both $\omega/\Omega+1$ = -1.8 and -2.6 (being Ω = 200rpm), respectively corresponding to the highest-efficiency condition for the CY and HM jars. The insets report, in linear scale, the difference between HM and CY probability distributions.

this is not true for the HM jar, where regions with higher impact density/magnitude exist, particularly concentrated near the upper corner. In agreement with ω and Ω rotation wise, this indicates an increase in number of balls following the ideal trajectory of high-energy exchange in the normal direction for the HM jar, as expected at the design stage.

For an angular velocity ratio $\omega/\Omega + 1$= -2.6, the efficiency of the CY jar becomes the highest, while HM exchanges markedly less energy (see figure 4.15). Beyond this value, a ball-rolling mode establishes in both jars and high-relative-velocity impacts almost vanish. CY jar efficiency is still higher than HM's but, as discussed later, experimental data demonstrate that this condition is generally not so effective. The right side of figure 4.15 reports the tangential (slip) component of the relative velocities of colliding bodies: for higher-relative-velocity events, CY always exceeds the HM jar.
So far, only the steel-steel case (*i.e.* no powder charge) has been discussed. To validate model predictions, a comparison of simulations and experimental XRPD data was performed for calcium fluoride (milled at

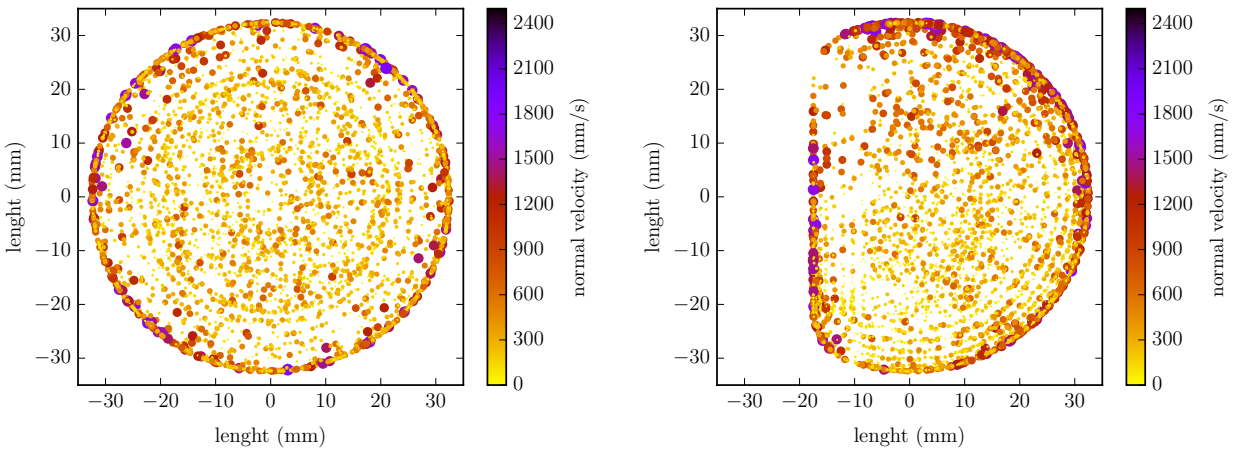

Figure 4.16: Map of balls-jar contact events in the CY (left) and HM (right) jar at Ω = 200rpm and $\omega/\Omega + 1$ = -1.8, for the steel-steel interaction case. The relative velocities during each collision define the color scale and the radius of each point. HM jar clearly shows a concentration of events in the upper corner.

Ω = 200rpm for 32 hours). As already stated, the effect of the milling charge in simulations has been accounted for by modifying the friction parameters (μ_s and μ_d, see table 4.3).
For the HM jar, figure 4.17a illustrates the comparison between the impact power density computed for plate velocity Ω= 200rpm, both for the steel-steel (no feed) and the steel-fluorite interaction cases.

As shown for the CY jar in [91], the presence of a fluorite charge reduces friction and (i) shifts the $\omega/\Omega+1$ position of the maximum efficiency to more negative values and (ii) increases the absolute value of the exchanged power density in the HM jar too. In particular, the broad plateau centered at $\omega/\Omega + 1$ = -1.8 found for the steel-steel interaction is replaced by a sharp maximum at $\omega/\Omega + 1$ = -2.2. The same figure also reports results of the WPPM analysis of experimental XRPD patterns collected on fluorite samples ground in the HM jar under the same conditions as those considered in the simulations. Microstructural data are proposed in terms of (i) average size ($\langle D \rangle$) of spherical crystallites (*i.e.* coherent scattering domains) and (ii) dislocation density (ρ). In particular, the more efficient the process, the more $\langle D \rangle$ is expected to decrease (better comminution) whereas ρ, which broadly includes a large variety of defects, is supposed to increase [93, 159–164]. These quantities can be also related to the mechanical properties of the end product, by means of two expressions describing the microstructure effect of the milling process; namely, (i) the Hall-Petch relation [166, 167],

$$\sigma_y = \sigma_i + \frac{k_y}{\sqrt{\langle D \rangle}}, \tag{4.2}$$

where σ_y is the yield stress, σ_i the starting stress for dislocations movement and k_y the strengthening coefficient of the material; and (ii) the Taylor equation of work hardening [168],

$$\sigma_y = \sigma_i + \alpha G b \sqrt{\rho}, \tag{4.3}$$

where G is the shear modulus, b the magnitude of Burgers vector and α a correction factor specific to the material. From these two relations it can be deduced that, the smaller the grain size, the greater is σ_y and the higher is ρ, the more hardened becomes the material. Interestingly, figure 4.17a shows that the impact power density computed from simulations nicely maps the Hall-Petch trend of experimental data, lying in between the steel-steel and steel-fluorite cases, thus validating the simulations and the

speculations on HM jar efficiency. The same applies, to a certain extent, to the dislocation density which however shows a steep increase around $\omega/\Omega + 1$ = -0.6 and a broad plateau below this value.
A comparison of experimental results of fluorite milled in HM and CY jars is shown in figure 4.17b. Two points should be noticed: (i) a smaller crystallite size is obtained in the HM jar than in the CY, whereas (ii) the maximum dislocation density is comparable but more peaked for the CY than for the HM one. A possible explanation for the former observation, perfectly compatible with computer simulations, lies in the larger fraction of collisions along impact axis (compression), which are more efficient to comminute the brittle powder charge [1, 15, 174]. On the contrary, the cylindrical jar exhibits a relatively larger amount of dislocations at its best performance, owing to the higher energy exchange in the tangential mode, which better supports shear deformation components.

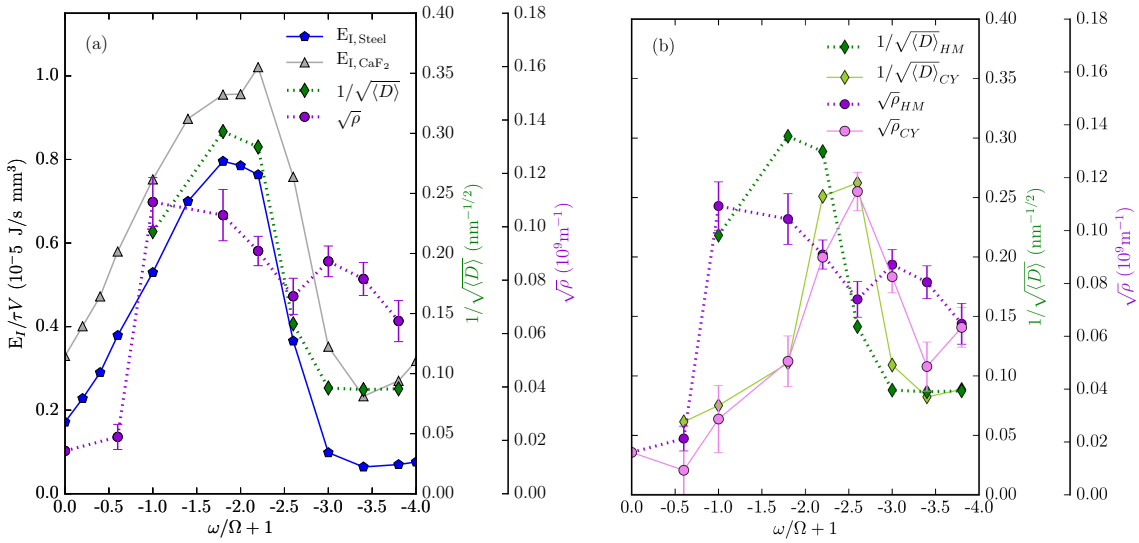

Figure 4.17: Left (a), comparison of simulated and experimental data collected for calcium fluoride ground in the HM jar. Impact power density computed from simulations for the steel-steel ($E_{I,Steel}$, blue pentagons) and the steel-fluorite (E_{I,CaF_2}, grey triangles) interactions nicely maps the trend of experimental data expressed as the reciprocal of the square root of the average crystallite size ($1/\sqrt{\langle D\rangle}$, green diamonds), calculated from the X-Ray powder diffraction pattern of milled calcium fluoride. The dislocation density ($\sqrt{\rho}$, violet circles) is also reported, expressing the deviation from the corresponding ideal structure. Right (b), the same experimental data for the CY and HM jars are compared, illustrating the difference between the two jar shapes, in terms of crystallite size and dislocation densities characterising the end-product at each velocity ratio. Interestingly, while the maximum of these two quantities coincides for the CY case, it is different for the HM jar. Both for experimental and computed data, Ω = 200rpm

In terms of overall performance, it is worth stressing that the HM jar exhibits a wider range of optimal conditions than the CY, thus allowing more robust control of the milling process, reflected on the homogeneity of the resulting powder in terms of domain (crystallite) size. Indeed, as observed in [187, 188], traditional CY jars mostly produce inhomogeneous powders, with a ground fraction (fine) coexisting with less-to-not ground powder (coarse). This information for the discussed case study is revealed in figure 4.18, depicting the distribution of crystallite sizes of calcium fluoride powders ground in the CY and HM jars at increasing velocity ratios, $\omega/\Omega+1$. XRPD data modelling were obtained by WPPM analysis [140] by imposing two lognormal distributions, corresponding respectively to the fine and the coarse fluorite fractions. The existence of these two fractions was also supported by Scanning Electron Microscopy images (see supplementary information in [183]) and confirmed by solid state NMR studies [187, 188]. As shown in figure 4.18, powder ground inside the HM jar is homogeneous (namely a single lognormal curve

is enough to model data) across a relatively broader range of $\omega/\Omega + 1$ velocity ratios than the CY. A more detailed discussion, including the effect of milling time, is reported in [183].

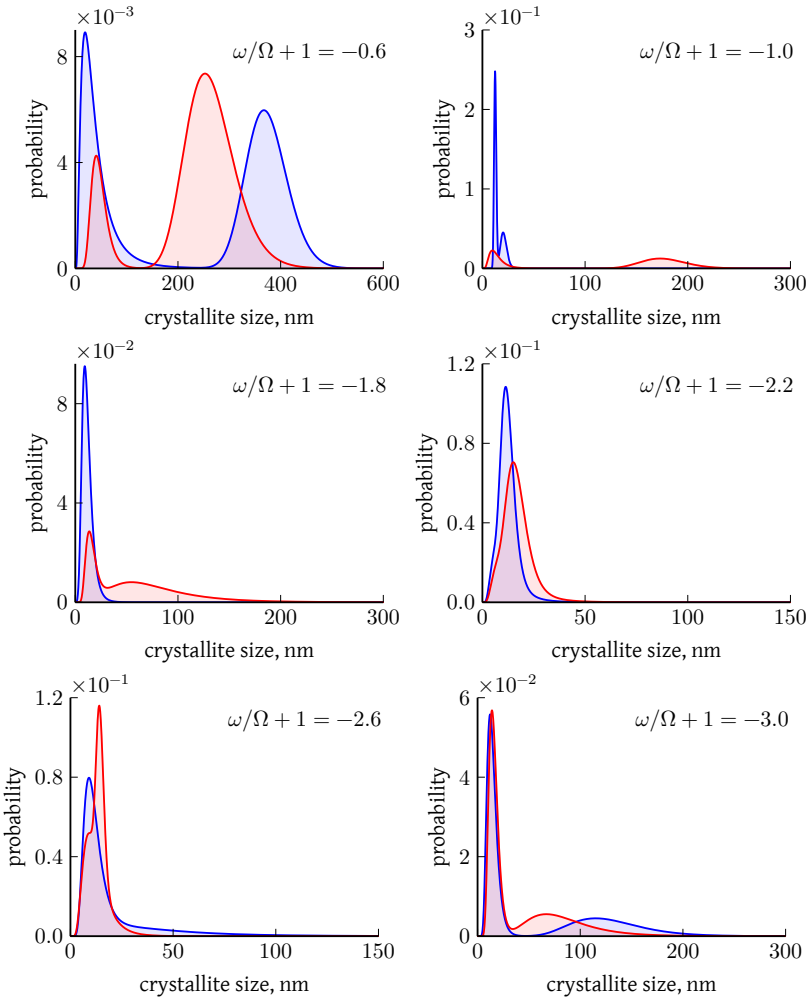

Figure 4.18: WPPM models of crystalline domain size probability distribution of fluorite ground in CY (red) and HM (blue) jars for 32 hours at increasing velocity ratios, $\omega/\Omega + 1$. HM jar produces an homogeneous powder (one lognormal curve) for a wider range of $\omega/\Omega + 1$ than CY.

Conclusions

In this work, an innovative jar design for planetary ball milling has been proposed. The aim of the design was to enhance comminution of the mill charge by providing an increased fraction of energy exchange along the impact axis, with respect to a traditional cylindrical vial. To pursue this goal, a flat wall portion was inserted halfway between the original curved wall and the vial axis, resulting in an half-moon cross section. A rigorous investigation of the HM jar and a comparison with the CY jar has been presented, employing both a dynamic-mechanical multibody model and X-ray powder diffraction data. Specifically, the effect of jar and plate angular velocities on vials efficiency has been discussed in terms of impact power density and the probability distribution of relative velocities of colliding bodies, both divided into normal and perpendicular components with respect to the impact axis. Although globally exchanging less energy than the CY jar, the normal fraction is higher for the HM vial which also provides a larger

amount of high-normal-relative-velocity impacts, supposed to the most effective in the fracture process of brittle powders (calcium fluoride in this study). Moreover, the range of jar-to-plate velocity ratio, corresponding to the highest efficiency (and most disordered ball motion), is wider for the HM ($\omega/\Omega+1$ from -1.8 to -2.2) than for the CY jar (peaked at $\omega/\Omega+1$ = -2.6). Therefore, being less sensitive to milling parameters, the HM jar provides more robust grinding. Modelling predictions are supported and validated by X-Ray Powder Diffraction Line Profile Analysis, giving insights into average crystallite size and defect content of the ground powder. While the CY jar produces a larger amount of defects and homogeneous ground powder only at best milling condition, the HM gives a more uniform and finer end product across a broader range of jar-to-plate velocity ratios. This ongoing research proceeds with the study of different jar geometries, to enhance either the normal or the perpendicular fraction of exchanged energy allowing for the tailoring of the end product characteristics.

Acknowledgements

The present work was partly supported by Fondazione Caritro, under project No 2013-0247 "Mechanical activation to improve bio- availability and reduce adverse effects of drugs in the therapy of chronic diseases". The authors are especially grateful to Dr. D. Catelani (MSC Software) for precious collaboration and support to the research work. NMP is supported by the European Research Council (ERC StG Ideas 2011 BIHSNAM n.279985, ERC PoC 2015 SILKENE nr. 693670) and by the European Commission under the Graphene Flagship (WP14 Poly- mer Composites, no. 696656).

Remarks

Unlike in section 4.1, in the reported paper not the average SE (see equation 3.10) but rather the E_I/τ (see equation 3.8) is used to estimate the energy involved in the process. However, section 3.3 showed these two expression to share approximately the same trend, as confirmed by figure 4.19 reporting, as an example, the normal component of both these quantities. Therefore the presented speculations about the jars performance apply regardless from the formulation adopted for energy.

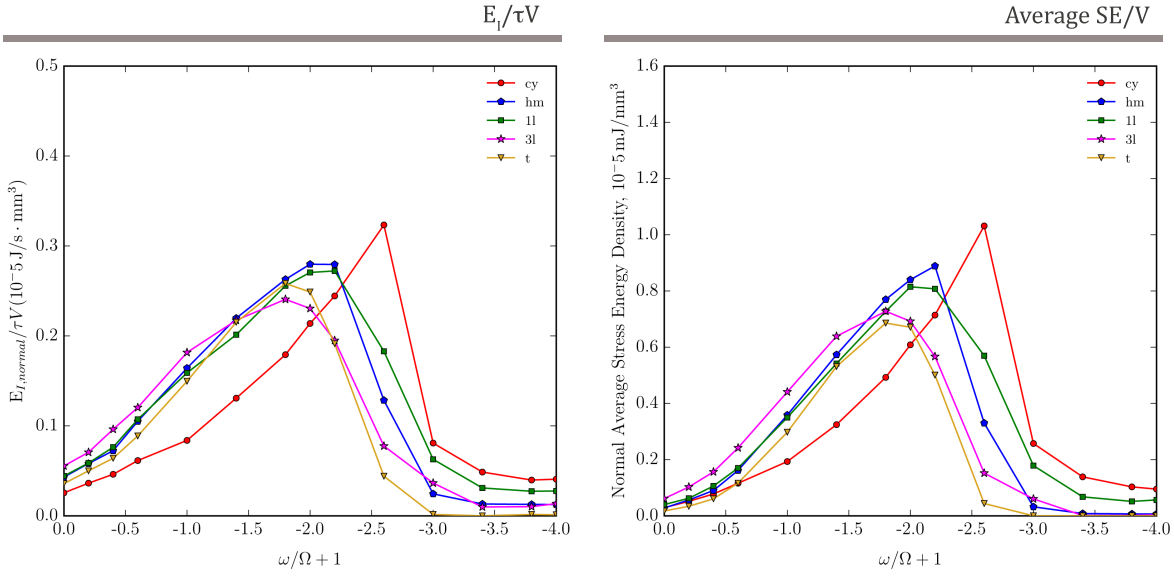

Figure 4.19: Trend of normal component of impact power (E_I/τ, left) and average stress energy (SE, right) for the CY and the newly-designed jars. It is worth noting that the two quantities share the same trend.

Another difference with the analysis reported in section 4.1 is the use of the computer program PM2K [176] instead of TOPAS [177] for the modelling of the XRPD patterns of ground fluorite.

4.2.2 Homogeneity of ball milled ceramic powders: effect of jar shape and milling conditions

Authors: M. Broseghini, M. D'Incau, L. Gelisio, N.M. Pugno and P. Scardi. *Adapted from [183].*

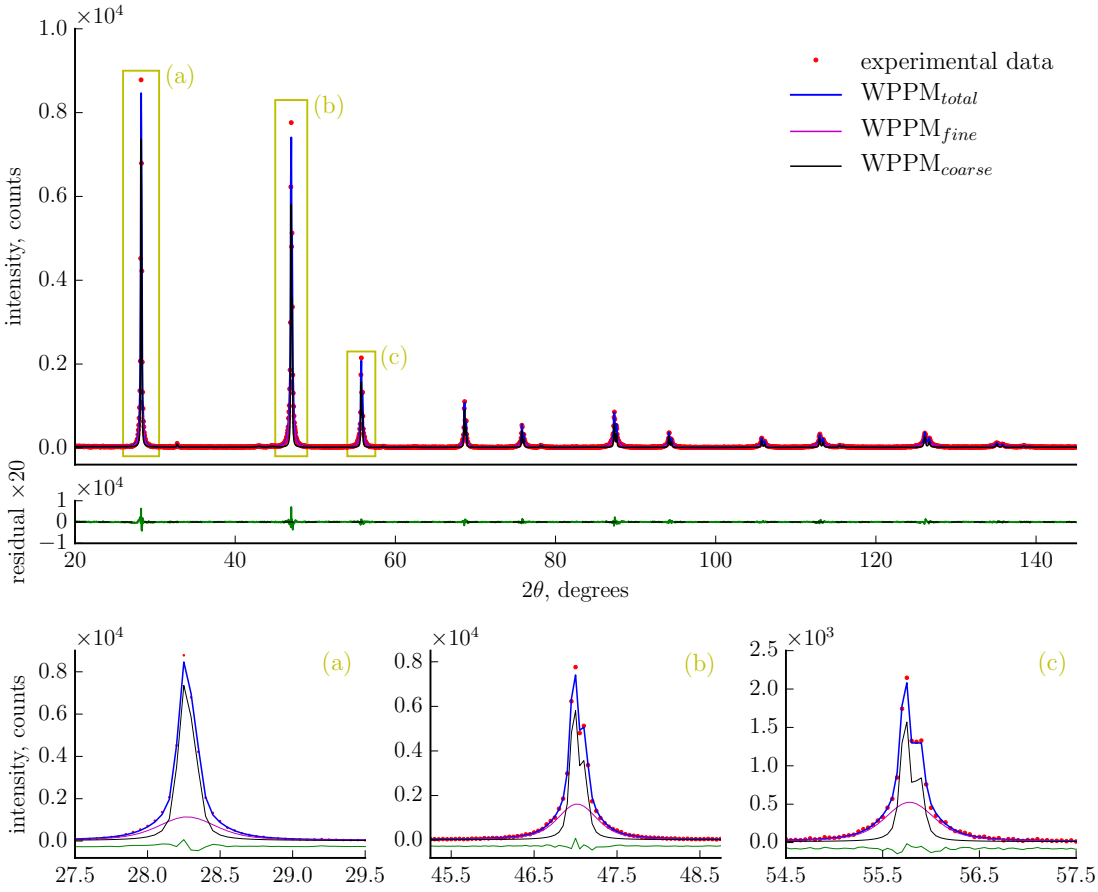

Figure 4.20: XRPD pattern of CaF_2 ball-milled in the Half-Moon (HM) jar for 32h and with jar-to-plate velocity ratio $\omega/\Omega + 1$ = -3.8. Experimental data (red circle) are shown together with the WPPM profile (blue line) and their difference (residual, green line below). The contribution of a coarse-grained (black line) and a fine-grained (purple line) fluorite fraction to the model is also accentuated in the insets (a, b, c).

Abstract

This article contains data and supporting information of and complementary to the research article entitled *Effect of jar shape on high-energy planetary ball milling efficiency: simulations and experiments* [92]. Calcium fluoride (CaF_2) was ground using two jars of different shape (cylindrical and half-moon) installed on a planetary ball-mill, exploring different operating conditions (jar-to-plate angular velocity ratio and milling time). Scanning Electron Microscopy (SEM) images and X-Ray Powder Diffraction data (XRPD) were collected to assess the effect of milling conditions on the end-product crystallite size. Due

to the inhomogeneity of the end product, the Whole Powder Pattern Model (WPPM, [140]) analysis of XRPD data required the hypothesis of a bimodal distribution of sizes - respectively ground (fine fraction) and less-to-not ground (coarse fraction) - confirmed by SEM images and suggested by previous literature [187, 188]. Predominance of fine fraction clearly indicates optimal milling conditions.

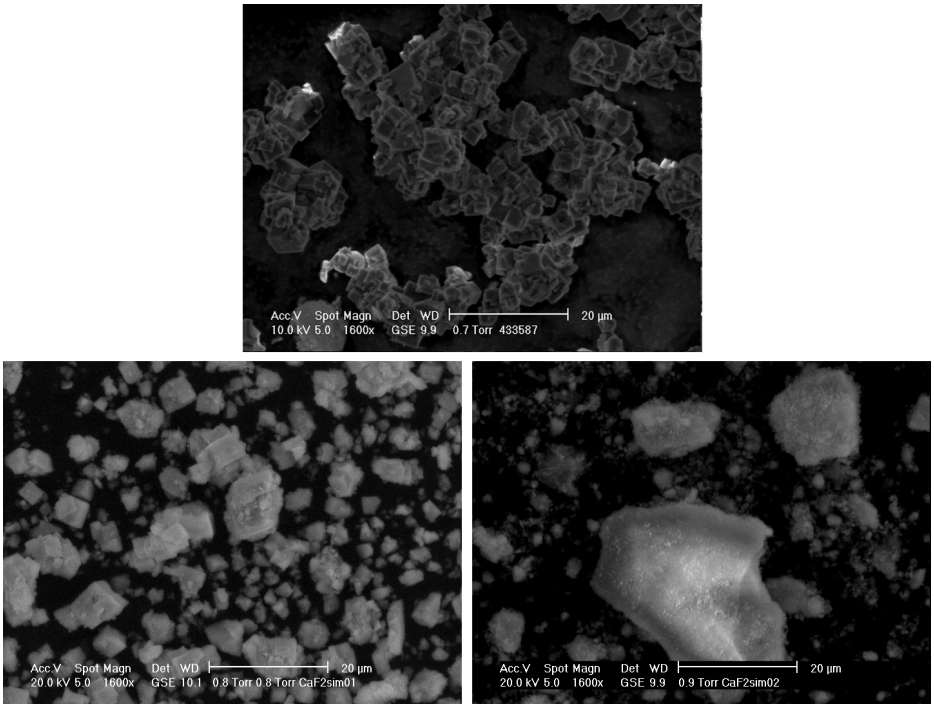

Figure 4.21: SEM micrographs of pristine powder (top) ball-milled with the cylindrical (CY, bottom left) and half-moon (HM, bottom right) jars for 8 hours and with velocity ratio of $\omega/\Omega + 1 =$ -1.0.

Value of the data

- The planetary ball-milling process is ubiquitous in the production of nanostructured materials and modification of their properties. The choice of optimal operating conditions defines end product characteristics. Data reported in this manuscript guide the understanding of the effect of two milling parameters (jar-to-plate angular velocity ratio and milling time) on the dimensional characteristics of the end product.

- The assessment of the milling behaviour (*e.g.* coexistence of fine and coarse fractions and their distributions) of a new jar design and the comparison with the standard cylindrical one can be drawn from reported data and clearly show the importance of the vial shape on the end product properties and on comminution efficiency.

Data

Data here reported aim at shedding some light on the effect of the milling process in terms of mill charge comminution.
During grinding, fluorite pristine powder, exhibiting crystallite sizes of approximately a few hundreds of nm, undergoes a overall size reduction but, as already pointed out in [92], depending on operating conditions, the end product could be not homogeneous. Under scarcely efficient conditions in particular,

the ground powder tends to develop a bimodal distribution of sizes, with a more or less pronounced fraction of powder ground to nanometer scale (fine fraction) coexisting with a second fraction of less or totally not ground fluorite crystals (coarse fraction). This is shown by the WPPM analyses, requiring two lognormal distributions of crystalline domains, describing respectively the coarse and the fine fractions, for the optimal modelling of XRPD data, as illustrated in figure 4.20.
The validity of this hypothesis is further demonstrated by SEM pictures (selected cases reported in figure 4.21), clearly showing the coexistence of grains characterised by considerably different sizes.

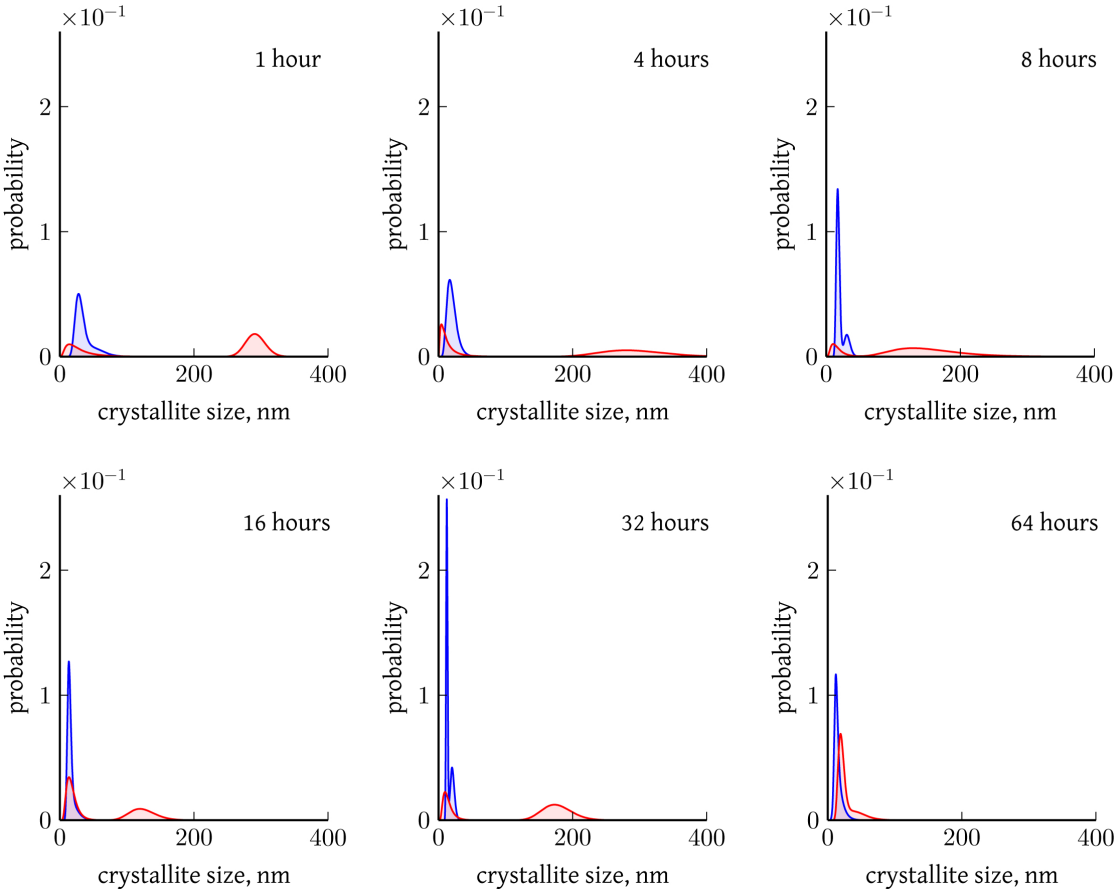

Figure 4.22: Crystallite domain size probability distribution for CaF_2 ground with the CY (red) and HM (blue) jars for increasing milling time and at $\omega/\Omega + 1$ = -1.0. Two lognormal size distributions, representing respectively the finer and the coarser (less or totally not ground crystals) fractions of the end product, were required to properly model XRPD data. The powder homogeneity increases with milling time and strongly depends on the vial shape, the HM jar being more effective and faster in producing a more uniform sample.

The lack of homogeneity of the end product can be significantly reduced by carefully tailoring the process and, in particular, a more uniform fluorite powder exhibiting nanometric crystalline domains, was produced by increasing the milling time [138, 187]. However, the amount of time required to reach this result closely relates on the jar design and the HM jar was revealed to be much more effective and faster, as illustrated in figure 4.22 comparing end product size distributions obtained by the WPPM analyses of patterns from samples milled with the CY and the HM jars for different milling times. SEM micrographs in figure 4.21 support this results. Indeed, cubic particles typical of the pristine material (figure 4.21,top) are still clearly recognizable in the end product of the CY jar (figure 4.21, bottom left) while

almost absent after milling with the HM vial (figure 4.21, bottom right), demonstrating the enhanced comminution efficiency of the HM jar under the adopted operating conditions (8 hours, $\omega/\Omega + 1 =$ -1). Also the creation of agglomerates covered by a large amount of fine particulate (below one micron) can be observed for the latter jar shape.

Experimental Design, Materials and Methods

Materials Calcium fluoride from CARLO ERBA Reagents S.r.l..

Milling Samples were milled in a Fritsch Pulverisette 4 (P4 [109]) planetary ball-mill under different operative conditions (jar-to-plate angular velocity ratio and milling time). Twelve balls were inserted in a cylindrical and in a half-moon jar (physical and geometrical properties reported in [91, 92]), designed by the authors and produced at the University of Trento (Italy).

Data acquisition A ESEM FEI XL 30 was employed to acquire SEM images while XRPD data were collected using a Rigaku PMG/VH diffractometer according to the procedure reported in [92, 138].

XRPD data analysis WPPM analyses [140] were performed using the software PM2K [176] and details are reported in [92].

Chapter 5

Some relevant case studies

While in chapter 4 the multibody dynamics model of the planetary ball mill (introduced in chapter 3) was employed to investigate the effect of the jar shape on the milling performance, in this chapter two case studies requiring different mechanical actions – *i.e.* mostly along the collision axis and perpendicular to it – are discussed.
In particular, a strategy for the optimisation of milling parameters for (i) the production of two-dimensional materials by exfoliation – mostly requiring tangential action – and (ii) the size-reduction – or comminution, especially requiring normal action – of the anti-HIV drug Efavirenz aimed at improving its dissolution properties, are tackled through the proposed modelling approach.

5.1 Planetary ball milling for the production of 2D nanostructured materials

The mechanical exfoliation of 3D-bulk systems leading to the production of 2D-nanostructured materials has been demonstrated to mainly require shear actions [15, 154, 189]. Among the possible approaches, the planetary ball milling is one of the most suitable top-down techniques being able to transfer a larger amount of energy in tangential direction than other grinding methods [15, 152, 190]. Simulations are here employed to investigate mill configurations maximising tangential mechanical action, particularly focusing on the effect of the number of balls and the jar-to-plate velocity ratio. The material considered in this example is graphite, characterised by extremely low friction coefficients, allowing to speculate also on the influence of this variable on the modelling results.
It should be pointed out that, while the case study of the milling of the Efavirenz is discussed in more detail and complemented with experimental data, the present discussion is only aimed at providing some hints and a possible optimisation procedure but further investigations would be required.

5.1.1 Introduction

In the last decades, two-dimensional (2D) materials such as graphene and boron nitride nanosheets, triggered intensive research worldwide [191, 192] due to their intriguing electrical [193], thermal [194], optical [195], magnetic [196] and mechanical [197] properties.
In particular, since the report of the first graphene layer isolated from graphite [198], this material – either as a single layer or as an aggregate of a few layers – has been proposed and investigated for a wide range of potential applications, ranging from energy production and storage to electronic industry, as well as to materials engineering *e.g.* to create nanocomposites [152, 192, 199, 200].
Graphene was first obtained by mechanical cleavage using Scotch tape [198], a technique still often used in laboratories since it provides high-quality samples [154]. However, the yield of this method is very low, excellent for lab-scale but certainly not sufficient for the development of graphene-based technologies,

requiring a large-scale and low-cost production method [154, 199, 201].
Literature provides several alternatives fulfilling this request, either following a bottom-up or a top-down route [152, 189, 192, 202]. While the former category mainly includes chemical methods, such as vapor deposition, epitaxial growth or solvothermal synthesis [203–205], the latter consists in the exfoliation of 3D bulk graphite, mostly *via* sonication or by mechanical action [206–208]. Ball milling – which falls into the second class of methods – is often employed (see *e.g.* [152, 189, 190, 199, 201, 202, 209, 210]) due to the low operational cost and the possibility of processing a relatively large amount of material. Among the various ball mill apparatuses, the planetary one demonstrated the highest attitude [152, 154] generally being able to transfer a larger amount of shear action with respect to the other devices. Indeed, the process efficiency was shown to be strongly influenced by the shock or shear nature of the impulsive stress transferred by the impacts [15, 211–213]. A prevalence of intense shock loads was noticed to mostly destroy or disorder the graphite in-plane crystal structure even leading to amorphous phases [15, 154, 189, 214]. On the contrary, graphene sheets exhibiting low defect content and well preserved crystal structure were obtained with a dominant shear component of stresses [15, 154, 189, 214]. The proficiency of the shear action was further confirmed by the high quality end product obtained by Antisari [15], introducing a newly designed milling device, exploiting the sliding between a rotating pestle and jar to transfer pure shear to the mill charge. Anyway, this milling condition can be approximately reproduced by a planetary ball mill by carefully tailoring the milling parameters so to control the arising balls motion mode [154, 189, 215]. Among the works highlighting the fundamental role of parameters assessment in maximising exfoliation efficiency, the one of Deepika [215], presenting an experimental systematic investigation on the effect of milling time, filling ratio, mill velocities and balls size on the production of boron-nitride nanosheets should certainly be mentioned.
As a possible process optimisation procedure, alternative to experiments, the application of multibody dynamics computer simulations is here proposed for the case study of the milling of graphite. This method provides insights on the milling dynamics, therefore allowing to speculate on configurations mainly transferring energy in tangential direction and reducing or even avoiding violent impacts.

5.1.2 Methods

The multibody dynamics model presented in chapter 3 is employed here to simulate the milling of graphite. Steel jar and balls exhibiting the previously listed geometrical and physical characteristics (see table 4.2) are adopted and therefore the contact model parameters reported in table 3.2 are applied.
Also in this case the powder charge is not explicitly modelled, but its effect is simulated through suitable friction parameters and both the (i) steel-steel and (ii) steel-graphite interaction cases are investigated, as experimental grinding is expected to fall in-between them. It is worth underlying that the latter (ii) case is characterised by extremely low friction and, as suggested by literature [216, 217], $\mu_s = 0.1$ and $\mu_d = 0.08$ are adopted in the Coulomb friction scheme (MSC.Adams formulation, see chapter 3).
Integrator parameters reported in subsection 3.2.1 are maintained and simulation time equals 24 seconds. The effect of the number of balls (6, 12, 24) and jar-to-plate velocity ratio ($\omega/\Omega + 1$ ranging from 0.0 to -3.4) are investigated and simulations results are analysed in terms of average SE, probability distribution of impact velocities and balls trajectories.

5.1.3 Results

Figure 5.1 reports the average SE computed from simulations as a function of jar-to-plate velocity ratio ($\omega/\Omega + 1$), both for the steel-steel (green) and the steel-graphite (red) interactions and for an increasing number of balls inside the jar. In particular, for the steel-steel case this quantity exhibits a maximum shifting towards less negative velocity ratios while increasing the number of balls. As already pointed out

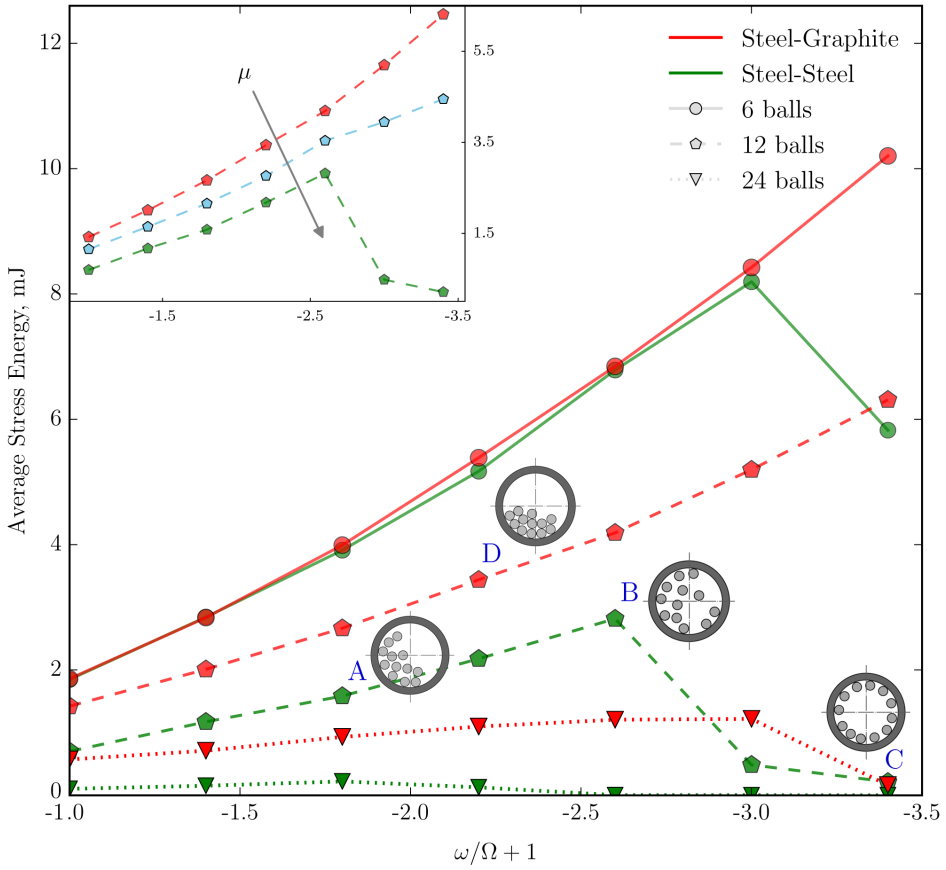

Figure 5.1: Average SE for the steel-steel (green) and the steel-graphite (red) interactions as a function of number of balls (6, 12, 24) and $\omega/\Omega + 1$. Typical balls trajectories are also sketched. The inset reports the average SE computed for 12 spheres for the steel-steel, the steel-fluorite (lightblue) and the steel-graphite cases, highlighting the effect of the lowering of friction ($\mu_d = 0.8, 0.2, 0.08$ respectively).

in the previous chapters (where simulations were performed with 12 balls), the average SE is proportional to balls motion complexity, with cascading (a), cataracting (b) and rolling (c) regimes arising by varying $\omega/\Omega + 1$ as sketched in figure 5.1. Particularly, cataracting regime, providing with the maximum SE, shows the most disordered balls movements and the larger number of high velocity impacts, as can be deduced by comparing the a, b and c cases of figure 5.2, reporting the trajectories of 12 spheres and the corresponding probability distributions of normal and tangential components of contact relative velocity, transferring respectively shock and shear actions. According to the above-mentioned literature the cataracting regime, giving to the most complex motion, should be the worst for graphene production, probably damaging its atomic structure [15, 154, 189, 214].

Looking at the steel-graphite case, the average SE computed with 6 and 12 balls does not demonstrate a maximum – or, in other words, a modification of the motion regime depending on the velocity ratio – and this can be related to the very low friction parameters characterising this interaction. Indeed, the inset of figure 5.1 reporting the average SE computed for steel-steel, steel-fluorite and steel-graphite interactions

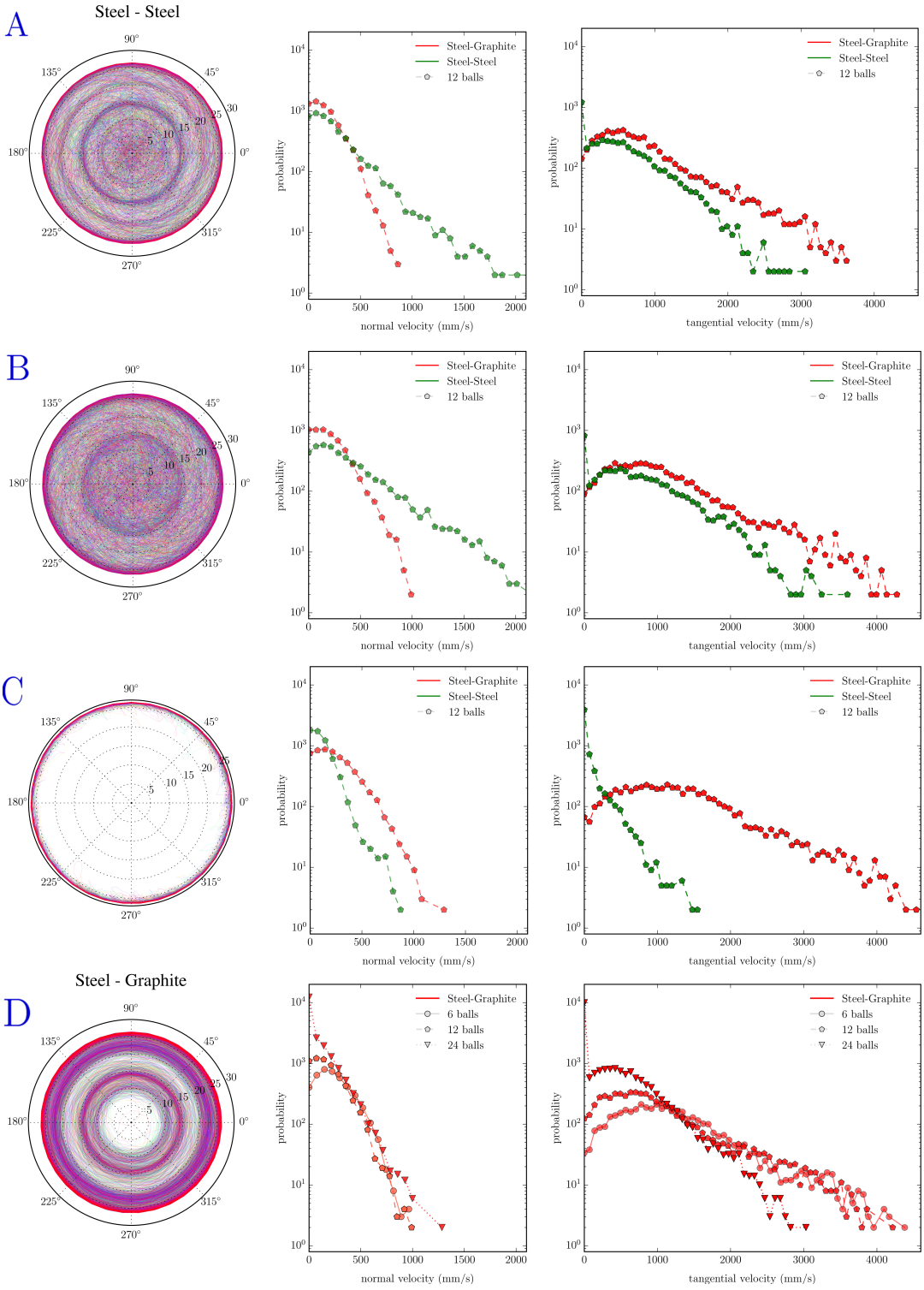

Figure 5.2: Selected trajectories and probability distributions of relative contact velocities for the steel-steel (green) and steel-graphite (red) interactions corresponding to the velocity ratios sketched and indicated with a,b,c,d in figure 5.1. The normal and tangential velocities components are presented in a,b,c for the two simulated interactions, whereas d highlights the effect of the different number of balls for the steel-graphite case.

(respectively characterised by $\mu_d = 0.8, 0.2, 0.08$) shows that the lowering of friction shifts the maximum of the SE to more negative values, till the limit of curves being monotonically increasing.
In terms of motion regime, for all the $\omega/\Omega + 1$ the reduced friction leads milling media to cluster and slide along the vial surface (d). Consequently, the balls crossing the jar and colliding at high velocity are only a small fraction, or even none, as shown by trajectories in figure 5.2d. This implies a normal component of contact relative velocities much lower than in the steel-steel case but, most importantly, a noticeably larger tangential one (see figure 5.2,a,b,c), resulting in a higher exchange of shear actions, as required for best exfoliation of graphite [15, 154, 189, 214]. However this applies until the number of balls is sufficiently low. In fact, interactions among balls generally increase with their number, therefore promoting the detachment from the jar surface, causing a modification of the motion regime also for the steel-graphite pair as suggested by the 24 spheres curve of figure 5.1. Consequently, an increase in the normal relative velocity component and a decrease in the tangential one can be observed (see figure 5.2,d).
Recalling that real grinding is expected to fall in-between the steel-steel and steel-graphite boundary interactions, the analyses here reported suggest that milling configurations providing with the higher shear action exchange are likely to require a relatively reduced jar filling ratio. Furthermore, in terms of jar and plate velocities, either the lowest or the highest ratios (*i.e.* sufficiently far from the maxima of SE curves) seem to be more favourable. However, being the magnitude of the average available SE a function of $\omega/\Omega + 1$, correlations with experimental results would be necessary to assess the condition leading to the most efficient graphene sheets production. Experiments would also provide a validation of simulations results, allowing to further exploit the modelling for predicting the effect of the other milling variables.

5.2 Planetary ball milling of the Anti-HIV drug Efavirenz

In this section, the processing of the Anti-HIV drug Efavirenz in the planetary ball mill is investigated. In terms of required mechanical action, this problem is opposite to the exfoliation of graphite since, as will be better explained, normal forces and low energy are fundamental to achieve the goal of enhancing the dissolution properties of this organic compound. Furthermore, differently from the previously presented cases, not steel but rather zirconium oxide milling media are adopted so to avoid the contamination of the end product. Also the size of both jar and balls is different since samples consist of a smaller amount of powder.

5.2.1 Introduction

The latest report of the Joint United Nations Program on HIV/AIDS (UNIDAS) [218] estimates that until 2015 the number of people living with AIDS world-wide was about 36.7 million. However, from 2010 the access to anti-retroviral treatments has more than doubled (from 7.5 from 17.0 million people) and this is regarded to be largely responsible of a 26 % reduction of AIDS-related deaths. Greater financial and human investments are currently running both in clinical experience and research so to achieve the ambitious targets to extend the therapy coverage to at least the 90% of HIV-positive within 2020 and to end the epidemic by 2030 [218].
Among the mostly prescribed anti-retroviral drugs, Efavirenz (EFV) belongs to the class-II (low solubility, high permeability) under the Biopharmaceutics Classification System (BCS) [219], exhibiting poor aqueous solubility and low dissolution rate. This leads to limited drug bioavailability [†] (since these kinds of compounds tend to be eliminated by the body before the dissolution and absorption into the systemic

[†]Bioavailability of a drug is defined as the fraction of the administered dose of a drug that enters the systemic circulation, thereby accessing the site of action [220]

circulation processes are completed), requiring an increased dosage to achieve therapeutic levels in the body, often implying adverse effects for the patient [221–223].
Nowadays, almost the 70 % of newly developed drugs show low solubility and therefore the enhancement of dissolution is one of the most considerable challenges in pharmaceutical industry [222, 224, 225]. Several strategies have been adopted to overcome this limitation both involving chemical and physical modification of the compounds. While the former route implies the design of new polymorphs often followed by undesirable alterations of the biological effect, the latter keeps it unchanged, requiring consequently a smaller amount of *in vitro* and *in vivo* testing procedures. One of the most exploited physical method to enhance drug solubility, is particle size reduction [11, 226, 227]. This yields to the increase of the surface area in contact with the dissolution medium, S, which is proportional to the dissolution rate, $dC/\mathrm{d}t$, as stated by the Nernst-Brunner equation [228]

$$\frac{dC}{dt} = \frac{D\,S}{V\,h}(C_S - C), \tag{5.1}$$

where D is the diffusion coefficient, V the volume of the dissolution medium, h the thickness of the diffusion layer, C_s the saturation solubility and C the instantaneous concentration at time t.
Many technologies are available for the production of ultrafine particles [229, 230] and micronization has been for years the most widely used, employing in particular air jet mills (see *e.g.* [11, 223, 231]). However, nowadays many pharmaceuticals are so poorly soluble that going down to the nanorange is essential to affect dissolution and, for this task, planetary ball mills are frequently adopted [11–14].
Apart from size reduction, milling induces many other alterations of the drug particles (*e.g.* shape, roughness, structural disorder and defect content) that have a considerable impact on dissolution, as revealed by some literature works [11, 222, 232, 233]. Therefore, to completely understand the phenomenon, the connections not only with particle size but also with many other parameters should be investigated. With this in mind, a recent study proposes the analysis of the effect of drug microstructural properties on the biopharmaceutical performance [139]. These properties, very often exploited in Materials Science to explain the behaviour of materials like ceramics and metals, are not properly considered in the pharmaceutical science [139]. Nevertheless, the above-mentioned work, focusing on crystallite domains, evidenced this quantity to better correlate with dissolution than particle size [†] for the EFV produced by micronization (raw material). Indeed, smaller crystalline domain sizes were found to correspond to higher dissolution values also for batches with comparable particle sizes.
In the study here proposed, at the aim of enhance the dissolution rate, the EFV raw material is ground in the planetary ball mill and the crystallite domain size is adopted as a parameter to compare the effect of the milling process performed under different conditions. Since the end-product characteristics strongly relate to milling parameters, as already shown in previous chapters, the application of the planetary ball mill multibody dynamics model, supported also by camera recordings of the process, was crucial to quickly predict the mill configuration providing with the larger reduction of crystallite size, possibly leading to the higher dissolution.

5.2.2 Methods

EFV raw material, produced by micronization, was kindly donated by the Brazilian governmental pharmaceutical laboratory Farmanguinhos-FIOCRUZ.
Unlike the previous examples reported in this thesis, for processing the EFV in the P4 planetary ball mill, zirconium oxide (or zirconia) balls and jar were used. This material was chosen since it offers at

[†]Particles are localized objects exhibiting well-defined contours; crystallite domains constitute the internal structure of each particle and are regions coherently scattering. See section 3.2 for more detailed informations.

the same time high grinding efficiency (due to the high density) and great wear resistance, satisfying the requirement of preventing sample contamination, fundamental for the milling of a pharmaceutical.
Experiments were performed adopting a 45 ml volume jar (whereas in the previous case studies it was 80 ml), filled with 20 balls of 3 mm diameter and 800 mg of EFV powder. The complete set of geometrical and physical properties of milling media is reported in table 5.1. Different plate velocities and jar-to-plate velocity ratios were tested through both computer simulations and experiments.

Jar and Spheres (Zirconium Oxide)	
jar radius	20mm
jar volume	45cm^3
jar height	40mm
spheres radius	3mm
density	5.7 g/cm^3
Young modulus	205GPa
Poisson ratio	0.23

Table 5.1: Geometrical and physical properties of jar and milling media for the case study of EFV grinding.

The model

The multibody dynamics model was built following the procedure explained in section 3.2 but, being materials and dimensions of milling body different from previous examples, both the geometry and the contact laws were redesigned.
Contact and friction schemes coefficients as well as integrator parameters (HHT integrator, $h_{max} = 10^{-6}$, error $= 10^{-6}$, *step* $= 200$/sec) were estimated according to the method defined in section 2.1. Also in this case the mill charge was not explicitly modelled but accounted for through the friction coefficients. All the values of parameters adopted for the for the zirconia-zirconia and zirconia-EFV interactions, resulting from the experiments reported in subsection 2.1.1 can be found in table 5.2.
Simulations lasting 24 seconds were performed for both cases and results in terms of relative velocity were exploited to compute the average stress energy (equation 3.10). Trajectories of balls were also investigated and compared with camera recordings.

Camera recordings

The motion of the balls was monitored *in operando*, both with and without the EFV mill charge, by installing the equipment described in subsection 4.1.1. Camera recordings allowed a qualitative comprehension of balls movements and their dependence on milling parameters set up.

XRPD-LPA

The XRPD patterns of EFV reported in the following section were recorded by a Thermo-ARL XTRA diffractometer with MoKa radiation generated at 50 kV and 40 mA, with a scanning rate of 0.4°/min over the 1.5-12° 2θ range. Measurements were performed in Bragg-Brentano geometry.
The analysis of each powder pattern under the WPPM approach [140–142], provided with the corresponding Full Width at Half Maximum (FWHM) which is inversely proportional to the size of the crystalline domains (for more information see section 3.2 and *e.g.* [234]).

Contact model parameters		
sphere-sphere generalized contact stiffness, k_{ss}	176,730N/mm$^{3/2}$	eq.3.3
sphere-plane generalized contact stiffness, k_{sp}	249,935N/mm$^{3/2}$	eq.3.4
restitution coefficient, e	0.9	drop test, $e = \sqrt{h^*/h_0}$
relative impact velocity, $\dot{u}_{n0}$	3,3mm/s	statistical analysis of velocities
sphere-sphere contact damping, $c_{m,ss}$	0.33kg/s	eq.3.5
sphere-plane contact damping, $c_{m,sp}$	0.57kg/s	eq.3.5
full damping penetration depth, d	0.114mm	fit of experimental drop test results
Friction parameters		
static friction, zirconia-zirconia μ_s	0.8	literature
dynamic friction, zirconia-zirconia μ_d	0.67	tribological test
static friction, zirconia-EFV μ_s	0.48	literature
dynamic friction, zirconia-EFV μ_d	0.4	tribological test
stiction transition velocity, v_s	1mm/s	statistical analysis of velocities
friction transition velocity, v_d	10mm/s	statistical analysis of velocities

Table 5.2: Values used for the contact and the friction models and method used for their derivation.

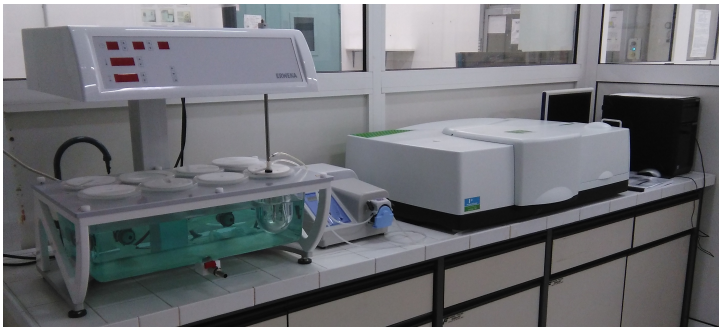

Figure 5.3: The apparatuses for dissolution testing: the dissolutor (on the left) and the spectrophotometer (on the right)

Dissolution Tests

In vitro dissolution tests are used in pharmaceutical industry as a surrogate of *in vivo* human studies to assess the release properties of the drugs so to predict required oral dosage and *in vivo* bioavailability [235–237].
Tests are performed in a dissolutor, an apparatus made of a transparent vessel and a rotating paddle (USP Apparatus 2 [236, 238], see figure 5.3). The vessel contains a liquid (the dissolution medium), kept at constant human-body temperature (*i.e.* approximately 37° C), and the drug sample in granular (powder) or tablet form. For the tests here presented, an Erweka DT-626 dissolutor was used, with the paddle rotating at 50 rpm and the vessel filled with 900 mL of methanol solution (40% V/V) at 37° C ± 0.5° C and 0.1 g of ground EFV. The drug release in the dissolution medium was real-time measured by an UV-VIS Spectrophotometer (Perkin Elmer Lambda 650, wavelength 248 nm wavelength) connected by a 40 μm cannula filter to the dissolutor (see figure 5.3), allowing to collect and analyse samples in continuous [232, 233].

5.2.3 Results †

A first series of preliminary experimental tests was performed by milling the EFV for 30 minutes under conditions typical for ceramics materials and metals, namely Ω=200rpm and $\omega/\Omega + 1$ between -1 and -3.4. However, XRPD-LPA on the end-products, revealed that the process did not have any effect on crystallite domain size. Indeed, as reported in figure 5.4 top-left for $\omega/\Omega + 1$ = -1 and -3.4, with respect

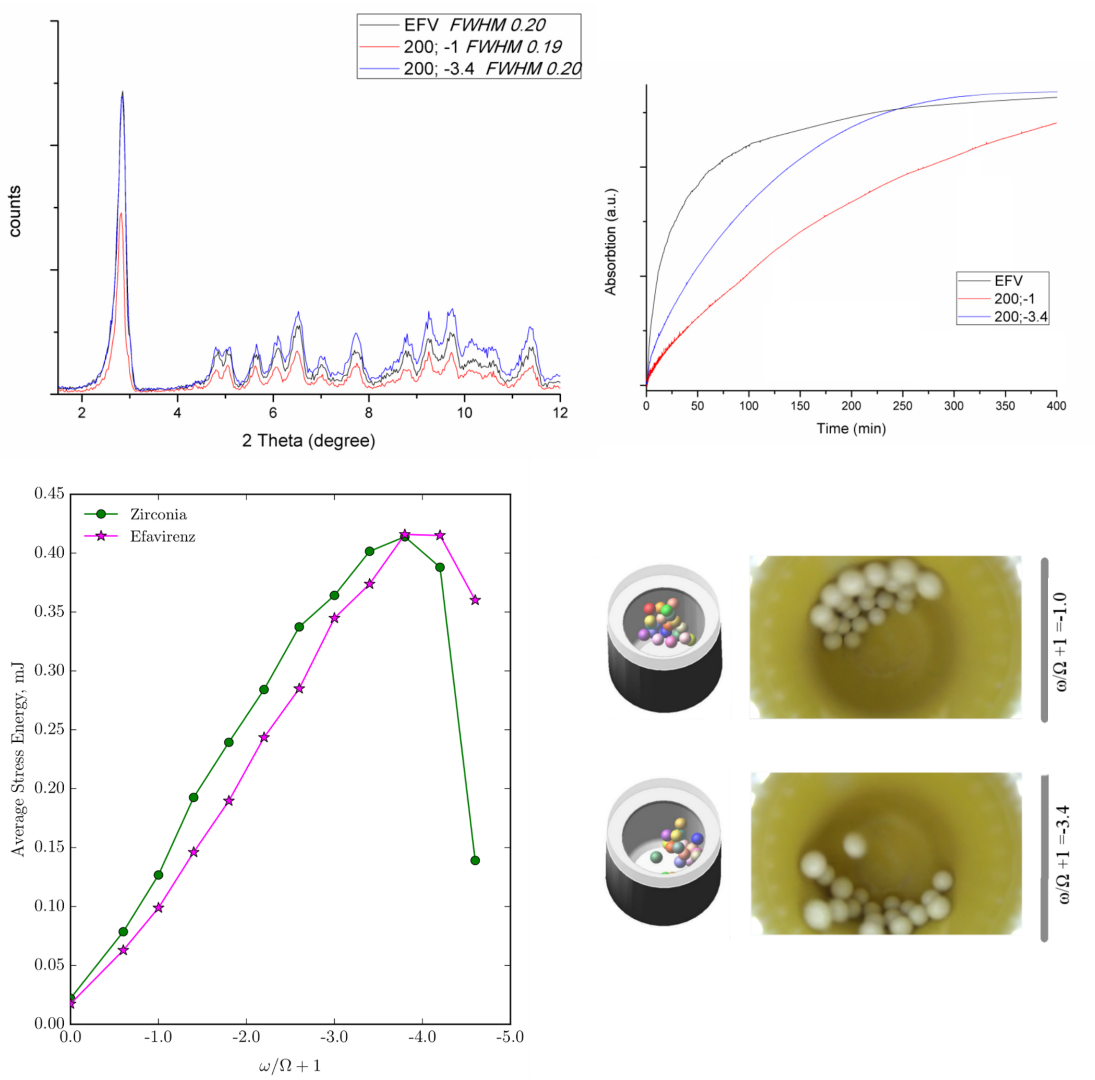

Figure 5.4: Results of milling of Efavirenz with Ω=200rpm and $\omega/\Omega + 1$ = -1 and -3.4. Top-left, XRPD-LPA patterns; top-right, dissolution tests; bottom left, *average stress energy* computed from simulations; bottom-right, simulated and recorded images of the milling process for the two tested velocity ratios.

to the raw material (black line) no broadening of the peaks can be observed for the ground samples and the FWHM is almost unaltered. Moreover, for longer milling time, the works [232] and [233] showed this conditions to be too energetic, to the point of causing the recrystallization of the material, leading

†In this work I carried out the simulations, the *in operando* camera recordings and part of the experimental milling. The major part of the experimental milling, the XRPD measures together with the LPA were executed by E. Cappelletto and M. D'Incau. Dissolution test were performed by E. Cappelletto. XRPD patterns and dissolution profiles reported in the figures of this section are courtesy of E. Cappelletto and M. D'Incau.

to morphology alterations. Also in terms of dissolution, no improvement but rather a worsening with respect to the raw material, was given by the milled samples, as reported in figure 5.4 top-right.
So to investigate the reasons of ineffectiveness of the adopted milling process configuration, the application of multibody dynamics simulation and *in operando* video recording was helpful. In fact, results of simulations performed under the same milling conditions of the above-mentioned experiments and presented in figure 5.4, bottom right, showed that, due to the high velocities, the balls tend to gather together and stick along the height of the jar. The group of spheres rolls and slides over the powder, also covering the jar surface but, in contrast with the exfoliation process, this kind of motion is not effective in comminution, since this process seems to especially require the transfer of forces in normal direction [91, 92]. Prevalence of rolling motion was found to arise (both from camera recordings and trajectories of balls in simulations) for every tested velocity ratio. Nevertheless, the average Stress Energy (SE) computed from simulations (see figure 5.4,bottom right) shows a trend but this is due to the sporadic detachment of some balls at the highest velocity ratios, resulting in a larger number of high velocity impacts and, in turn, augmented average energy.

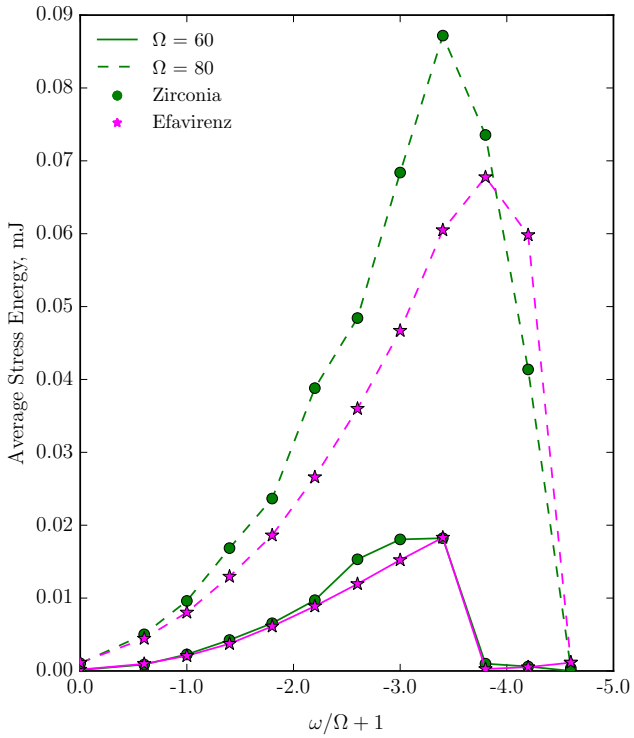

Figure 5.5: Average stress energy for zirconia-zirconia and zirconia-EFV interactions as a function of the jar to plate angular velocities, computed from simulations performed at Ω= 60 (solid line) and 80rpm (dashed line). For both the plate velocities and interactions, the location of the maximum is comprised approximately between $\omega/\Omega + 1$=-3.0 and -3.8.

Giving useful support in the comprehension of the milling process, both the model and camera recordings were further exploited to setup more suitable milling conditions, possibly leading to effective crystallite size reduction, shown to be one of the parameters influencing the dissolution enhancement [139].
As a first step, energy reduction was pursued in order to avoid the side effects evidenced in [232, 233] and, referring to the previously reported results (see chapters 3 and 4) highlighting the dependence of this quantity on plate angular velocity, Ω was reduced. Ω = 60rpm and Ω = 80rpm were tested and, both for the zirconium-zirconium and zirconium-EFV interactions, simulations were performed varying

the $\omega/\Omega + 1$ velocity ratio between 0 and -4.6. Besides a global remarkable reduction of the magnitude of the average SE with respect to Ω = 200rpm, figure 5.5 shows the maximum of this quantity to be comprised between approximately $\omega/\Omega + 1$=-3.0 and -3.8 for both the tested Ω.
Furthermore, it can be noted that the $\omega/\Omega+1$ maximum location keeps almost the same for the zirconium-zirconium and the zirconium-EFV interactions since friction characteristics, pointed out by the tribological tests, are very similar.

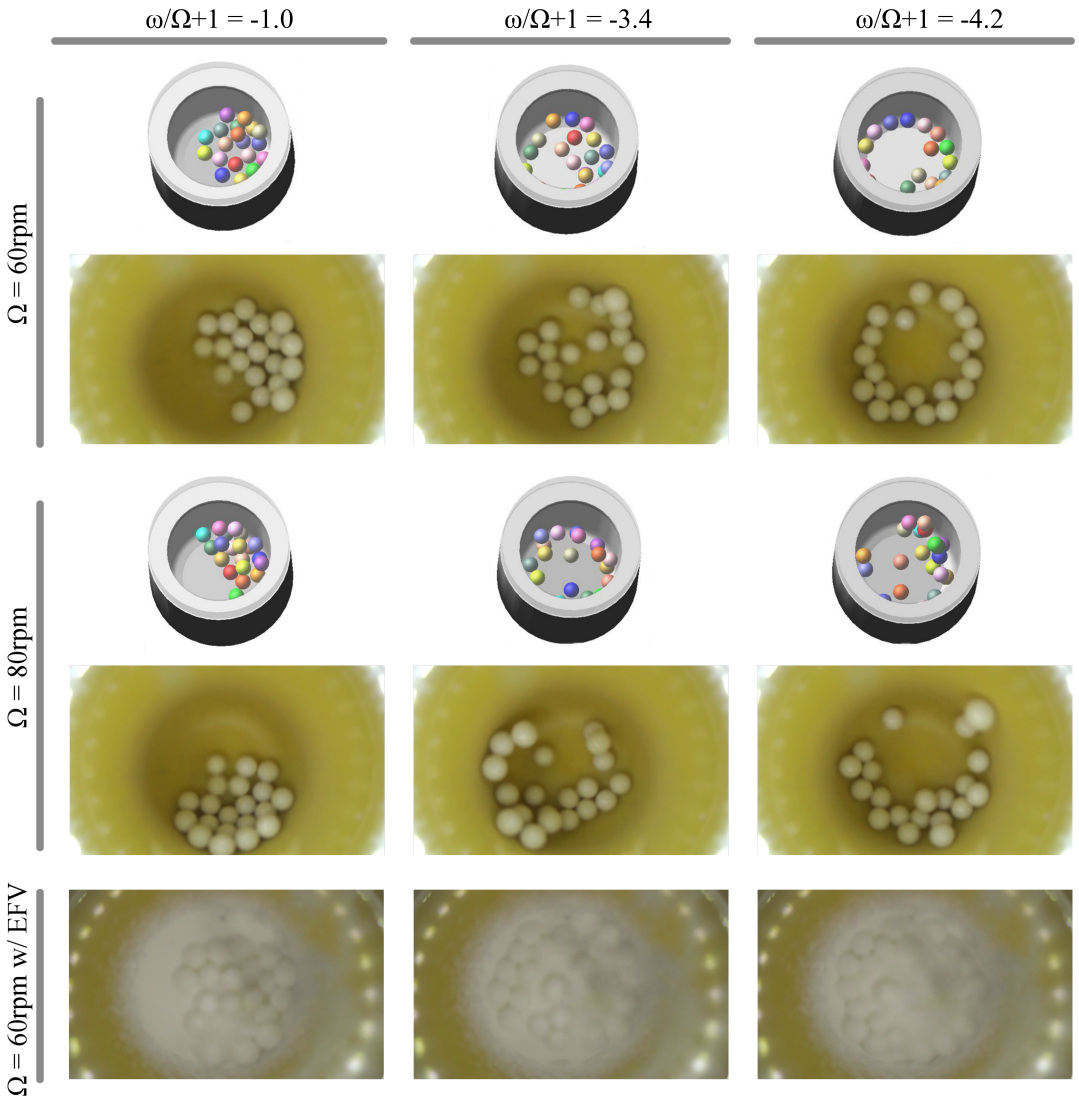

Figure 5.6: Top and middle, comparison of camera and simulated images of milling media motion inside the jar for, respectively, Ω = 60 and 80 rpm and $\omega/\Omega+1$=-1.0 (left), -3.4 (center) and -4.2 (right). The maximum disorder of the motion corresponds to $\omega/\Omega + 1$=-3.4. Bottom, camera images recorded with EFV powder inside the jar for Ω = 60rpm and under the above-mentioned velocity ratios. Balls can be seen to occupy the bottom part of the jar, therefore almost fully involving the powder in grinding.

According to the results presented for the fluorite case of study (see chapters 3 and 4), the $\omega/\Omega+1$ range of higher energy values should indicate the best milling condition for a material like EFV, requiring size reduction. Indeed, it was shown that the maximum energy corresponds to the higher disorder of balls motion, also providing with the larger amount of high normal velocity impacts, deemed as the more

effective in comminution [91, 92].
The maximum complexity of balls movements was confirmed to arise around $\omega/\Omega + 1$=-3.4 by visual inspection of balls trajectories both in simulations and camera recordings, as reported in figure 5.6, pointing out also a good agreement between images obtained from these two techniques. However, it should be underlined that, the three motion regimes (cascading, cataracting, rolling) clearly recognisable in the previous case studies, are not so markedly different for this mill configuration, probably due to jar and balls different geometry.
In addition, in contrast to the Ω=200rpm case, Ω=60 and 80rpm balls were revealed to move mainly in the lower part of the jar. In particular, camera images recorded with the EFV for Ω=60rpm and reported in figure 5.6 bottom, show balls to occupy the very bottom part of the jar, where also the powder lies. As a consequence, powder is much more involved in milling than in the other cases, in which it is mainly pushed along jar wall. Better comminution and higher end-product homogeneity were therefore expected for this Ω condition.
Driven by simulation predictions, EFV was ground for 30 minutes at $\omega/\Omega + 1$ = -1, -3.4, -4.2, with Ω=60 and 80rpm so to test three different conditions in terms of motion regime and energy. XRPD-LPA results, reported in figure 5.7, highlight that for Ω=60rpm (left part of figure 5.7) ω/Ω+1 = -3.4 provides with the maximum crystallite size reduction, as expected from simulations and camera investigations. This does not apply instead to Ω=80rpm (right part of figure 5.7), where smaller crystallites are produced under $\omega/\Omega + 1$ = -1.0. However, a similarity among these two conditions can be noticed in resulting FWHM (0.32 for $\omega/\Omega + 1$ = -3.4, Ω = 60rpm; 0.33 for $\omega/\Omega + 1$ = -1.0, Ω = 80rpm, see figure 5.7), amorphous component (apparently larger than for the other ratios, see figure 5.7) and even in terms of total amount of average SE (approximately around 0.01 mJ, see figure 5.5). This could suggest this value to represent a some kind of upper bound of energy efficiently involved in comminution and that the energy exceeding it could be involved in the development of other processes.

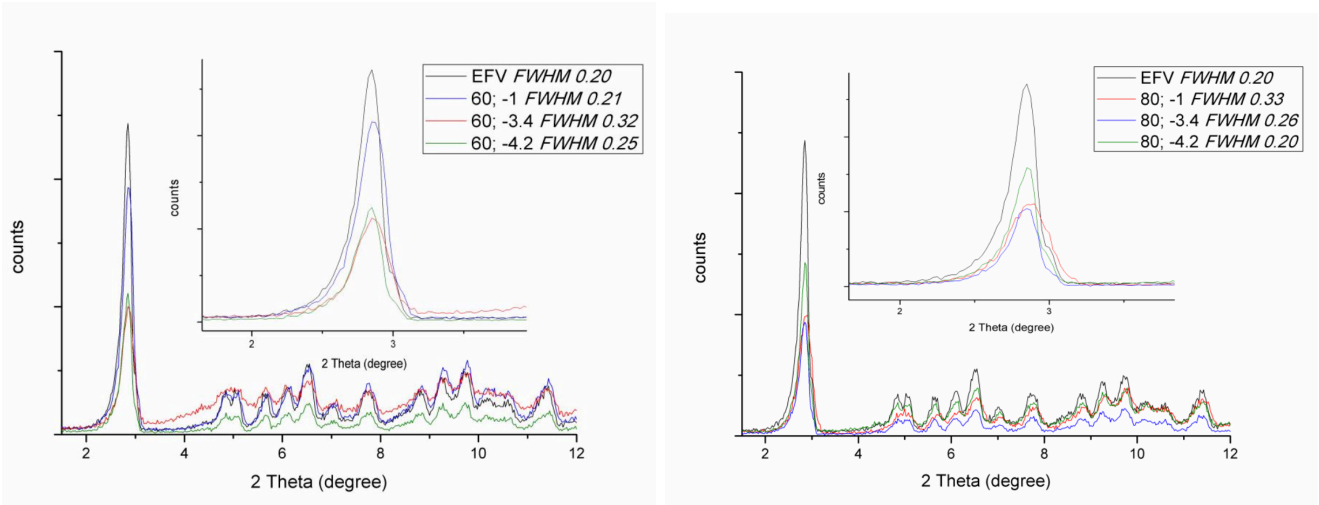

Figure 5.7: XRPD patterns of EFV milled at Ω= 60 (left) and 80rpm (right). For Ω= 60rpm, results of LPA indicates $\omega/\Omega + 1$=-3.4 to provide with the maximum broadening of the peaks and higher FWHM, namely with the smaller crystallite sizes. For Ω= 80rpm the same results is given by $\omega/\Omega + 1$=-1.0.

Figure 5.8 reports the dissolution profiles of the samples milled at $\omega/\Omega + 1$ = -3.4, with Ω = 60, 80, 200rpm and it clearly reveals both the Ω = 60 and 80rpm milling conditions to give an improvement of dissolution rate with respect to the raw material as well as Ω = 200rpm, supporting the previously highlighted request of energy reduction. In particular, the sample corresponding to the less energetic configuration (Ω = 60rpm) provides the best result, exhibiting an amount of dissolved drug larger than

the others at every instant of time. Furthermore, for these Ω conditions, a correlation between crystallite dimensions and dissolution can be supposed since the smaller the crystallites the higher is the dissolution.

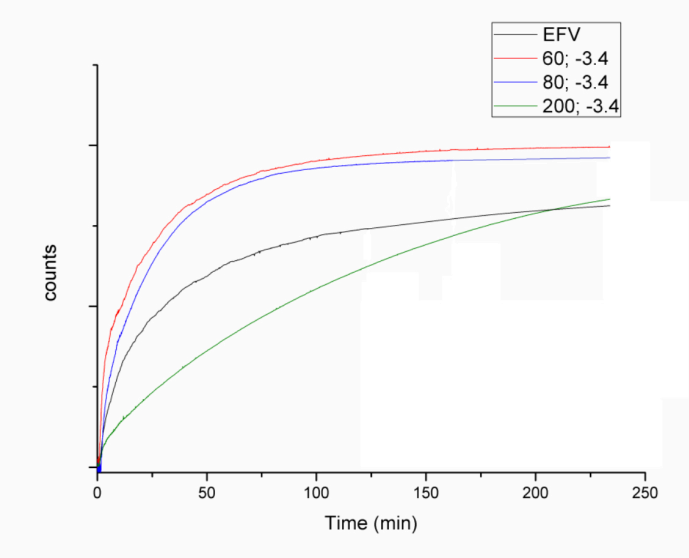

Figure 5.8: Dissolution profiles of EFV raw material and milled at $\omega/\Omega + 1$=-3.4, with Ω = 60, 80 and 200rpm. Samples produced with Ω = 60 and 80rpm give an improvement of dissolution rate with respect to the raw material and the Ω = 200rpm condition, thus validating the suggestion about efficient milling conditions provided by simulations.

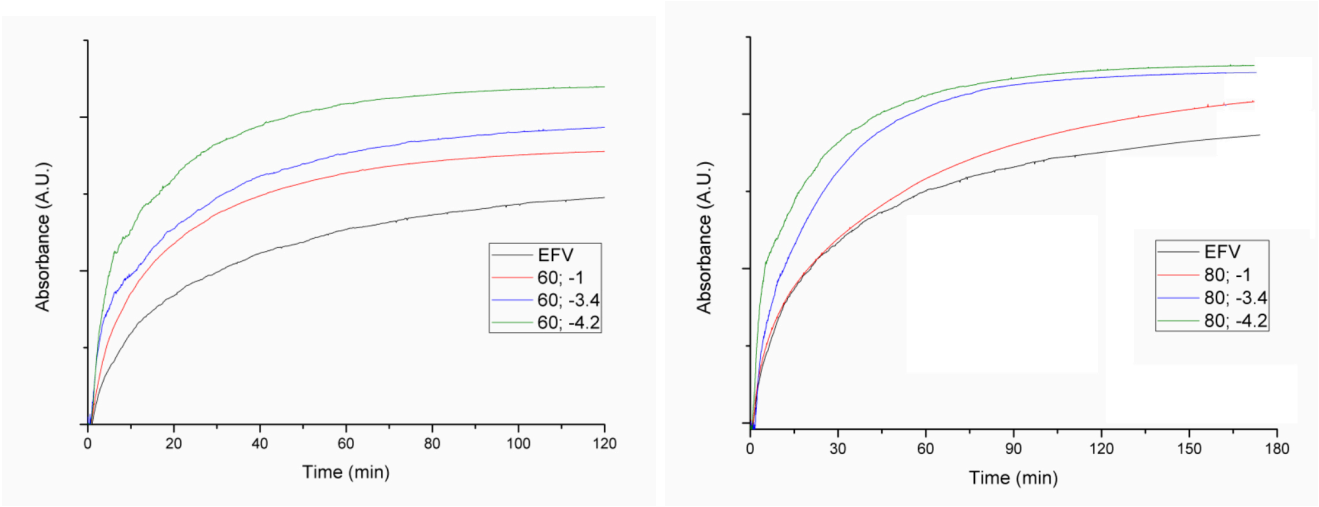

Figure 5.9: Dissolution profiles of EFV raw material and milled at $\omega/\Omega + 1$=-1.0, -3.4, -4.2, with Ω = 60 (left) and 80rpm (right). For both Ω, for all the tested velocity ratios an enhancement of dissolution rate with respect to raw material can be noticed and samples milled $\omega/\Omega + 1$= -4.2 are shown to give the best results.

The same can not be asserted, however, for the dissolution profiles of samples milled under the same Ω but at different velocity ratios. Indeed, as shown in figure 5.9, for both Ω = 60 and 80rpm, the dissolution is slightly higher for the samples ground at $\omega/\Omega + 1$ = -4.2, a ratio not among those indicated as most favourable by simulations and providing with larger crystallites than *e.g.* -3.4. This results, can relate to other effects of the milling process *e.g.* agglomeration of particles or alterations of morphology, not

investigated in this work but strongly influencing the dissolution mechanisms [232, 233]. It can therefore be concluded that, the modelling of the process together with the *in operando* recordings, allowed a better understanding of the milling process dynamics and provided suggestions to move towards in the setup of milling conditions leading to an efficient reduction of crystallite size and an enhancement of EFV dissolution. However, dissolution is a complex phenomenon and further analyses, also going beyond the milling process, are required for its full comprehension.

Chapter 6

Conclusions

The main focus of this Thesis has been the development of a numerical model of the planetary ball mill, one of the most flexible and widely employed high-energy grinding devices. This multibody dynamics model, typically corroborated by a structural and microstructural characterisation of the ground mill charge, has been exploited to investigate and tune several milling variables, which define operating conditions that determine the characteristics of the end product. Simulations outcomes – consisting in the kinematic and dynamic quantities at each timestep – shed light on several fundamental aspects of the process *e.g.* balls motion regimes and collision velocities, in turn related to the available power and the preferential direction of impact energy exchange with respect to the collision axis (normal-to-tangential ratio).

When compared to typical experimental characterisation of the milling result, this numerical tool reduces the effort – as well as the cost – of parameters assessment and provide quantities *e.g.* contact forces which are not accessible by experiments. The validity of the model has been successfully assessed (i) against a size-strain analysis – in terms of crystallite dimensions and dislocation densities – of X-ray powder diffraction data collected on ground calcium fluorite, where size reduction and increased defectiveness have been correlated to the device effectiveness, and (ii) directly against video recorded *in operando* conditions.

Among the investigated variables, it is worth mentioning the jar-to-plate velocity ratio which has been shown to strongly affect the balls motion regime, in turn demonstrated to correlate to the amount of energy available for grinding by comparing the statistical occupation of the jar volume and the available energy estimated from simulations. Particularly it has been demonstrated that, the more the motion is complex, the higher is the impact energy.

The model was further exploited to analyse the effect of the jar shape, a parameter usually neglected by the literature. Four innovative designs have been proposed, aimed at breaking the cylindrical symmetry of the standard cylindrical jar in different way but pursuing the same goal of disordering balls movements. Obstacles or polygonal profiles were introduced so to drive balls along trajectories promoting impacts with high axial velocity component, deemed as the most effective in the comminution process. Simulations output – analysed in terms of average available energy, balls trajectories and velocity probability distribution, both in normal and tangential direction – are rather promising, suggesting the newly designed jars to provide with an increased amount of available energy in the contact direction with respect to the standard cylindrical vial. Moreover, the range of jar-to-plate velocity ratio corresponding to the most disordered ball motion and, in turn, to the most efficient grinding conditions has been revealed to be more extended for the new jars. Being less sensitive to milling parameters, the new vials were therefore supposed to give more robust grinding. To conclude, newly designed jars were also experimentally shown to require shorter milling time than the cylindrical design to achieve the same results in terms of mill charge comminution, reducing therefore the overall process duration with consequent time and energy saving.

The flexibility and simplicity of the model developed in this Thesis allowed and will allow a detailed com-

prehension and tuning of milling parameters for specific cases, *e.g.* requiring mostly tangential – this is, for example, the case of the exfoliation from a bulk of two-dimensional materials – or normal mechanical actions, exploitable *e.g.* for the reduction of crystallite size of poorly soluble drugs, possibly contributing in the challenge of bioavailability enhancement.

Further directions of research will include the understanding of the role of variables such as size and volume fraction of milling media on the process efficiency. Moreover, a deeper comprehension of the fracture of the mill charge could be achieved by coupling the outcome of the presented model – in terms of velocity, direction and duration of collision – with theoretical models of dynamic fracture and atomistic simulations of the contact event, shedding light on the formation and amount of structural defects.

Acknowledgements

Thanks to my tutors, Prof. P. Scardi and Prof. N. M. Pugno for giving me the opportunity to do the PhD. *Thanks* also to Dr. M. D'Incau for sharing his knowledge, for the collaboration and helpful advices.

Thanks to Prof. C. Della Volpe and Prof. S. Siboni encouraging me to explore other fields of science, for enthusiasm and precious suggestions.
Thanks to Prof. M. Gei, not only for science but also for always keeping an eye on me, kindly following my progresses and disasters!

Thanks to Dr. D. Catelani (MSC.Software) for the patient and continuous support.

Thanks to old and new friends, Arianna, Francesca, Stefania, Tania, Loredana, Marco, Roberto, Elisa and Cristy (and to their husbands/boyfriends/girlfriends and children too!) enriching my life of unforgettable moments and adventures.

Thanks to all my family and especially to my grandparents: your memory and love are always with me.

Thanks to my parents, Bruno and Anita, and to my sister, Micaela, lovingly supporting me and my weird decisions in every possible way. Thanks also to Lilly, always keeping me happy and warm!

Thanks to Luca, believing in me much more than I do. At the end, I must admit you were right: I made it! Thanks for having been there for me since we first met and, above all, for our amazing, adventurous and sweet life together!

Projects

The support from the FP7 IRSES Marie Curie Grant TAMER No. 610547 allowing me to travel to Russia is gratefully acknowledged.

Fondazione Caritro (project No 2013-0247 "Mechanical activation to improve bioavailability and reduce adverse effects of drugs in the therapy of chronic diseases") partially supporting this work is also aknowledged.

Abbreviations

Glossary

CAE	Computer Aided Engineering
DEM	Discrete Element Method
CaF_2	Calcium fluoride
XRPD	X-Ray powder diffraction
LPA	Line profile analysis
XRPD-LPA	X-Ray powder diffraction line profile analysis
WPPM	Whole Powder Pattern Modeling
FWHM	Full Width at Half Maximum
SEM	Scanning Electron Microscopy
CDF	Cylindrical Distribution Function
E_I/τ	Impact Power (or specific impact energy)
SE	Stress Energy
CY	Cylindrical jar
HM	Half-Moon jar
1L	1-Lifter jar
3L	3-Lifters jar
T	Triangular jar
EFV	Efavirenz

Symbols

ω	jar angular velocity
Ω	main disk (plate) angular velocity
$\omega/\Omega + 1$	Ratio of jar to plate angular velocity
$\dot{u}$	Relative velocity of colliding bodies
u	Relative displacement of colliding bodies, or compenetration
k	Generalised contact stiffness
c	Contact damping
μ_s	Static friction coefficient
μ_d	Dynamic friction coefficient
σ_y	Yield stress
$\langle D \rangle$	Average crystallite dimensions
ρ	Dislocation density

Bibliography

[1] P. Baláz *et al.* "Hallmarks of mechanochemistry: from nanoparticles to technology". *Chemical Society Reviews* **42** (2013), pp. 7571–7637. DOI: 10.1039/C3CS35468G.

[2] A. Lynch and C. Rowland. *The History of Grinding*. Society for Mining, Metallurgy, and Exploration, 2005.

[3] T.P. Yadav, R.M. Yadav, and D.P. Singh. "Mechanical milling: a top down approach for the synthesis of nanomaterials and nanocomposites". *Nanoscience and Nanotechnology* **2** (2012), pp. 22–48.

[4] Ö. Genç. "Energy-Efficient Technologies in Cement Grinding". In: *High Performance Concrete Technology and Applications*. Ed. by S. Yilmaz and H.B. Ozmen. Rijeka: InTech, 2016. Chap. 06. DOI: 10.5772/64427.

[5] D. Chaira and S.K. Karak. "Fabrication of Nanostructured Materials by Mechanical Milling". In: *Handbook of Mechanical Nanostructuring*. Wiley-VCH Verlag GmbH & Co. KGaA, 2015, pp. 379–416. DOI: 10.1002/9783527674947.ch16.

[6] H. Fecht, E. Hellstern, Z. Fu, and W. Johnson. "Nanocrystalline metals prepared by high-energy ball milling". English. *Metallurgical Transactions A* **21** (1990), pp. 2333–2337. DOI: 10.1007/BF02646980.

[7] VV.AA. *High-Energy Ball Milling: Mechanochemical Processing of Nanopowders*. Ed. by M. Sopicka-Lizer. Woodhead Publishing, 2010.

[8] C. Suryanarayana. "Mechanical alloying and milling". *Progress in Materials Science* **46** (2001), pp. 1–184. DOI: http://dx.doi.org/10.1016/S0079-6425(99)00010-9.

[9] V. Šepelák, S. Bégin-Colin, and G. Le Caër. "Transformations in oxides induced by high-energy ball-milling". *Dalton Transactions* **41** (2012), pp. 11927–11948. DOI: 10.1039/C2DT30349C.

[10] S. Indris, D. Bork, and P. Heitjans. "Nanocrystalline Oxide Ceramics Prepared by High-Energy Ball Milling". English. *Journal of Materials Synthesis and Processing* **8** (2000), pp. 245–250. DOI: 10.1023/A:1011324429011.

[11] Z.H. Loh, A.K. Samanta, and P.W.S. Heng. "Overview of milling techniques for improving the solubility of poorly water-soluble drugs". *Asian Journal of Pharmaceutical Sciences* **10** (2015), pp. 255–274. DOI: http://dx.doi.org/10.1016/j.ajps.2014.12.006.

[12] C.F. Burmeister and A. Kwade. "Process engineering with planetary ball mills". *Chemical Society Reviews* **42** (2013), pp. 7660–7667. DOI: 10.1039/C3CS35455E.

[13] I. Colombo, G. Grassi, and M. Grassi. "Drug mechanochemical activation". *Journal of Pharmaceutical Sciences* **98** (2009), pp. 3961–3986. DOI: 10.1002/jps.21733.

[14] R. Sonoda, M. Horibe, T. Oshima, T. Iwasaki, and S. Watano. "Improvement of Dissolution Property of Poorly Water-Soluble Drug by Novel Dry Coating Method Using Planetary Ball Mill". *Chemical and Pharmaceutical Bulletin* **56** (2008), pp. 1243–1247. DOI: 10.1248/cpb.56.1243.

[15] M.V. Antisari, A. Montone, N. Jovic, E. Piscopiello, C. Alvani, and L. Pilloni. "Low energy pure shear milling: A method for the preparation of graphite nano-sheets". *Scripta Materialia* **55** (2006), pp. 1047–1050. DOI: http://dx.doi.org/10.1016/j.scriptamat.2006.08.002.

[16] K. Kouroupis-Agalou, A. Liscio, E. Treossi, L. Ortolani, V. Morandi, N.M. Pugno, and V. Palermo. "Fragmentation and exfoliation of 2-dimensional materials: a statistical approach". *Nanoscale* **6** (2014), pp. 5926–5933. DOI: 10.1039/C3NR06919B.

[17] S.L. James *et al.* "Mechanochemistry: opportunities for new and cleaner synthesis". *Chem. Soc. Rev.* **41** (2012), pp. 413–447. DOI: 10.1039/C1CS15171A.

[18] S. Rosenkranz, S. Breitung-Faes, and A. Kwade. "Experimental investigations and modelling of the ball motion in planetary ball mills". *Powder Technology* **212** (2011), pp. 224–230. DOI: http://dx.doi.org/10.1016/j.powtec.2011.05.021.

[19] A. Nath, C. Jiten, and K.C. Singh. "Influence of ball milling parameters on the particle size of barium titanate nanocrystalline powders". *Physica B: Condensed Matter* **405** (2010), pp. 430–434. DOI: http://dx.doi.org/10.1016/j.physb.2009.08.299.

[20] M. Enayati, Z. Sadeghian, M. Salehi, and A. Saidi. "The effect of milling parameters on the synthesis of Ni3Al intermetallic compound by mechanical alloying". *Materials Science and Engineering: A* **375 - 377** (2004), pp. 809–811.

[21] E. Gaffet. "Planetary ball-milling: an experimental parameter phase diagram". *Materials Science and Engineering: A* **132** (1991), pp. 181–193. DOI: http://dx.doi.org/10.1016/0921-5093(91)90374-V.

[22] J. Kano and F. Saito. "Correlation of powder characteristics of talc during Planetary Ball Milling with the impact energy of the balls simulated by the Particle Element Method". *Powder Technology* **98** (1998), pp. 166–170. DOI: http://dx.doi.org/10.1016/S0032-5910(98)00039-4.

[23] J.G.d. Jalon and E. Bayo. *Kinematic and Dynamic Simulation of Multibody Systems: The Real Time Challenge*. Secaucus, NJ, USA: Springer-Verlag New York, Inc., 1994.

[24] R. Ledesma, Z..-.-D. Ma, G. Hulbert, and A. Wineman. "A nonlinear viscoelastic bushing element in multibody dynamics". *Computational Mechanics* **17** (1996), pp. 287–296. DOI: 10.1007/BF00368551.

[25] G. Gilardi and I. Sharf. "Literature survey of contact dynamics modelling". *Mechanism and Machine Theory* **37** (2002), pp. 1213–1239. DOI: http://dx.doi.org/10.1016/S0094-114X(02)00045-9.

[26] W. Goldsmith. *Impact: the theory and physical behaviour of colliding solids*. Dover Publications, 2001.

[27] R. Brach. *Mechanical Impact Dynamics: Rigid Body Collisions*. Raymond M. Brach, 2007.

[28] E. Anders. "Water on the Moon?" *Science* **169** (1970), pp. 1309–1310. DOI: 10.1126/science.169.3952.1309.

[29] P. Barkan. "Mechanical Design and Systems Handbook". In: McGraw-Hill, New York, 1974. Chap. Impact design.

[30] K.L. Johnson. *Contact Mechanics*. Cambridge University Press, 1985. DOI: 10.1017/CBO9781139171731.

[31] W.J. Stronge. *Impact Mechanics*. Cambridge University Press, 2000.

[32] P.E. Nikravesh. *Computer-aided Analysis of Mechanical Systems*. Upper Saddle River, NJ, USA: Prentice-Hall, Inc., 1988.

[33] G.C. Barker. "Computer Simulations of Granular Materials". In: *Granular Matter: An Interdisciplinary Approach*. Ed. by A. Mehta. New York, NY: Springer New York, 1994, pp. 35–83. DOI: 10.1007/978-1-4612-4290-1_2.

[34] P. Flores and H. Lankarani. *Contact Force Models for Multibody Dynamics*. Springer International Publishing, 2016.

[35] C.-y. Wu, L.-y. Li, and C. Thornton. "Rebound behaviour of spheres for plastic impacts". *International Journal of Impact Engineering* **28** (2003), pp. 929–946. DOI: http://dx.doi.org/10.1016/S0734-743X(03)00014-9.

[36] I. Newton. *Philosophiae naturalis principia mathematica*. Londini: S. Pepsy, Reg. Soc, London, 1686, 1687.

[37] H. Hertz. "Über die Berührung fester elastischer Körper". *Journal für die reine und angewandte Mathematik (Crelle's Journal)* **92** (1882), pp. 156–171.

[38] D. Bernoulli. "De vibrationibus et sono laminarum elasticum Commentiationes Physico-Geometricae". *Commentarii Academiae Scientiarum Imperialis Petropolitanae* **13** (1751), p. 105.

[39] S. Poisson. *Traité de mécanique, 2*. 2nd. Bachelier, Paris, 1833.

[40] C. Navier. "Note sur les effects des secousses imprimées aux poids suspendus á des fils ou á des verges élastiques". *Soc. Philomatique de Paris, Bull. des Sciences* **10** (1823), p. 73.

[41] S. Timoshenko. "Zur Frage nach der Wirkung eines Stosses auf einen Balken". *Zeits. Math. Phys.* **62** (1913), p. 198.

[42] M. Machado, P. Moreira, P. Flores, and H.M. Lankarani. "Compliant contact force models in multibody dynamics: Evolution of the Hertz contact theory". *Mechanism and Machine Theory* **53** (2012), pp. 99–121. DOI: http://dx.doi.org/10.1016/j.mechmachtheory.2012.02.010.

[43] E.T. Whittaker. *A treatise on the analytical dynamics of particles and rigid bodies; with an introduction to the problem of three bodies*. Cambridge: University Press, 1917.

[44] H. Minamoto and S. Kawamura. "Moderately high speed impact of two identical spheres". *International Journal of Impact Engineering* **38** (2011), pp. 123–129. DOI: http://dx.doi.org/10.1016/j.ijimpeng.2010.09.005.

[45] S. Faik and H. Witteman. "Modeling of impact dynamics: A literature survey." *International ADAMS User Conference* **80** (2000).

[46] C. Lim and W. Stronge. "Oblique elastic–plastic impact between rough cylinders in plane strain". *International Journal of Engineering Science* **37** (1999), pp. 97–122. DOI: http://dx.doi.org/10.1016/S0020-7225(98)00026-3.

[47] O.A. Bauchau and C. Ju. "Modeling friction phenomena in flexible multibody dynamics". *Computer Methods in Applied Mechanics and Engineering* **195** (2006), pp. 6909–6924. DOI: http://dx.doi.org/10.1016/j.cma.2005.08.013.

[48] F. Marques, P. Flores, and H.M. Lankarani. "On the Frictional Contacts in Multibody System Dynamics". In: *Multibody Dynamics: Computational Methods and Applications*. Ed. by J.M. Font-Llagunes. Cham: Springer International Publishing, 2016, pp. 67–91. DOI: 10.1007/978-3-319-30614-8_4.

[49] A.K. Banerjee and T.R. Kane. "Modeling and simulation of rotor bearing friction". *Journal of Guidance, Control, and Dynamics* **17** (1994), pp. 1137–1139. DOI: 10.2514/3.21323.

[50] H. Hirani. *Fundamentals of Engineering Tribology with Applications*. Cambridge University Press, 2016.

[51] CSM Instruments – Pin-on-Disk Tribometer (TRB). *http://www.csm-instruments.com/en/Pin-on-Disk-Tribometer*.

[52] P. Flores, J.C.P. Claro, and H. Lankarani. "A comparative study on continuous contact force models for constrained multibody systems". In: *Thematic Conference Multibody Dynamics 2011 (ECCOMAS)*. 2011.

[53] S.H. Zhu, S. Zwiebel, and G. Bernhardt. "A theoretical formula for calculating damping in the impact of two bodies in a multibody system". *Proceedings of the Institution of Mechanical Engineers, Part C: Journal of Mechanical Engineering Science* **213** (1999), pp. 211–216. DOI: 10.1243/0954406991522581.

[54] C.S. Koshy, P. Flores, and H.M. Lankarani. "Study of the effect of contact force model on the dynamic response of mechanical systems with dry clearance joints: computational and experimental approaches". *Nonlinear Dynamics* **73** (2013), pp. 325–338. DOI: 10.1007/s11071-013-0787-x.

[55] P. Ravn. "A Continuous Analysis Method for Planar Multibody Systems with Joint Clearance". *Multibody System Dynamics* **2** (1998), pp. 1–24. DOI: 10.1023/A:1009759826529.

[56] P. Dietl, J. Wensing, and G.C. van Nijen. "Rolling bearing damping for dynamic analysis of multi-body systems—experimental and theoretical results". *Proceedings of the Institution of Mechanical Engineers, Part K: Journal of Multi-body Dynamics* **214** (2000), pp. 33–43. DOI: 10.1243/1464419001544124.

[57] D. Zhang and W. Whiten. "The calculation of contact forces between particles using spring and damping models". *Powder Technology* **88** (1996), pp. 59–64. DOI: http://dx.doi.org/10.1016/0032-5910(96)03104-X.

[58] J.D. Hartog. *Mechanical Vibrations*. Dover Publications, New York, 1934.

[59] W. Thomson. *Theory of Vibrations with Applications, 4th ed.* Prentice-Hall, 1993.

[60] G. Hu, Z. Hu, B. Jian, L. Liu, and H. Wan. "On the Determination of the Damping Coefficient of Nonlinear Spring-dashpot System to Model Hertz Contact for Simulation by Discrete Element Method". In: *Information Engineering (ICIE), 2010 WASE International Conference on*. Vol. 3. 2010, pp. 295–298. DOI: 10.1109/ICIE.2010.247.

[61] F.P. Di Maio and A. Di Renzo. "Analytical solution for the problem of frictional-elastic collisions of spherical particles using the linear model". *Chemical Engineering Science* **59** (2004), pp. 3461–3475. DOI: http://dx.doi.org/10.1016/j.ces.2004.05.014.

[62] H.M. Lankarani and P.E. Nikravesh. "Continuous contact force models for impact analysis in multibody systems". English. *Nonlinear Dynamics* **5** (1994), pp. 193–207. DOI: 10.1007/BF00045676.

[63] D.W. Marhefka and D.E. Orin. "A compliant contact model with nonlinear damping for simulation of robotic systems". *IEEE Transactions on Systems, Man, and Cybernetics - Part A: Systems and Humans* **29** (1999), pp. 566–572.

[64] J. Alves, N. Peixinho, M.T. da Silva, P. Flores, and H.M. Lankarani. "A comparative study of the viscoelastic constitutive models for frictionless contact interfaces in solids". *Mechanism and Machine Theory* **85** (2015), pp. 172–188. DOI: http://dx.doi.org/10.1016/j.mechmachtheory.2014.11.020.

[65] S. Dubowsky and T.N. Gardner. "Design and Analysis of Multilink Flexible Mechanisms With Multiple Clearance Connections". *Journal of Engineering for Industry* **99** (1977), pp. 88–96. DOI: 10.1115/1.3439171.

[66] S. Dubowsky, J.F. Deck, and H. Costello. "The Dynamic Modeling of Flexible Spatial Machine Systems With Clearance Connections". *Journal of Mechanisms, Transmissions, and Automation in Design* **109** (1987), pp. 87–94. DOI: 10.1115/1.3258790.

[67] A.D. Renzo and F.P.D. Maio. "Comparison of contact-force models for the simulation of collisions in DEM-based granular flow codes". *Chemical Engineering Science* **59** (2004), pp. 525–541. DOI: http://dx.doi.org/10.1016/j.ces.2003.09.037.

[68] R.J. Rogers and G.C. Andrews. "Dynamic Simulation of Planar Mechanical Systems With Lubricated Bearing Clearances Using Vector-Network Methods". *Journal of Engineering for Industry* **99** (1977), pp. 131–137. DOI: 10.1115/1.3439126.

[69] S. Hegazy, H. Rahnejat, and K. Hussain. "Multi-body dynamics in full-vehicle handling analysis". **213** (2000).

[70] P.A. Cundall and O.D.L. Strack. "A discrete numerical model for granular assemblies". *Geotechnique* **29** (1979), 47–65(18).

[71] P.A. Cundall. *BALL - A program to model granular media using the distinct element method*. Tech. rep. Technical Note, Advanced Technology Group, 1978.

[72] S. Dubowsky and F. Freudenstein. "Dynamic Analysis of Mechanical Systems With Clearances – Part 1: Formation of Dynamic Model". *Journal of Engineering for Industry* **93** (1971), pp. 305–309. DOI: 10.1115/1.3427895.

[73] K.H. Hunt and F.R.E. Crossley. "Coefficient of Restitution Interpreted as Damping in Vibroimpact". *Journal of Applied Mechanics* **42** (1975), pp. 440–445. DOI: 10.1115/1.3423596.

[74] S. Shivaswamy and H.M. Lankarani. "Impact Analysis of Plates Using Quasi-Static Approach". *Journal of Mechanical Design* **119** (1997), pp. 376–381. DOI: 10.1115/1.2826358.

[75] X. Zhang and L. Vu-Quoc. "Modeling the dependence of the coefficient of restitution on the impact velocity in elasto-plastic collisions". *International Journal of Impact Engineering* **27** (2002), pp. 317–341. DOI: http://dx.doi.org/10.1016/S0734-743X(01)00052-5.

[76] E. Bayo and A. Avello. "Singularity-free augmented Lagrangian algorithms for constrained multibody dynamics". *Nonlinear Dynamics* **5** (1994), pp. 209–231. DOI: 10.1007/BF00045677.

[77] K.C. Park and J.C. Chiou. "A discrete momentum-conserving explicit algorithm for rigid body dynamics analysis". *International Journal for Numerical Methods in Engineering* **36** (1993), pp. 1071–1083. DOI: 10.1002/nme.1620360702.

[78] J.A.C. Ambrosio and P.E. Nikravesh. "Elasto-plastic deformations in multibody dynamics". *Nonlinear Dynamics* **3** (1992), pp. 85–104. DOI: 10.1007/BF00118987.

[79] A. Lisjak and G. Grasselli. "A review of discrete modeling techniques for fracturing processes in discontinuous rock masses". *Journal of Rock Mechanics and Geotechnical Engineering* **6** (2014), pp. 301–314. DOI: http://dx.doi.org/10.1016/j.jrmge.2013.12.007.

[80] N. Weerasekara, M. Powell, P. Cleary, L. Tavares, M. Evertsson, R. Morrison, J. Quist, and R. Carvalho. "The contribution of DEM to the science of comminution". *Powder Technology* **248** (2013), pp. 3–24. DOI: http://dx.doi.org/10.1016/j.powtec.2013.05.032.

[81] MSC Adams. *http://www.mscsoftware.com/it/product/adams*.

[82] H. Mio, J. Kano, F. Saito, and K. Kaneko. "Effects of rotational direction and rotation-to-revolution speed ratio in planetary ball milling". *Materials Science and Engineering: A* **332** (2002), pp. 75–80. DOI: http://dx.doi.org/10.1016/S0921-5093(01)01718-X.

[83] Y. Feng, K. Han, and D. Owen. "Discrete element simulation of the dynamics of high energy planetary ball milling processes". *Materials Science and Engineering: A* **375** (2004), pp. 815–819. DOI: http://dx.doi.org/10.1016/j.msea.2003.10.162.

[84] B. Mishra and R.K. Rajamani. "The discrete element method for the simulation of ball mills". *Applied Mathematical Modelling* **16** (1992), pp. 598–604. DOI: http://dx.doi.org/10.1016/0307-904X(92)90035-2.

[86] B. Mishra and C. Murty. "On the determination of contact parameters for realistic {DEM} simulations of ball mills". *Powder Technology* **115** (2001), pp. 290–297. DOI: http://dx.doi.org/10.1016/S0032-5910(00)00347-8.

[87] R.A. Serway, J.W. Jewett, and V. Peroomian. *Physics for Scientists and Engineers with Modern Physics*. Brooks/Cole Cengage Learning, 2014.

[88] A. Kharaz, D. Gorham, and A. Salman. "An experimental study of the elastic rebound of spheres". *Powder Technology* **120** (2001), pp. 281–291. DOI: http://dx.doi.org/10.1016/S0032-5910(01)00283-2.

[89] R.L. Jackson, I. Green, and D.B. Marghitu. "Predicting the coefficient of restitution of impacting elastic-perfectly plastic spheres". *Nonlinear Dynamics* **60** (2010), pp. 217–229. DOI: 10.1007/s11071-009-9591-z.

[90] R. Sondergaard, K. Chaney, and C. Brennen. "Measurements of solid spheres bouncing off flat plates". *Journal of Applied Mechanics* **112** (1990), pp. 694–699.

[93] M. D'Incau, M. Leoni, and P. Scardi. "High-energy grinding of FeMo powders". *Journal of Materials Research* **22** (2007), pp. 1744–1753. DOI: 10.1557/JMR.2007.0224.

[94] A. Stolle, T. Szuppa, S.E.S. Leonhardt, and B. Ondruschka. "Ball milling in organic synthesis: solutions and challenges". *Chemical Society Reviews* **40** (2011), pp. 2317–2329. DOI: 10.1039/C0CS00195C.

[95] P.L. Brun, E. Gaffet, L. Froyen, and L. Delaey. "Structure and properties of Cu, Ni and Fe powders milled in a planetary ball mill". *Scripta Metallurgica et Materialia* **26** (1992), pp. 1743–1748. DOI: http://dx.doi.org/10.1016/0956-716X(92)90545-P.

[96] M. Abdellaoui and E. Gaffet. "The physics of mechanical alloying in a planetary ball mill: Mathematical treatment". *Acta Metallurgica et Materialia* **43** (1995), pp. 1087–1098. DOI: http://dx.doi.org/10.1016/0956-7151(95)92625-7.

[97] B.S. Murty and S. Ranganathan. "Novel materials synthesis by mechanical alloying/milling". *International Materials Reviews* **43** (1998), pp. 101–141. DOI: 10.1179/imr.1998.43.3.101.

[98] L. Kong, J. Ma, and H. Huang. "$MgAl_2O_4$ spinel phase derived from oxide mixture activated by a high-energy ball milling process". *Materials Letters* **56** (2002), pp. 238–243. DOI: http://dx.doi.org/10.1016/S0167-577X(02)00447-0.

[99] P. Pochet, E. Tominez, L. Chaffron, and G. Martin. "Order-disorder transformation in Fe-Al under ball milling". *Physical Review B* **52** (1995), pp. 4006–4016. DOI: 10.1103/PhysRevB.52.4006.

[100] L. Kong, W. Zhu, and O. Tan. "Preparation and characterization of $Pb(Zr_{0.52}Ti_{0.48})O_3$ ceramics from high-energy ball milling powders". *Materials Letters* **42** (2000), pp. 232–239. DOI: http://dx.doi.org/10.1016/S0167-577X(99)00190-1.

[101] C. Silva, M. Graça, M. Valente, and A. Sombra. "Crystallite size study of nanocrystalline hydroxyapatite and ceramic system with titanium oxide obtained by dry ball milling". English. *Journal of Materials Science* **42** (2007), pp. 3851–3855. DOI: 10.1007/s10853-006-0474-0.

[102] T. Yadav and O. Srivastava. "Synthesis of nanocrystalline cerium oxide by high energy ball milling". *Ceramics International* **38** (2012), pp. 5783–5789. DOI: http://dx.doi.org/10.1016/j.ceramint.2012.04.025.

[103] J. de Carvalho, S. de Medeiros, M. Morales, A. Dantas, and A. Carriço. "Synthesis of magnetite nanoparticles by high energy ball milling". *Applied Surface Science* **275** (2013), pp. 84–87. DOI: http://dx.doi.org/10.1016/j.apsusc.2013.01.118.

[104] M. Gateshki, V. Petkov, G. Williams, S.K. Pradhan, and Y. Ren. "Atomic-scale structure of nanocrystalline ZrO_2 prepared by high-energy ball milling". *Physical Review B* **71** (2005), pp. 224107–224115. DOI: 10.1103/PhysRevB.71.224107.

[105] M. Zakeri, M.R. Rahimipour, and B.J. Abbasi. "Synthesis of nanostructure tetragonal $ZrO_2$by high energy ball milling". *Materials Technology* **28** (2013), pp. 181–186. DOI: 10.1179/1753555712Y.0000000044.

[106] M. Zakeri, M. Razavi, M. Rahimipour, and B.J. Abbasi. "Effect of ball to powder ratio on the ZrO_2 phase transformations during milling". *Physica B: Condensed Matter* **444** (2014), pp. 49–53. DOI: http://dx.doi.org/10.1016/j.physb.2014.03.010.

[107] P. Heitjans and S. Indris. "Fast diffusion in nanocrystalline ceramics prepared by ball milling". English. *Journal of Materials Science* **39** (2004), pp. 5091–5096. DOI: 10.1023/B:JMSC.0000039189.17243.72.

[108] M. Hussain, Y. Oku, A. Nakahira, and K. Niihara. "Effects of wet ball-milling on particle dispersion and mechanical properties of particulate epoxy composites". *Materials Letters* **26** (1996), pp. 177–184. DOI: http://dx.doi.org/10.1016/0167-577X(95)00223-5.

[109] Fritsch Vario-Planetary Mill PULVERISETTE 4. *http://www.fritsch-milling.com/products/milling/planetary-mills/pulverisette-4-classic-line/description/*.

[110] F.K. Urakaev. "Mineral processing by the abrasive-reactive wear". *International Journal of Mineral Processing* **92** (2009), pp. 58–66. DOI: http://dx.doi.org/10.1016/j.minpro.2009.02.010.

[111] N. Burgio, A. Iasonna, M. Magini, S. Martelli, and F. Padella. "Mechanical alloying of the Fe-Zr system. Correlation between input energy and end products". English. *Il Nuovo Cimento* **13** (1991), pp. 459–476. DOI: 10.1007/BF02452130.

[112] M. Magini, A. Iasonna, and F. Padella. "Ball milling: An experimental support to the energy transfer evaluated by the collision model". *Scripta Materialia* **34** (1996), pp. 13–19. DOI: http://dx.doi.org/10.1016/1359-6462(95)00465-3.

[113] P. Chattopadhyay, I. Manna, S. Talapatra, and S. Pabi. "A mathematical analysis of milling mechanics in a planetary ball mill". *Materials Chemistry and Physics* **68** (2001), pp. 85–94. DOI: http://dx.doi.org/10.1016/S0254-0584(00)00289-3.

[114] J. Raasch. "Trajectories and impact velocities of grinding bodies in planetary ball mills". *Chemical Engineering & Technology* **15** (1992), pp. 245–253. DOI: 10.1002/ceat.270150406.

[115] P.L. Brun, L. Froyen, and L. Delaey. "The modelling of the mechanical alloying process in a planetary ball mill: comparison between theory and in-situ observations". *Materials Science and Engineering: A* **161** (1993), pp. 75–82. DOI: http://dx.doi.org/10.1016/0921-5093(93)90477-V.

[116] T. Inoue and K. Okaya. "Grinding mechanism of centrifugal mills - a simulation study based on the discrete element method". *International Journal of Mineral Processing* **44** (1996), pp. 425–435. DOI: http://dx.doi.org/10.1016/0301-7516(95)00049-6.

[117] H. Mio, J. Kano, F. Saito, and K. Kaneko. "Optimum revolution and rotational directions and their speeds in planetary ball milling". *International Journal of Mineral Processing* **74** (2004), S85–S92. DOI: http://dx.doi.org/10.1016/j.minpro.2004.07.002.

[118] A. Iasonna and M. Magini. "Power measurements during mechanical milling. An experimental way to investigate the energy transfer phenomena". *Acta Materialia* **44** (1996), pp. 1109–1117. DOI: http://dx.doi.org/10.1016/1359-6454(95)00226-X.

[119] M. Magini, C. Colella, A. Iasonna, and F. Padella. "Power measurements during mechanical milling - II. The case of "single path cumulative" solid state reaction". *Acta Materialia* **46** (1998), pp. 2841–2850. DOI: http://dx.doi.org/10.1016/S1359-6454(98)80001-3.

[120] M. Magini, N. Burgio, A. Iasonna, S. Martelli, F. Padella, and E. Paradiso. "Analysis of energy transfer in the mechanical alloying process in the collision regime". *Journal of Materials Synthesis and Processing(USA)* **1** (1993), pp. 135–144.

[121] A. Joisel. "Broyeurs a satellite, Nr. 493, 1952". *Revue des matèriaux de construction* **493** (1956), pp. 234–250.

[122] H. Rumpf. *Vorlesungen über Mechanische Verfahrenstechnik*. Karlsruhe Universität, 1963 - 1964.

[123] H. Fischer. "Die Arbeitsvorgänge in Kugelmühlen, insbesondere in Rohrmühlen". *Z. VDI* **48** (1904), pp. 437–441.

[124] E. Davis. "Fine crushing ball-mills". *Trans. AIMME* **61** (1919), pp. 250–296.

[125] P.A. Cundall. "A computer model for simulating progressive, large-scale movements in blocky rock systems". In: *Proc. Symp. Int. Rock Mech.* Vol. 2. Nancy, 1971.

[126] G.D.J. de Jong and A. Verruijt. "Etude photo-élastique d'un empilement de disques". *Cah. Grpe fr. Etud. Rhéol* **2** (1969), pp. 73–86.

[127] M. Wolff, V. Salikov, S. Antonyuk, S. Heinrich, and G. Schneider. "Three-dimensional discrete element modeling of micromechanical bending tests of ceramic–polymer composite materials". *Powder Technology* **248** (2013), pp. 77–83. DOI: http://dx.doi.org/10.1016/j.powtec.2013.07.009.

[128] M. Yang, S. Li, and Q. Yao. "Mechanistic studies of initial deposition of fine adhesive particles on a fiber using discrete-element methods". *Powder Technology* **248** (2013), pp. 44–53. DOI: http://dx.doi.org/10.1016/j.powtec.2012.12.016.

[129] C. Thornton. "Numerical simulations of deviatoric shear deformation of granular media". *Géotechnique* **50** (2000), pp. 43–53. DOI: 10.1680/geot.2000.50.1.43.

[130] B. Mishra. "A review of computer simulation of tumbling mills by the discrete element method: Part I—contact mechanics". *International Journal of Mineral Processing* **71** (2003), pp. 73–93. DOI: http://dx.doi.org/10.1016/S0301-7516(03)00032-2.

[131] B. Mishra. "A review of computer simulation of tumbling mills by the discrete element method: Part II - Practical applications". *International Journal of Mineral Processing* **71** (2003), pp. 95–112. DOI: http://dx.doi.org/10.1016/S0301-7516(03)00031-0.

[132] B. Mishra and C. Thornton. "An improved contact model for ball mill simulation by the discrete element method". *Advanced Powder Technology* **13** (2002), pp. 25–41. DOI: http://dx.doi.org/10.1163/15685520252900938.

[133] D. Geissbuhler and M.L. Sawley. "Particle motion and energy dissipation spectra in a planetary ball mill". In: *PARTICLES 2013, III International Conference on Particle-based Methods – Fundamentals and Applications*. 2013.

[134] J. Kano, N. Chujo, and F. Saito. "A method for simulating the three-dimensional motion of balls under the presence of a powder sample in a tumbling ball mill". *Advanced Powder Technology* **8** (1997), pp. 39–51. DOI: http://dx.doi.org/10.1016/S0921-8831(08)60478-1.

[135] A. Kwade. "Mill selection and process optimization using a physical grinding model". *International Journal of Mineral Processing* **74, Supplement** (2004), S93–S101. DOI: http://dx.doi.org/10.1016/j.minpro.2004.07.027.

[136] J. Kano, H. Mio, and F. Saito. "Correlation of Size Reduction Rate of Inorganic Materials with Impact Energy of Balls in Planetary Ball Milling". *Journal of Chemical Engineering of Japan* **32** (1999), pp. 445–448. DOI: 10.1252/jcej.32.445.

[137] LIGGGHTS. *https://www.cfdem.com/liggghts-open-source-discrete-element-method-particle-simulation-code*.

[138] M. D'incau. "High Energy Milling in Nanomaterials Technologies: process modelling and optimization". PhD thesis. University of Trento, 2008.

[139] C. Fandaruff *et al.* "Correlation between microstructure and bioequivalence in Anti-HIV Drug Efavirenz". *European Journal of Pharmaceutics and Biopharmaceutics* **91** (2015), pp. 52–58. DOI: http://dx.doi.org/10.1016/j.ejpb.2015.01.020.

[140] P. Scardi. "Microstructural Properties: Lattice DEfects and Domain Size Effects". In: *Powder Diffraction. Theory and practice*. Ed. by R. Dinnebier and S. Billinge. RSC Publishing, Cambridge, 2008. Chap. 13, pp. 378–416.

[141] P. Scardi and M. Leoni. "Diffraction line profiles from polydisperse crystalline systems". *Acta Crystallographica Section A* **57** (2001), pp. 604–613. DOI: 10.1107/S0108767301008881.

[142] P. Scardi and M. Leoni. "Whole powder pattern modelling". *Acta Crystallographica Section A* **58** (2002), pp. 190–200. DOI: 10.1107/S0108767301021298.

[143] S. Sheibani, A. Ataie, S. Heshmati-Manesh, and G. Khayati. "Structural evolution in nano-crystalline Cu synthesized by high energy ball milling". *Materials Letters* **61** (2007), pp. 3204–3207. DOI: http://dx.doi.org/10.1016/j.matlet.2006.11.027.

[144] N. Rubio, C. Fabbro, M.A. Herrero, A. de la Hoz, M. Meneghetti, J.L.G. Fierro, M. Prato, and E. Vázquez. "Ball-Milling Modification of Single-Walled Carbon Nanotubes: Purification, Cutting, and Functionalization". *Small* **7** (2011), pp. 665–674. DOI: 10.1002/smll.201001917.

[145] I.-Y. Jeon, H.-J. Choi, S.-M. Jung, J.-M. Seo, M.-J. Kim, L. Dai, and J.-B. Baek. "Large-Scale Production of Edge-Selectively Functionalized Graphene Nanoplatelets via Ball Milling and Their Use as Metal-Free Electrocatalysts for Oxygen Reduction Reaction". *Journal of the American Chemical Society* **135** (2013), pp. 1386–1393. DOI: 10.1021/ja3091643.

[146] E.L. Parrott. "Milling of pharmaceutical solids". *Journal of Pharmaceutical Sciences* **63** (1974), pp. 813–829. DOI: 10.1002/jps.2600630603.

[147] J.E. Patterson, M.B. James, A.H. Forster, R.W. Lancaster, J.M. Butler, and T. Rades. "Preparation of glass solutions of three poorly water soluble drugs by spray drying, melt extrusion and ball milling". *International Journal of Pharmaceutics* **336** (2007), pp. 22–34. DOI: http://dx.doi.org/10.1016/j.ijpharm.2006.11.030.

[148] P. Liu, X. Rong, J. Laru, B. van Veen, J. Kiesvaara, J. Hirvonen, T. Laaksonen, and L. Peltonen. "Nanosuspensions of poorly soluble drugs: Preparation and development by wet milling". *International Journal of Pharmaceutics* **411** (2011), pp. 215–222. DOI: http://dx.doi.org/10.1016/j.ijpharm.2011.03.050.

[149] H.-j. Lu, G.-Z. Liang, X.-y. Ma, B.-y. Zhang, and X.-b. Chen. "Epoxy/clay nanocomposites: further exfoliation of newly modified clay induced by shearing force of ball milling". *Polymer International* **53** (2004), pp. 1545–1553. DOI: 10.1002/pi.1596.

[150] A. Esawi and K. Morsi. "Dispersion of carbon nanotubes (CNTs) in aluminum powder". *Composites Part A: Applied Science and Manufacturing* **38** (2007), pp. 646–650. DOI: http://dx.doi.org/10.1016/j.compositesa.2006.04.006.

[151] Y. Chen, J.F. Gerald, J. Williams, and S. Bulcock. "Synthesis of boron nitride nanotubes at low temperatures using reactive ball milling". *Chemical Physics Letters* **299** (1999), pp. 260–264. DOI: http://dx.doi.org/10.1016/S0009-2614(98)01252-4.

[152] Y. Fan, L. Wang, J. Li, J. Li, S. Sun, F. Chen, L. Chen, and W. Jiang. "Preparation and electrical properties of graphene nanosheet/Al_2O_3 composites". *Carbon* **48** (2010), pp. 1743–1749. DOI: http://dx.doi.org/10.1016/j.carbon.2010.01.017.

[153] W. Zhao, F. Wu, H. Wu, and G. Chen. "Preparation of Colloidal Dispersions of Graphene Sheets in Organic Solvents by Using Ball Milling". *Journal of Nanomaterials* **2010** (2010), 6:1–6:4. DOI: 10.1155/2010/528235.

[154] L.H. Li, Y. Chen, G. Behan, H. Zhang, M. Petravic, and A.M. Glushenkov. "Large-scale mechanical peeling of boron nitride nanosheets by low-energy ball milling". *Journal of Materials Chemistry* **21** (2011), pp. 11862–11866. DOI: 10.1039/C1JM11192B.

[155] H.M. Hilber, T.J.R. Hughes, and R.L. Taylor. "Improved numerical dissipation for time integration algorithms in structural dynamics". *Earthquake Engineering & Structural Dynamics* **5** (1977), pp. 283–292. DOI: 10.1002/eqe.4290050306.

[156] D. Negrut, R. Rampalli, G. Ottarsson, and A. Sajdak. "On an Implementation of the Hilber-Hughes-Taylor Method in the Context of Index 3 Differential-Algebraic Equations of Multibody Dynamics (DETC2005-85096)". *Journal of Computational and Nonlinear Dynamics* **2** (2006), pp. 73–85. DOI: 10.1115/1.2389231.

[157] VV.AA. *Defect and Microstructure Analysis by Diffraction*. Ed. by R.L. Snyder, H.J. Bunge, and J. Fiala. Oxford University Press, 1999.

[158] VV.AA. *Diffraction Analysis of the Microstructure of Materials*. Ed. by E. Mittemeijer and P. Scardi. Springer, 2004.

[159] E. Hellstern, H.J. Fecht, Z. Fu, and W.L. Johnson. "Structural and thermodynamic properties of heavily mechanically deformed Ru and AlRu". *Journal of Applied Physics* **65** (1989), pp. 305–310. DOI: http://dx.doi.org/10.1063/1.342541.

[160] J. Huang, Y. Wu, and H. Ye. "Ball milling of ductile metals". *Materials Science and Engineering: A* **199** (1995), pp. 165–172. DOI: http://dx.doi.org/10.1016/0921-5093(94)09715-1.

[161] Á. Révész, T. Ungár, A. Borbély, and J. Lendvai. "Dislocations and grain size in ball-milled iron powder". *Nanostructured Materials* **7** (1996), pp. 779–788. DOI: http://dx.doi.org/10.1016/S0965-9773(96)00048-7.

[162] L. Börner and J. Eckert. "Nanostructure formation and steady-state grain size of ball-milled iron powders". *Materials Science and Engineering: A* **226** (1997), pp. 541–545. DOI: http://dx.doi.org/10.1016/S0921-5093(97)80063-9.

[163] S. Vives, E. Gaffet, and C. Meunier. "X-ray diffraction line profile analysis of iron ball milled powders". *Materials Science and Engineering: A* **366** (2004), pp. 229–238. DOI: http://dx.doi.org/10.1016/S0921-5093(03)00572-0.

[164] O. Boytsov, A. Ustinov, E. Gaffet, and F. Bernard. "Correlation between milling parameters and microstructure characteristics of nanocrystalline copper powder prepared via a high energy planetary ball mill". *Journal of Alloys and Compounds* **432** (2007), pp. 103–110. DOI: http://dx.doi.org/10.1016/j.jallcom.2006.05.101.

[165] G.D. Giudici, R. Biddau, M. D'incau, M. Leoni, and P. Scardi. "Dissolution of nanocrystalline fluorite powders: An investigation by {XRD} and solution chemistry". *Geochimica et Cosmochimica Acta* **69** (2005), pp. 4073–4083. DOI: http://dx.doi.org/10.1016/j.gca.2005.04.002.

[166] E.O. Hall. "The Deformation and Ageing of Mild Steel: III Discussion of Results". *Proceedings of the Physical Society. Section B* **64** (1951), pp. 747–753.

[167] N.J. Petch. "The cleavage strength of polycrystals". *Journal of the Iron and Steel Institute* **174** (1953), pp. 25–28.

[168] G.I. Taylor. "The Mechanism of Plastic Deformation of Crystals. Part I. Theoretical". *Proceedings of the Royal Society of London A: Mathematical, Physical and Engineering Sciences* **145** (1934), pp. 362–387. DOI: 10.1098/rspa.1934.0106.

[170] A. Sato, J. Kano, and F. Saito. "Analysis of abrasion mechanism of grinding media in a planetary mill with {DEM} simulation". *Advanced Powder Technology* **21** (2010), pp. 212–216. DOI: http://dx.doi.org/10.1016/j.apt.2010.01.005.

[171] F. Schneider, A. Stolle, B. Ondruschka, and H. Hopf. "The Suzuki - Miyaura Reaction under Mechanochemical Conditions". *Organic Process Research & Development* **13** (2009), pp. 44–48. DOI: 10.1021/op800148y.

[172] T. Szuppa, A. Stolle, B. Ondruschka, and W. Hopfe. "Solvent-free dehydrogenation of [gamma]-terpinene in a ball mill: investigation of reaction parameters". *Green Chem.* **12** (2010), pp. 1288–1294. DOI: 10.1039/C002819C.

[173] M. Matsuoka, J. Hirata, and S. Yoshizawa. "Kinetics of solid-state polymorphic transition of glycine in mechano-chemical processing". *Chemical Engineering Research and Design* **88** (2010), pp. 1169–1173. DOI: 10.1016/j.cherd.2010.01.011.

[174] S. Chauruka, A. Hassanpour, R. Brydson, K. Roberts, M. Ghadiri, and H. Stitt. "Effect of mill type on the size reduction and phase transformation of gamma alumina". *Chemical Engineering Science* **134** (2015), pp. 774–783. DOI: http://dx.doi.org/10.1016/j.ces.2015.06.004.

[175] A. Rogachev, D. Moskovskikh, A. Nepapushev, T. Sviridova, S. Vadchenko, S. Rogachev, and A. Mukasyan. "Experimental investigation of milling regimes in planetary ball mill and their influence on structure and reactivity of gasless powder exothermic mixtures". *Powder Technology* **274** (2015), pp. 44–52. DOI: http://dx.doi.org/10.1016/j.powtec.2015.01.009.

[176] M. Leoni, T. Confente, and P. Scardi. "PM2K: a flexible program implementing Whole Powder Pattern Modelling". *Zeitschrift fr Kristallographie Supplements* **23** (2006), pp. 249–254.

[177] Topas-Academic. *http://www.topas-academic.net*.

[178] S. Sadrai, J.A. Meech, D. Tromans, and F. Sassani. "Energy efficient comminution under high velocity impact fragmentation". *Minerals Engineering* **24** (2011), pp. 1053–1061. DOI: http://dx.doi.org/10.1016/j.mineng.2011.05.006.

[179] D.A. Fulmer, W.C. Shearouse, S.T. Medonza, and J. Mack. "Solvent-free Sonogashira coupling reaction viahigh speed ball milling". *Green Chem.* **11** (2009), pp. 1821–1825. DOI: 10.1039/B915669K.

[180] V.P. Balema, J.W. Wiench, M. Pruski, and V.K. Pecharsky. "Solvent-free mechanochemical synthesis of phosphonium salts". *Chem. Commun.* (2002), pp. 724–725. DOI: 10.1039/B111515D.

[181] C. Suryanarayana. "Nanocrystalline materials". *International Materials Reviews* **40** (1995), pp. 41–64. DOI: 10.1179/imr.1995.40.2.41.

[182] E. Ivanov and C. Suryanarayana. "Materials and Process Design through Mechanochemical Routes". *Journal of Materials Synthesis and Processing* **8** (2000), pp. 235–244. DOI: 10.1023/A:1011372312172.

[184] K.D.M. Harris. "Mechanochemical synthesis: How grinding evolves". *Nature Chemistry* **5** (2013), pp. 12–14.

[185] T. Frišvcić, I. Halasz, P.J. Beldon, A.M. Belenguer, F. Adams, S.A. Kimber, V. Honkimäki, and R.E. Dinnebier. "Real-time and in situ monitoring of mechanochemical milling reactions". *Nature Chemistry* **5** (2013), pp. 66–73. DOI: 10.1038/nchem.1505.

[186] J.P. Cline, R.D. Deslattes, J.L. Staudenmann, E.G. Kessler, L.T. Hudson, A. Henins, and R.W. Cheary. *Certificate SRM 660a*. NIST, Gaithersburg, MD, USA. 2000.

[187] M. Abdellatief, M. Abele, M. Leoni, and P. Scardi. "Combined X-ray diffraction and solid-state ^{1}9F magic angle spinning NMR analysis of lattice defects in nanocrystalline CaF_2". *Journal of Applied Crystallography* **46** (2013), pp. 1049–1057. DOI: 10.1107/S0021889813016944.

[188] M. Abdellatief, M. Abele, M. Leoni, and P. Scardi. "Solid State Nuclear Magnetic Resonance and X-ray Diffraction Line Profile Analysis of heavily deformed fluorite". *Thin Solid Films* **530** (2013), pp. 44–48. DOI: http://dx.doi.org/10.1016/j.tsf.2012.09.020.

[189] W. Zhao, M. Fang, F. Wu, H. Wu, L. Wang, and G. Chen. "Preparation of graphene by exfoliation of graphite using wet ball milling". *Journal of Materials Chemistry* **20** (2010), pp. 5817–5819. DOI: 10.1039/C0JM01354D.

[190] Y. Chen, C.P. Li, H. Chen, and Y. Chen. "One-dimensional nanomaterials synthesized using high-energy ball milling and annealing process". *Science and Technology of Advanced Materials* **7** (2006), pp. 839–846. DOI: http://dx.doi.org/10.1016/j.stam.2006.11.014.

[191] A.K. Geim and K.S. Novoselov. "The rise of graphene". *Nature Materials* **6** (2007), pp. 183–191.

[192] A.C. Ferrari *et al.* "Science and technology roadmap for graphene, related two-dimensional crystals, and hybrid systems". *Nanoscale* **7** (2015), pp. 4598–4810. DOI: 10.1039/C4NR01600A.

[193] K.S. Novoselov, A.K. Geim, S.V. Morozov, D. Jiang, M.I. Katsnelson, I.V. Grigorieva, S.V. Dubonos, and A.A. Firsov. "Two-dimensional gas of massless Dirac fermions in graphene". *Nature* **438** (2005), pp. 197–200.

[194] A.A. Balandin, S. Ghosh, W. Bao, I. Calizo, D. Teweldebrhan, F. Miao, and C.N. Lau. "Superior Thermal Conductivity of Single-Layer Graphene". *Nano Letters* **8** (2008), pp. 902–907. DOI: 10.1021/nl0731872.

[195] A. Vakil and N. Engheta. "Transformation Optics Using Graphene". *Science* **332** (2011), pp. 1291–1294. DOI: 10.1126/science.1202691.

[196] O.V. Yazyev, R.B. Capaz, and S.G. Louie. "Theory of magnetic edge states in chiral graphene nanoribbons". *Physical Review B* **84** (2011), p. 115406. DOI: 10.1103/PhysRevB.84.115406.

[197] C. Lee, X. Wei, J.W. Kysar, and J. Hone. "Measurement of the Elastic Properties and Intrinsic Strength of Monolayer Graphene". *Science* **321** (2008), pp. 385–388. DOI: 10.1126/science.1157996.

[198] K.S. Novoselov, A.K. Geim, S.V. Morozov, D. Jiang, Y. Zhang, S.V. Dubonos, I.V. Grigorieva, and A.A. Firsov. "Electric Field Effect in Atomically Thin Carbon Films". *Science* **306** (2004), pp. 666–669. DOI: 10.1126/science.1102896.

[199] X. Fan, D.W. Chang, X. Chen, J.-B. Baek, and L. Dai. "Functionalized graphene nanoplatelets from ball milling for energy applications". *Current Opinion in Chemical Engineering* **11** (2016), pp. 52–58. DOI: https://doi.org/10.1016/j.coche.2016.01.003.

[200] S. Guo and S. Dong. "Graphene nanosheet: synthesis, molecular engineering, thin film, hybrids, and energy and analytical applications". *Chemical Society Reviews* **40** (2011), pp. 2644–2672. DOI: 10.1039/C0CS00079E.

[201] V. Leon, M. Quintana, M.A. Herrero, J.L.G. Fierro, A.d.l. Hoz, M. Prato, and E. Vazquez. "Few-layer graphenes from ball-milling of graphite with melamine". *Chemical Communication* **47** (2011), pp. 10936–10938. DOI: 10.1039/C1CC14595A.

[202] L. Liu, Z. Xiong, D. Hu, G. Wu, and P. Chen. "Production of high quality single- or few-layered graphene by solid exfoliation of graphite in the presence of ammonia borane". *Chemical Communication* **49** (2013), pp. 7890–7892. DOI: 10.1039/C3CC43670E.

[203] H. Zhang and P.X. Feng. "Fabrication and characterization of few-layer graphene". *Carbon* **48** (2010), pp. 359–364. DOI: http://dx.doi.org/10.1016/j.carbon.2009.09.037.

[204] K.S. Kim *et al.* "Large-scale pattern growth of graphene films for stretchable transparent electrodes". *Nature* **457** (2009), pp. 706–710.

[205] M. Choucair, P. Thordarson, and J.A. Stride. "Gram-scale production of graphene based on solvothermal synthesis and sonication". *Nature Nanotechnology* **4** (2009), pp. 30–33.

[206] Y. Hernandez *et al.* "High-yield production of graphene by liquid-phase exfoliation of graphite". *Nature Nanotechnology* **3** (2008), pp. 563–568.

[207] W. Gu *et al.* "Graphene sheets from worm-like exfoliated graphite". *Journal of Materials Chemistry* **19** (2009), pp. 3367–3369. DOI: 10.1039/B904093P.

[208] A. Ciesielski and P. Samori. "Graphene via sonication assisted liquid-phase exfoliation". *Chem. Soc. Rev.* **43** (2014), pp. 381–398. DOI: 10.1039/C3CS60217F.

[209] H. Wu, W. Zhao, H. Hu, and G. Chen. "One-step in situball milling synthesis of polymer-functionalized graphene nanocomposites". *Journal of Mateials Chemistry* **21** (2011), pp. 8626–8632. DOI: 10.1039/C1JM10819K.

[210] H. Zhu, Y. Cao, J. Zhang, W. Zhang, Y. Xu, J. Guo, W. Yang, and J. Liu. "One-step preparation of graphene nanosheets via ball milling of graphite and the application in lithium-ion batteries". *Journal of Materials Science* **51** (2016), pp. 3675–3683. DOI: 10.1007/s10853-015-9655-z.

[211] Y. Chen, J.F. Gerald, L.T. Chadderton, and L. Chaffron. "Nanoporous carbon produced by ball milling". *Applied Physics Letters* **74** (1999), pp. 2782–2784. DOI: 10.1063/1.124012.

[212] F. Salver-Disma, J. Tarascon, C. Clinard, and J. Rouzaud. "Transmission electron microscopy studies on carbon materials prepared by mechanical milling". *Carbon* **37** (1999), pp. 1941–1959. DOI: http://dx.doi.org/10.1016/S0008-6223(99)00059-7.

[213] F. Salver-Disma, C. Lenain, B. Beaudoin, L. Aymard, and J. Tarascon. "Unique effect of mechanical milling on the lithium intercalation properties of different carbons". *Solid State Ionics* **98** (1997), pp. 145–158. DOI: http://dx.doi.org/10.1016/S0167-2738(97)00108-2.

[214] L.H. Li, Y. Chen, B.-M. Cheng, M.-Y. Lin, S.-L. Chou, and Y.-C. Peng. "Photoluminescence of boron nitride nanosheets exfoliated by ball milling". *Applied Physics Letters* **100** (2012), p. 261108. DOI: 10.1063/1.4731203.

[215] Deepika, L.H. Li, A.M. Glushenkov, S.K. Hait, P. Hodgson, and Y. Chen. "High-Efficient Production of Boron Nitride Nanosheets via an Optimized Ball Milling Process for Lubrication in Oil". **4** (2014), p. 7288.

[216] D. Berman, A. Erdemir, and A.V. Sumant. "Graphene: a new emerging lubricant". *Materials Today* **17** (2014), pp. 31–42. DOI: http://dx.doi.org/10.1016/j.mattod.2013.12.003.

[217] Engineer's Handbook. *http://www.engineershandbook.com/index.htm*.

[218] UNIDAS. *Global AIDS updae*. Tech. rep. 2016.

[219] G.L. Amidon, H. Lennernäs, V.P. Shah, and J.R. Crison. "A Theoretical Basis for a Biopharmaceutic Drug Classification: The Correlation of in Vitro Drug Product Dissolution and in Vivo Bioavailability". *Pharmaceutical Research* **12** (1995), pp. 413–420. DOI: 10.1023/A:1016212804288.

[220] J. Le. "The Merck manual of diagnosis and therapy online". In: ed. by M.H. Beers, R.S. Porter, T.V. Jones, J.L. Kaplan, and M. Berkwits. 2017. Chap. Drug Bioavailability.

[221] A.C.C. de Melo, I.F. de Amorim, M.d.L. Cirqueira, and F.T. Martins. "Toward Novel Solid-State Forms of the Anti-HIV Drug Efavirenz: From Low Screening Success to Cocrystals Engineering Strategies and Discovery of a New Polymorph". *Crystal Growth & Design* **13** (2013), pp. 1558–1569. DOI: 10.1021/cg3018002.

[222] P. Khadka *et al.* "Pharmaceutical particle technologies: An approach to improve drug solubility, dissolution and bioavailability". *Asian Journal of Pharmaceutical Sciences* **9** (2014), pp. 304–316. DOI: http://dx.doi.org/10.1016/j.ajps.2014.05.005.

[223] da Costa, M. Assis, R.C. Seiceira, C.R. Rodrigues, C.R.D. Hoffmeister, L.M. Cabral, and H.V.A. Rocha. "Efavirenz Dissolution Enhancement I: Co-Micronization". *Pharmaceutics* **5** (2012), pp. 1–22.

[224] K.T. Savjani, A.K. Gajjar, and J.K. Savjani. "Drug Solubility: Importance and Enhancement Techniques". *ISRN Pharmaceutics* **2012** (2012).

[225] S. Kalepu and V. Nekkanti. "Insoluble drug delivery strategies: review of recent advances and business prospects". *Acta Pharmaceutica Sinica. B* **5** (2015), pp. 442–453.

[226] V.B. Junyaprasert and B. Morakul. "Nanocrystals for enhancement of oral bioavailability of poorly water-soluble drugs". *Asian Journal of Pharmaceutical Sciences* **10** (2015), pp. 13–23. DOI: http://dx.doi.org/10.1016/j.ajps.2014.08.005.

[227] S.M. Dizaj, Z. Vazifehasl, S. Salatin, K. Adibkia, and Y. Javadzadeh. "Nanosizing of drugs: Effect on dissolution rate". *Research in Pharmaceutical Sciences* **10** (2014), pp. 95–108.

[228] A. Dokoumetzidis and P. Macheras. "A century of dissolution research: From Noyes and Whitney to the Biopharmaceutics Classification System". *International Journal of Pharmaceutics* **321** (2006), pp. 1–11. DOI: http://dx.doi.org/10.1016/j.ijpharm.2006.07.011.

[229] B. Sinha, R.H. Müller, and J.P. Möschwitzer. "Bottom-up approaches for preparing drug nanocrystals: formulations and factors affecting particle size". *International journal of pharmaceutics* **453** (2013), pp. 126–141. DOI: 10.1016/j.ijpharm.2013.01.019.

[230] T.-L. Chang, H. Zhan, D. Liang, and J.F. Liang. "Nanocrystal technology for drug formulation and delivery". *Frontiers of Chemical Science and Engineering* **9** (2015), pp. 1–14. DOI: 10.1007/s11705-015-1509-3.

[231] N. Rasenack and B.W. Müller. "Micron-Size Drug Particles: Common and Novel Micronization Techniques". *Pharmaceutical Development and Technology* **9** (2004), pp. 1–13. DOI: 10.1081/PDT-120027417.

[232] E. Cappelletto, L. Rebuffi, A. Flor, and P. Scardi. "Microstructural effects of high-energy grinding on poorly soluble drugs: the case study of efavirenz". *Powder Diffraction* (2017), pp. 1–6. DOI: 10.1017/S0885715617000161.

[233] E. Cappelletto, C. Firrito, M. Pizzato, L. Rebuffic, and P. Scardi. "Mechanical activation of Efavirenz: the effects on the dissolution and inhibitory behavior". *Submitted to Pharmaceutical Development and Technology* (2017).

[234] H. Klug and L.E. Alexander. *X-Ray Diffraction Procedures: For Polycrystalline and Amorphous Materials, 2nd Edition*. Wiley-Interscience, 1974.

[235] J.B. Dressman, G.L. Amidon, C. Reppas, and V.P. Shah. "Dissolution Testing as a Prognostic Tool for Oral Drug Absorption: Immediate Release Dosage Forms". *Pharmaceutical Research* **15** (1998), pp. 11–22. DOI: 10.1023/A:1011984216775.

[236] J.L. Cohen, B.B. Hubert, L.J. Leeson, C.T. Rhodes, J.R. Robinson, T.J. Roseman, and E. Shefter. "The Development of USP Dissolution and Drug Release Standards". *Pharmaceutical Research* **7** (1990), pp. 983–987. DOI: 10.1023/A:1015922629207.

[237] E. Jantratid, V.D. Maio, E. Ronda, V. Mattavelli, M. Vertzoni, and J.B. Dressman. "Application of biorelevant dissolution tests to the prediction of in vivo performance of diclofenac sodium from an oral modified-release pellet dosage form". *European Journal of Pharmaceutical Sciences* **37** (2009), pp. 434–441. DOI: http://dx.doi.org/10.1016/j.ejps.2009.03.015.

[238] United States Pharmacopeia (USP). *http://www.usp.org*.

Scientific Production

[85] M. Broseghini, L. Gelisio, M. D'Incau, C.L.A. Ricardo, N.M. Pugno, and P. Scardi. "Modellazione del processo di macinazione ad alta energia tramite mulino a biglie planetario". *Analisi e Calcolo* **72** (2016), pp. 38–45.

[91] M. Broseghini, L. Gelisio, M. D Incau, C.A. Ricardo, N. Pugno, and P. Scardi. "Modeling of the planetary ball-milling process: The case study of ceramic powders". *Journal of the European Ceramic Society* **36** (2016), pp. 2205 - - 2212. DOI: http://dx.doi.org/10.1016/j.jeurceramsoc.2015.09.032.

[92] M. Broseghini, M. D'Incau, L. Gelisio, N. Pugno, and P. Scardi. "Effect of jar shape on high-energy planetary ball milling efficiency: Simulations and experiments". *Materials & Design* **110** (2016), pp. 365–374. DOI: http://dx.doi.org/10.1016/j.matdes.2016.06.118.

[169] M. Broseghini, L. Gelisio, M. D Incau, C.A. Ricardo, N. Pugno, and P. Scardi. "Corrigendum to "Modeling of the planetary ball-milling process: The case study of ceramic powders" [J. Eur. Ceram. Soc. 36 (9) (2016) 2205-2212]". *Journal of the European Ceramic Society* **37** (2017), p. 1141. DOI: http://dx.doi.org/10.1016/j.jeurceramsoc.2016.09.026.

[183] M. Broseghini, M. D'Incau, L. Gelisio, N. Pugno, and P. Scardi. "Homogeneity of ball milled ceramic powders: Effect of jar shape and milling conditions". *Data in Brief* **10** (2017), pp. 186–191. DOI: http://dx.doi.org/10.1016/j.dib.2016.11.070.

The content of the first part of chapter 4 of this Thesis is going to be included in a scientific publication, to date submitted:

- M. Broseghini, M. D'Incau, L. Gelisio, N. Pugno & P. Scardi. "Numerical and experimental investigations on new jar designs for high efficiency planetary ball milling." *Submitted*

Furthermore, in the next future, a paper reporting part of the analysis about the milling of Efavirenz in chapter 5 will be drafted.

During the Ph.D., I was involved in two research activities, not related to the topic of this Thesis, resulting in the production of the following scientific works:

- M. Broseghini, P. Zanetti, A.D. Jefferson & M. Gei. "Progressive instability in circular masonry columns." *Engineering Structures*, In press.
  My main task in this work was the development of a no-tension semi-analytical model for the instability of the circular masonry column.

- M. Broseghini, C. Ceccolini, C. Della Volpe & S. Siboni. "The notched stick, an ancient vibrot example." *In preparation*
  My main task in this work was performing multibody-dynamics simulations of the notched stick and I also participated in experimental testing.

The comminution and tuning of several structural parameters of materials is often accomplished following a top-down route by high-energy grinding. The reduced size of the particles constituting the end product and the incorporation of defects cause modified materials properties and increased solid-state chemical reactivity. Among grinding devices, the planetary ball mill features high efficiency and versatility, being suitable for processing almost any kind of material, from metals and ceramics to organic compounds and pharmaceuticals. While its design and working principle are rather simple, since grinding occurs by impacts between milling media (balls and jar) and mill charge, the characteristics of the end product strongly depend on a moltitude of variables, determining balls trajectories and velocities and, in turn, the nature of impulsive forces exchanged during collisions.
Numerical models can enourmously contribute to shed light on the process by providing the time evolution of kinematic and dynamic properties of milling media as well as quantities involved in contact events, permitting to understand the role of each milling variable and to design the characteristics of the end product. This Thesis chiefly proposes the implementation of a multibody dynamics model of the planetary ball milling process, its direct and indirect validation – respectively against movie collected *in-operando* and properties of the end product revealed by the analysis of X-ray powder diffraction data –, the evaluation of the effect of selected milling variables and the investigation of innovative solutions defining specific collision features, obtained by the re-design of the jar shape.

Marica Broseghni - Born in Trento (TN) in 1986, holds a degree in Building Engineering and Architecture (2013) from the Department of Civil, Environmental and Mechanical Engineering of the University of Trento. In 2014 she started a PhD at the University of Trento, focusing on the numerical modelling of mechanical systems.